Department of Physics and Astronomy Heidelberg University

Bachelor Thesis in Physics submitted by

Sarah Marie Michel

born in Böblingen (Germany)

2025

Performance of the BabyMOSS – A Repeated Sensor Unit of the Monolithic Stitched Sensor (MOSS) – for the ALICE ITS3 Upgrade

This Bachelor Thesis has been carried out by Sarah Marie Michel at the Physikalisches Institut, University Heidelberg under the supervision of Prof. Dr. Silvia Masciocchi

Abstract

During the Long Shutdown 3 (2026-2029) of the LHC at CERN, the ALICE experiment will upgrade the three innermost vertexing layers of its Inner Tracking System (ITS2) with truly cylindrical, bendable wafer-scale silicon sensors. The first stitched sensor prototype, called the Monolithic Stitched Sensor (MOSS), consists of ten stitched Repeated Sensor Units (RSUs).

This study focuses on smaller test chips called BabyMOSS, each containing a single RSU. The electrical performance of the BabyMOSS is evaluated through threshold scans across various DAC parameter configurations. The results are complemented by a dedicated test beam campaign, which provides insights into noise characteristics and cluster size behavior under in-beam conditions.

The study presents results for the sub-matrices of BabyMOSS, some of which contain different front-end electronics. These results highlight the impact of front-end design on noise levels and cluster size trends. The findings confirm the expected small cluster sizes, characteristic of the drift-dominated sensor, both with and without reverse bias applied between the diode and substrate. Notably, in the absence of reverse bias, peculiar noise patterns are observed, which are currently investigated by a complementary, separate study.

This work contributes to the optimization of stitched sensor design and provides valuable insights into the effects of various front-end design choices, helping to enhance future iterations of the detector.

Zusammenfassung

Während des Long Shutdown 3 (2026-2029) des LHC am CERN, wird das ALICE-Experiment die drei innersten Schichten seines Inner Tracking Systems (ITS2) mit wirklich zylindrischen, biegbaren Siliziumsensoren im Wafermaßstab aufrüsten. Der erste Stitched-Prototyp des Sensors, genannt Monolithic Stitched Sensor (MOSS), besteht aus zehn miteinander verbundenen Repeated Sensor Units (RSUs).

Diese Studie konzentriert sich auf kleinere Testchips, die als BabyMOSS bezeichnet werden und jeweils eine einzelne RSU enthalten. Das elektrische Verhalten des BabyMOSS wird durch Schwellenscans über verschiedene DAC-Parameterkonfigurationen untersucht. Die Ergebnisse werden durch eine dedizierte Testbeam-Kampagne ergänzt, die Einblicke in Rauschcharakteristika und Clustergrößenverhalten unter Bedingungen im Teilchenstrahl liefert.

Die Studie präsentiert Ergebnisse für die Sub-Matrizen von BabyMOSS, von denen einige unterschiedliche Front-End-Elektronik enthalten. Diese Ergebnisse zeigen den Einfluss des

Front-End-Designs auf Rauschpegel und Clustergrößentrends. Die Ergebnisse bestätigen die erwarteten kleinen Clustergrößen, die charakteristisch für den driftdominierten Sensor sind, sowohl mit als auch ohne angelegte Sperrspannung zwischen der Diode und dem Substrat. Bemerkenswerterweise werden ohne angelegte Sperrspannung ungewöhnliche Rauschmuster beobachtet, die derzeit durch eine ergänzende, separate Studie untersucht werden.

Diese Arbeit trägt zur Optimierung des Designs der Sensoren bei und liefert wertvolle Einblicke in die Auswirkungen verschiedener Front-End-Designs, die zur Verbesserung zukünftiger Iterationen des Detektors beitragen.

Contents

1	Inte	eraction of Charged Particles with Matter	1
	1.1	Energy Loss by Ionization and Excitation	1
		1.1.1 Energy Loss of Heavy Charged Particles	1
		1.1.2 Energy Loss of Electrons and Positrons	4
	1.2	Multiple Coulomb Scattering	6
2	\mathbf{AL}	ICE at the LHC	8
	2.1	Detector Layout of ALICE	8
	2.2	The Inner Tracking System 3 (ITS3)	9
3	Mo	nolithic Active Pixel Sensors (MAPS)	12
	3.1	Properties of Silicon	12
	3.2	Intrinsic and Extrinsic Semiconductors	13
	3.3	The pn Junction	14
	3.4	Metal-Oxide-Semiconductor Field-Effect Transistors	16
	3.5	Working Principle of MAPS	17
4	$Th\epsilon$	e Monolithic Stitched Sensor (MOSS)	20
	4.1	Pixel Design	20
	4.2	Production and Chip Architecture of MOSS and BabyMOSS	21
	4.3	Analog In-Pixel Front-End	23
5	Lab	oratory Scans 2	25
	5.1	Threshold Scan	26
	5.2	Exploration of the Threshold Range of BabyMOSS	35
6	Tes	t Beam	1 0
	6.1	DESY II Test Beam Facility	40
	6.2	Test Beam Campaign	42
7	Tes	t Beam Data Analysis	15
	7.1	Pixel Masking and Analysis of Hit Count Distributions	46
		7.1.1 Exemplary Analysis without Reverse Bias	48
		7.1.2 Exemplary Analysis with Reverse Bias	54
	7.2	Cluster Size Distributions	58
	7.3	Exploration of the Average Cluster Size over the VCASB Range	61
	7.4	Average Cluster Sizes for Matched Thresholds	64
		7.4.1 Analysis for Matched Thresholds without Reverse Bias 6	65
			69

8 Conclusion and Outlook	72
Appendix	77
References	78
Acknowledgements	82
Declaration	83

1 Interaction of Charged Particles with Matter

For a particle to be detected, it has to interact with matter. The detection of charged particles employs several processes of interaction with matter. These processes include ionization, excitation, bremsstrahlung, Cherenkov radiation and transition radiation and usually several subsequent interactions occur when a charged particle traverses the detector material [1].

This chapter focuses on the most important interaction processes regarding the energy loss of heavy charged particles and electrons, as well as multiple Coulomb scattering. When speaking about heavy charged particles, charged particles with a mass higher than the electron mass are referred to, thus excluding electrons and positrons [2].

1.1 Energy Loss by Ionization and Excitation

1.1.1 Energy Loss of Heavy Charged Particles

The dominant interaction processes for heavy charged particles with matter are ionization and excitation. Both ionization and excitation are Coulomb interactions, where the heavy charged particle electromagnetically interacts with an electron from an atom of the traversed material. If the atom gets excited, a bound electron of the atom reaches higher energy levels. When the excited atom returns to its initial state, it emits a photon in a process called de-excitation. If the atom gets ionized, however, the electron is completely removed from the atom. In general, ionization is the more relevant process regarding energy loss [2].

The average energy loss per path length of heavy charged particles in matter can be described by the Bethe-Bloch formula. This formula characterizes how the particles are stopped in matter, which is why the average energy loss is also called the stopping power. Here, the average energy loss is normalized to the density of the material in order to enable the comparison of the stopping power across different materials [1, 2]:

$$-\frac{dE}{dx}\frac{1}{\rho} = 4\pi N_A r_e^2 m_e c^2 z^2 \frac{Z}{A} \frac{1}{\beta^2} \left[\ln \left(\frac{2m_e c^2 \beta^2 \gamma^2}{I} \right) - \beta^2 - \frac{\delta(\beta \gamma)}{2} \right]$$
(1)

$$-\frac{dE}{dx}\frac{1}{\rho} = \kappa z^2 \frac{Z}{A} \frac{1}{\beta^2} \left[\ln \left(\frac{E_{kin}^{max}}{I} \right) - \beta^2 - \frac{\delta(\beta\gamma)}{2} \right]$$
 (2)

Constants:

N_A	Avogadro number
r_e	electron radius
m_e	electron mass
$\kappa = 4\pi N_A r_e^2 m_e c^2$	constant

Properties of the heavy charged particle:

z	charge in units of elementary charge
eta	$\frac{v}{c}$
γ	$\frac{1}{1-\beta^2}$ = Lorenz factor
$E_{kin}^{max} = 2m_e c^2 \gamma^2 \beta^2$	maximum energy transferred in a single collision

Properties of the material:

ρ	density of the material
Z	atomic number
A	atomic mass
I	mean excitation energy
δ	density correction

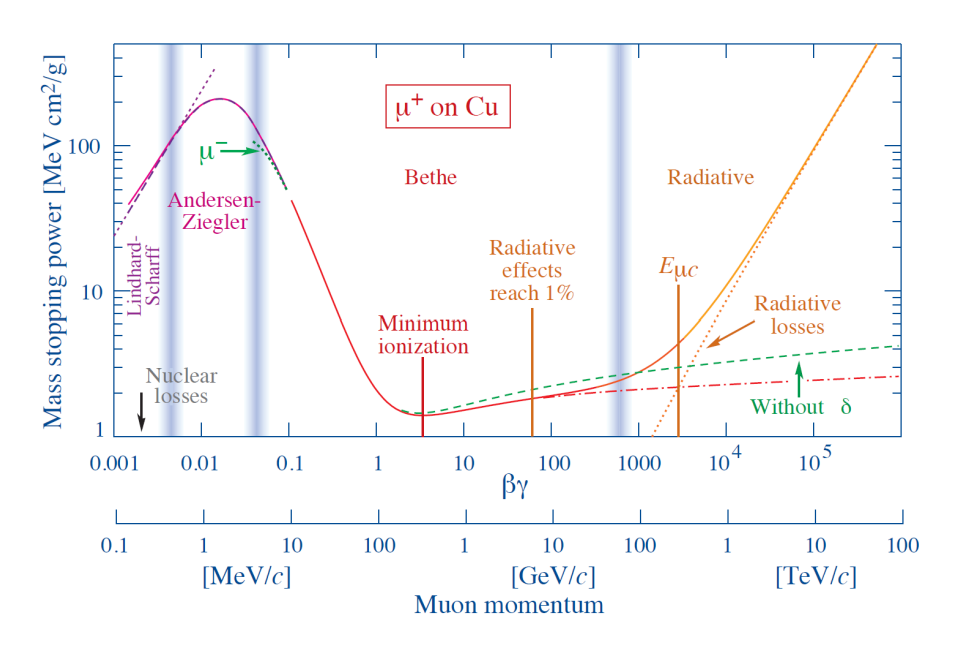


Figure 1: Stopping power for positive muons in copper [3].

The Bethe-Bloch formula is a function of $\beta\gamma=p/Mc$ and valid for the range of $0.5<\beta\gamma<500.$

An example of the stopping power, including the Bethe-Bloch range, is shown in Fig. 1.

In the low $\beta\gamma$ region of the Bethe-Bloch curve, the energy loss increases as the momentum of the incident particle decreases. This is due to the longer effective interaction time for slower particles. Since the momentum transfer is proportional to the interaction time, the momentum transfer increases and so does the energy loss. In this range, the energy loss is proportional to $\beta^{-5/3}$. If the momentum of the incident particle decreases further, its velocity can get close to the velocity of shell electrons and the assumption of electrons at rest loses its validity. At this point shell corrections must be taken into account.

For a momentum of $\beta \gamma \approx 3-4$, the energy loss is minimal and the incident particle is called Minimum Ionizing Particle (MIP). MIPs can be used as reference for detector calibration [2].

For higher $\beta\gamma$, the energy loss increases again. On the one hand, the maximum energy transfer in a single collision increases with γ . On the other hand, the increased energy loss correlates to a relativistic raise. The transverse electric field increases with γ , leading to an increased minimum possible energy transfer in the collision. However, the increase of the electric field is limited by the shielding of nearby atoms caused by the polarization of the medium. This process is referred to as density effect and is considered in the Bethe-Bloch formula with the term $\delta(\beta\gamma)$ [1].

In the high-momentum range, the stopping power grows proportional to $\ln(\beta\gamma)$ until it approaches a constant value, known as the Fermi plateau, because the maximum transferred energy stops to increase [2].

For even higher energies of the incident particle, radiative effects get more important than the energy loss by ionization [3].

The stopping power is dependent on the material and the incident particle. Regarding the material, the average energy loss is proportional to $\frac{Z}{A}$. For the incident particle, the Bethe-Bloch curve depends on $\beta \gamma = \frac{p}{Mc}$ with p as the momentum and M as the mass of the heavy charged particle [2].

Ultimately, the stopping power determines the range of the incident particle in the material. The amount of energy loss constantly changes with the decreasing momentum of the particle and follows the Bethe-Bloch curve in the backwards direction. This results in the Bragg peak, where the $\beta^{-5/3}$ dependency of the Bethe-Bloch curve for low momenta leads to a high energy transfer over a relatively short distance before the energy loss drops very low [1].

It is important to keep in mind that the stopping power depends on the average energy loss. The statistical fluctuations in energy loss are described by the Landau distribution, which displays the distribution of energy loss in individual collisions. This distribution is valid for materials with moderate thickness. In Fig. 2, straggling functions of the Landau

distribution are shown, which describe the actual energy loss Δ of a particle traversing a material with the thickness x. The width w is defined as the full-width half maximum. The asymmetric Landau distribution consists of a Gaussian distribution and a tail towards higher energy losses. Sometimes, ionization results in electrons with particularly high energy, the δ -electrons. In this instance, the highly-relativistic heavy charged particle transfers almost all its energy to a single electron. These δ -electrons cause the tail in the Landau distribution. Because of this tail, the most probable energy loss differs from the average energy loss [2].

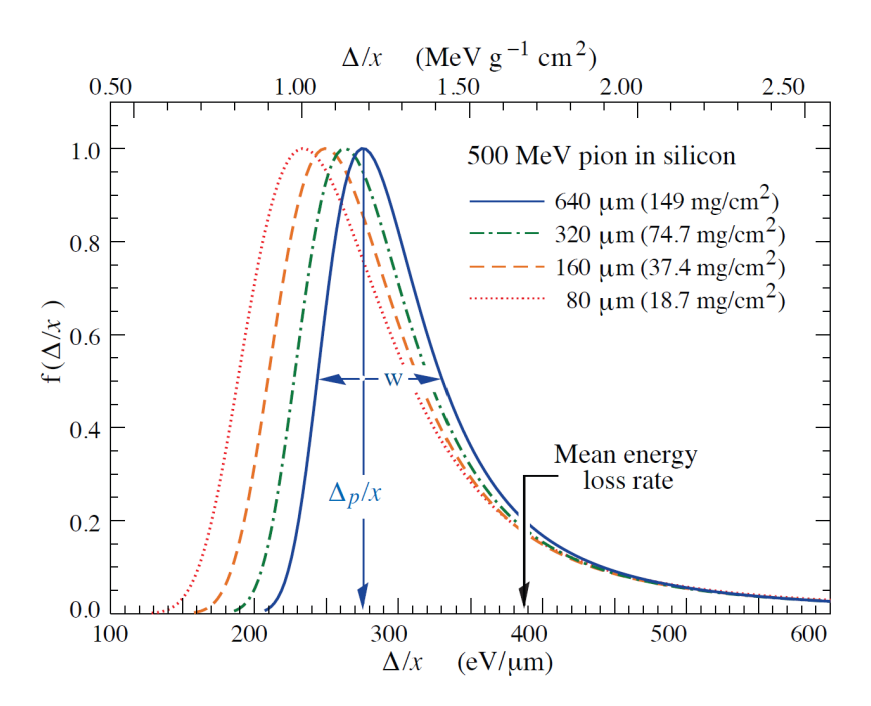


Figure 2: Straggling functions in silicon for 500 MeV pions, normalized to unity at the most probable value Δ_p/x [3].

1.1.2 Energy Loss of Electrons and Positrons

If the incident particle is an electron or positron and not a heavy charged particle, the Bethe-Bloch formula must be modified. In these cases, the incident particle has the same mass as the target particle and therefore the maximum transferred energy in a single collision does not equal the total kinetic energy T of the incident particle, but only half of it.

Additionally, if the incident particle is an electron, it becomes indistinguishable from the target particle after the collision, resulting in quantum mechanical effects. In this case, the stopping power relates to the faster of the two resulting electrons.

The modified Bethe-Bloch formula for electrons therefore includes a term for quantum mechanical corrections $F(\gamma)$:

$$-\frac{dE}{dx}\frac{1}{\rho} = \kappa \frac{Z}{A}\frac{1}{\beta^2} \left[\ln \left(\frac{m_e c^2 \beta^2 \gamma^2 T}{2I^2} \right) + F(\gamma) \right]$$
 (3)

If the incident particle is a positron, annihilation processes can occur at low energies, which increases the energy loss [2, 3].

Regarding light particles, bremsstrahlung becomes relevant already at relatively low energies and contributes to the energy loss in addition to ionization. Bremsstrahlung represents the deceleration of fast charged particles in the Coulomb field of an atomic nucleus. This is an electromagnetic interaction and a photon is emitted in the process. In Eq. 4, the formula for bremsstrahlung with an electron as incident particle is shown.

$$\left(-\frac{dE}{dx}\right)_{Brem} = 4\alpha N_A \frac{z^2 Z^2}{A} \left(\frac{1}{4\pi\epsilon_0} \cdot \frac{e^2}{mc^2}\right)^2 \cdot E \cdot \ln\left(\frac{183}{Z^{1/3}}\right) \tag{4}$$

Here, α is the fine structure constant and E is the energy of the incoming particle. For electrons as the incoming particle, this equation can be shortened to:

$$\left(-\frac{dE}{dx}\right)_{Brem} = \frac{E}{X_0} \tag{5}$$

 X_0 is the radiation length, which is a property of the material and describes the distance after which the energy of an electron is reduced to 37% of its initial energy E_0 in the specific material:

$$E' = \frac{E_0}{e} \approx 0.37 \cdot E_0 \tag{6}$$

Here, e is Euler's number [2].

In Fig. 3, the total energy loss for electrons, as a combination of ionization and bremsstrahlung, is displayed. The critical energy can be defined as the energy at which the energy loss by ionization and bremsstrahlung contribute to the total energy loss in equal parts. Another definition by Rossi describes the critical energy as the one where the energy loss by bremsstrahlung equals the energy loss by ionization per radiation length [3].

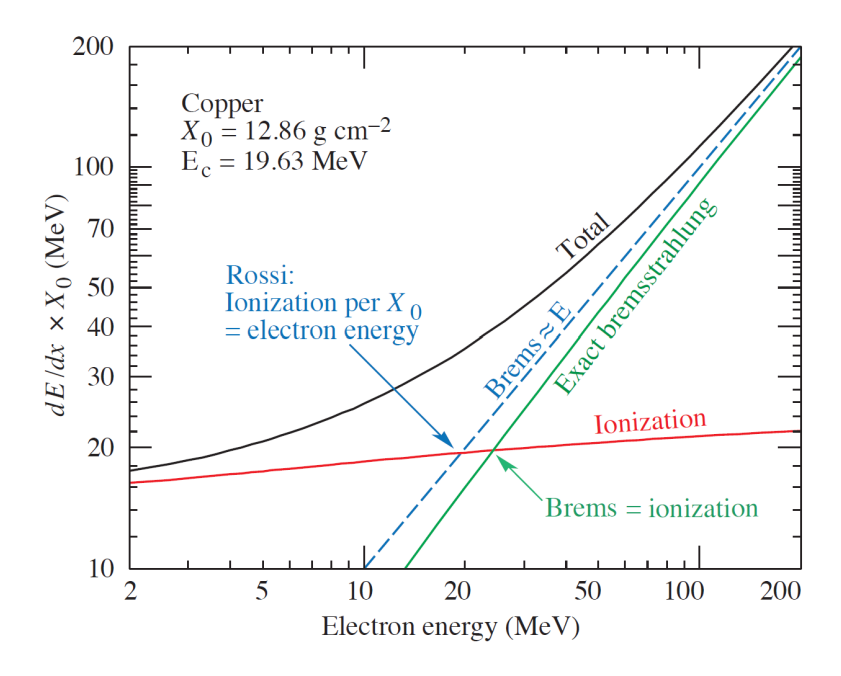


Figure 3: Energy loss of electrons in copper by ionization and bremsstrahlung [3].

1.2 Multiple Coulomb Scattering

When a charged particle traverses matter, it undergoes a large number of scattering processes where it is scattered by small angles, which leads to an overall deflection. This is called multiple scattering and is caused by the Coulomb fields of the nuclei of the material. The energy loss through multiple scattering is negligible, but it limits the momentum and tracking resolution of detectors [2].

For single collisions, the Coulomb scattering can be described by the Rutherford cross section:

$$\frac{d\sigma}{d\Omega} = z^2 Z^2 \alpha^2 \hbar^2 \frac{1}{\beta^2 p^2} \frac{1}{4sin^4(\theta/2)} \tag{7}$$

In this equation, θ is the scattering angle and Z is the atomic number of the matter. Properties of the incident particle are z as the charge, β as the velocity and p as the momentum. α is the fine structure constant and \hbar is the reduced Planck constant [2].

For a sufficiently thick material, where the number of scattering processes is at least 20, the multiple Coulomb scattering can be described by the Molière theory. According to the Molière theory, the distribution for small scattering angles can be approximated by a Gaussian distribution. This distribution is specified by the standard deviation θ_0 of the angle θ_{plane} . The spatial scattering angle θ_{plane} is the angle between the incident trajectory of the particle and the trajectory after the particle traversed the scattering volume, as displayed in Fig. 4 [1].

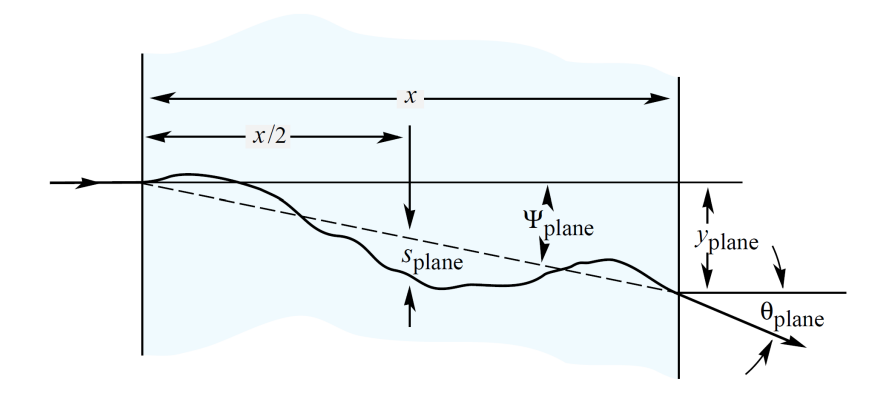


Figure 4: Multiple scattering of an incident particle traversing matter [3].

The parameter θ_0 can be approximated by the Highland formula:

$$\theta_0 = \sqrt{\langle \theta_{plane}^2 \rangle} = \frac{13.6 MeV/c}{p\beta} z \sqrt{\frac{x}{X_0}} \left[1 + 0.038 \cdot ln \left(\frac{x}{X_0} \right) \right]$$
 (8)

Here, x represents the thickness and X_0 the radiation length of the scattering material. The Highland formula indicates an increase of larger scattering angles for lower velocity and lower mass of the incident particle. Accordingly, electrons can be scattered at much larger angles than heavy particles [2].

2 ALICE at the LHC

ALICE (A Large Ion Collider Experiment) is a heavy-ion detector at the CERN Large Hadron Collider (LHC) [4].

Today, the LHC is the largest particle accelerator in the world with a 27 km long acceleration ring. Inside the ring, two particle beams are guided by a strong magnetic field created by superconducting electromagnets. The two beams can be collided at four interaction points, one of them being inside the ALICE detector [5].

The ALICE detector itself is 26 m long, 16 m high and 16 m wide and weighs 10000 tons. The purpose of ALICE is to explore the strongly interacting matter at extreme conditions, meaning high temperatures and energy densities. At these extreme conditions, a phase of matter called quark-gluon plasma (QGP) is formed, the characterization of which is the focus of the ALICE project. The high temperatures and energy densities are achieved by colliding heavy nuclei at the highest possible energies that can be provided by the LHC [4].

2.1 Detector Layout of ALICE

In order to be able to determine the properties of the QGP, the ALICE detector needs to capture the number, type, mass, energy and direction of the particles coming out of the QGP. For this purpose, several subdetectors are needed [4].

In Fig. 5 the ALICE 2 detector is shown, which is currently in operation.

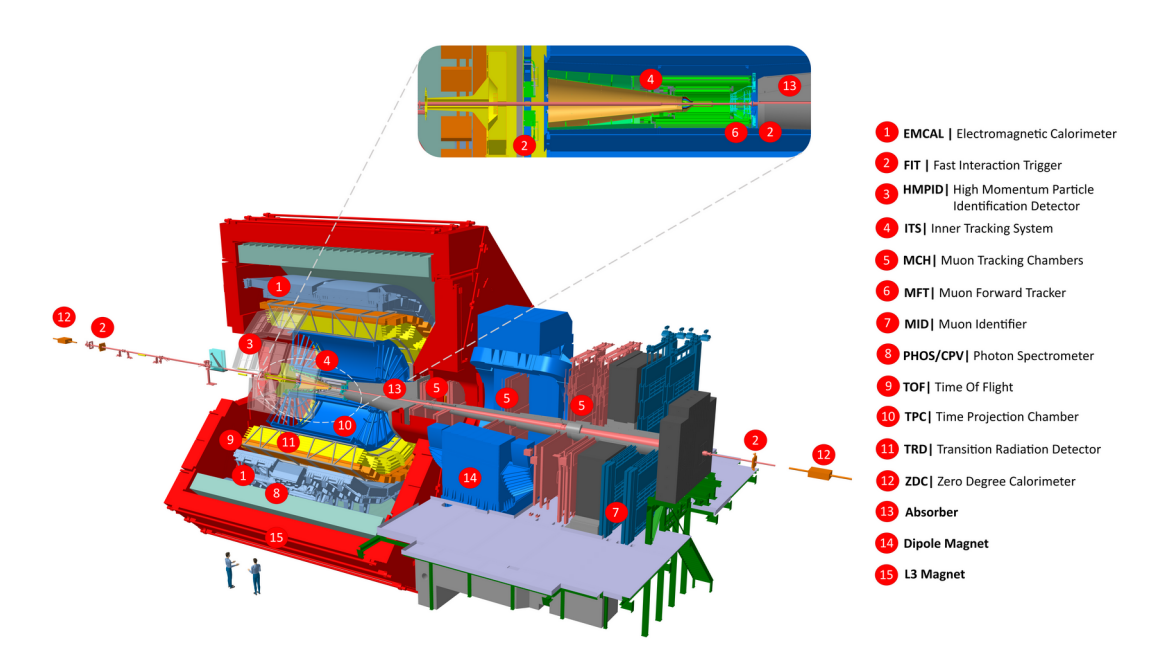


Figure 5: ALICE 2 detector systems [6].

The ALICE 2 detector includes a central barrel, a forward muon spectrometer and additional specialization detectors. The central barrel is responsible for detecting hadrons, electrons and photons and covers a polar angle from 45° to 135°. It is encased by a solenoid magnet, which provides a magnetic field of 0.5 T, forcing charged particles on a curved trajectory [4].

At this point, the two innermost detectors of the central barrel are discussed, since these detector layers are of main interest regarding the tracking of charged particles with low transverse momentum, which this study is focused on.

The vertex detector consists of the Inner Tracking System (ITS), which is responsible for reconstructing primary and secondary vertices, tracking and identifying charged particles with low transverse momentum p_T as well as improving the momentum resolution of charged particles at high p_T [4].

During the LHC Long Shutdown 2 (LS2, 2019-2021), the ITS was upgraded to the ITS2, leading to improved vertexing and tracking performance [7].

The ITS2 consists of seven approximately cylindrical silicon detector layers, where the three innermost layers build the Inner Barrel Module. Monolithic Active Pixel Sensors (MAPS), discussed in chapter 3, are used for the ITS2, which are referred to as ALPIDES (ALice PIxel DEtecor). In total, there are 24 thousand Monolithic Active Pixel Sensors installed, which cover a total active surface of $10 \, \mathrm{m}^2$ [8].

The next layer in the detector is formed by the Time Projection Chamber (TPC), which is the primary detector for the tracking of charged particles and particle identification in the central barrel of ALICE. The TPC is filled with gas, which is ionized by traversing charged particles. The electrons produced by ionization get amplified by Gas Electron Multipliers (GEMs) and drift towards the end plates, where the position and the time of arrival are read out. With this information the trajectory of the charged particle can be reconstructed. By measuring the specific energy loss dE/dx of the charged particle, the particle can be identified [4].

2.2 The Inner Tracking System 3 (ITS3)

Since 2022, the LHC Run 3 is running with the ITS2 implemented in ALICE. As the sensor technology of the ITS2, ALPIDE has demonstrated exceptional performance in terms of signal-to-noise ratio, spatial resolution, material budget, and readout speed [7]. However, the rapidly advancing CMOS imaging technology facilitates further development of the MAPS. Instead of the 180 nm CMOS technology used for ALPIDE, 65 nm technology can be used for the new sensors, enabling a more dense circuitry and a production on

larger wafers with a diameter of 300 mm [8].

Additionally, new CMOS imaging sensor technology allows for the application of stitching, which is described in chapter 4, and therefore the creation of larger sensors. These new features make the creation of a large curved sensor possible. The first stitched prototype sensor is referred to as Monolithic Stitched Sensor (MOSS) and further explored in chapter 4 [7].

During the Long Shutdown 3 (LS3, 2026-2029) the Inner Barrel Module of the ITS2 will be replaced with truly cylindrical layers of bendable wafer-scale silicon sensors, creating the ITS3 [8, 9].

The four remaining layers of the ITS2, which are further away from the interaction point, will not be replaced. The ITS3 detector layout is shown in Fig. 6. The three concentric cylindrical layers are split into two halves, which consist of one large sensor each, resulting in six sensors total [8].

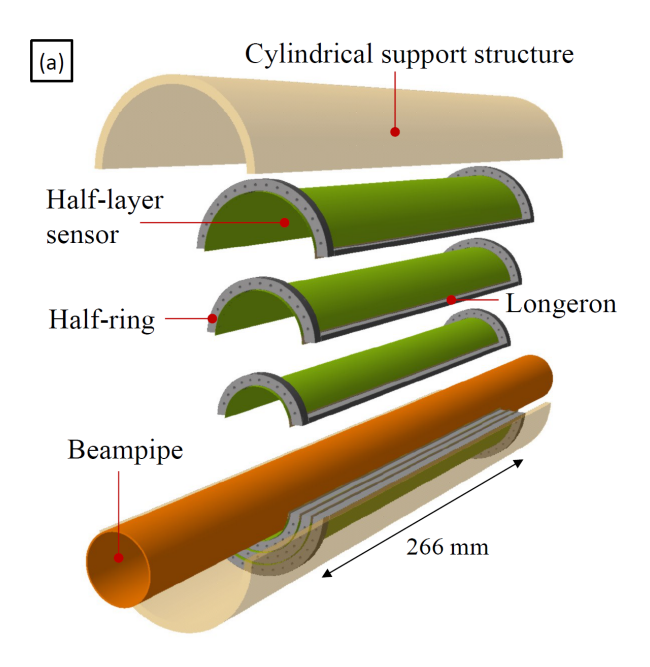


Figure 6: ITS3 detector layout [8].

The result of the upgraded sensors is a nearly massless detector consisting of wafer-scale silicon sensors with a size of up to $10 \,\mathrm{cm} \times 26 \,\mathrm{cm}$. With the new sensors, the material budget can be reduced from $0.35 \,\%\, \mathrm{X}_0$ to $0.07 \,\%\, \mathrm{X}_0$ per layer [7, 8].

The thickness of the sensors stays at about 50 µm and the truly cylindrical detector layers are supported by carbon foam, eliminating the need for staves as mechanical support. Moreover, water cooling can be eliminated and replaced with cooling by forced air flow. The innermost detector layer of the ITS3 can be positioned closer to the interaction point than the one of the ITS2, at a distance of 19 mm from the collision point and only 2 mm

from the beam pipe.

Resulting from the reduced material budget and the closeness to the interaction point, the detector will provide a spatial resolution improved by a factor of two compared to the ITS2 and a higher efficiency regarding the track reconstruction of low-momentum particles. The improved precision for reconstructing the decay topologies of heavy-flavor hadrons and dileptons will allow for a better understanding of the quark-gluon plasma formed in heavy-ion collisions.

Because the layers of ITS3 are closer to the interaction point than those of the ITS2, the flux of particles crossing the innermost layer will increase by 70%. Despite this increased particle flux, the hit occupancy stays relatively low due to the high granularity of the sensors, thus not overstraining the tracking capabilities. Correlating to the increased particle flux, the radiation load also increases by about 70%, but still remains well below the levels for which the 65 nm technology has been verified to maintain its performance [8].

3 Monolithic Active Pixel Sensors (MAPS)

Monolithic Active Pixel Sensors are made of silicon and utilize ionization to detect particles. When an ionizing particle traverses the semiconductive material, electron-hole pairs are created instead of electron-ion pairs, which are formed in gaseous detectors. In order to create one electron-hole pair in silicon, 3.6 eV are needed. In gaseous detectors, 30 eV are required to form one electron-ion pair. Therefore, the number of charges generated, i.e. the ionization yield, is about ten times higher in silicon, resulting in a better energy resolution and higher sensitivity [10].

In this chapter, the relevant properties of silicon and how it is used to create a Monolithic Active Pixel Sensor are explored.

3.1 Properties of Silicon

In order to understand the properties of a semiconductor like silicon, the energy band structure of crystalline solids is of great importance. In the periodic potential of a crystal lattice, there are quasi-continuous energy ranges that electrons are allowed to occupy. These energy ranges are called energy bands, which are separated by forbidden zones, also known as band gaps. The size of the band gap depends on the lattice constant and the binding forces of the crystal lattice. When an energy band is fully occupied by electrons, the electrons in that band do not contribute to the electrical conductivity of the crystalline solid. Hence, only the highest energy bands are of importance for the electrical conductivity of a crystal, while the lower energy bands, which are occupied according to Pauli's Principle, can be neglected. The two highest-lying energy bands consist of the valence band and the conduction band above, with the band gap E_G between them [11].

In Fig. 7, the band structures of insulators, semiconductors and conductors are schematically demonstrated.

In insulators, the valence band is entirely occupied, leaving the conduction band empty. The strong interatomic bonds of the valence band electrons in insulators cause the energy gap to be very large, which hinders electrons from being thermally excited into the conduction band. No current can flow.

In conductors, i.e. metals, the conduction band is partially occupied or both energy bands overlap, leading to electrical conductivity.

In semiconductors, the interatomic bonds are weaker than in insulators and therefore the energy gap is smaller. In the case of silicon, the energy gap consists of typically $1.12\,\mathrm{eV}$ [1]. At a temperature of $T=0\,\mathrm{K}$, the valence band is fully occupied, leading to isolating properties of the semiconductor. However, electrons from the valence band can be thermally excited into the conduction band for non-zero temperatures $T>0\,\mathrm{K}$.

The absence of an electron in the conduction band is called a hole, which appears as a positive charge because of the missing negative charge of the electron. The electrons in the conduction band and the holes in the valence band are free charge carriers, which enable the electrical conductivity of the semiconductor [1, 11].

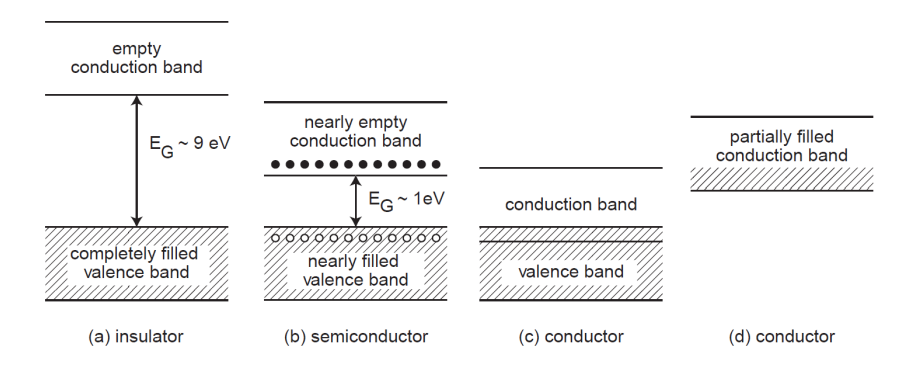


Figure 7: Occupation of valence and conduction band for insulators, semiconductors and conductors [1].

3.2 Intrinsic and Extrinsic Semiconductors

For intrinsic semiconductors, the concentration of electrons n equals the concentration of holes p. This concentration is also known as the intrinsic charge carrier concentration n_i :

$$n_i = n = p \tag{9}$$

The mobility of electrons μ_n in semiconductors is generally higher than the mobility of holes μ_p .

With these parameters, the electrical conductivity σ of an intrinsic semiconductor can be calculated as follows [11]:

$$\sigma = e(n\mu_n + p\mu_n) \tag{10}$$

$$\sigma_i = n_i \cdot e(\mu_n + \mu_p) \tag{11}$$

In intrinsic silicon, a carrier concentration of $n_i \approx 1.01 \cdot 10^{10} \, \mathrm{cm}^{-3}$ can be found [1]. The mobility of electrons in silicon amounts to $1450 \, \mathrm{cm}^2/\mathrm{Vs}$ and the mobility of holes to $500 \, \mathrm{cm}^2/\mathrm{Vs}$ [1]. Using these values, the electrical conductivity of silicon results in $\sigma_i \approx 2.8 \cdot 10^{-4} \, (\Omega \, \mathrm{m})^{-1}$ [1].

In order to change the electrical properties of semiconductors, the material can be doped, creating extrinsic semiconductors. In the process of doping, impurity atoms are incorporated into the semiconductor.

When pentavalent elements, such as arsenic, are introduced into a tetravalent semiconductor like silicon, the pentavalent atoms act as donors, leading to an excess of electrons

(Fig. 8). The energy levels of these donors appear close below the conduction band, causing donor electrons to be more easily excited into the conduction band. The resulting semiconductor with n >> p is called n-type semiconductor.

When trivalent elements, like boron, are introduced into a tetravalent semiconductor, the impurity atoms act as acceptors, leading to an excess of holes (Fig. 8). The energy levels of acceptors appear just above the valence band, which causes electrons from the valence band to be more easily excited into the acceptor levels, leaving holes in the valence band. This doped semiconductor with p >> n is called p-type semiconductor [1, 11].

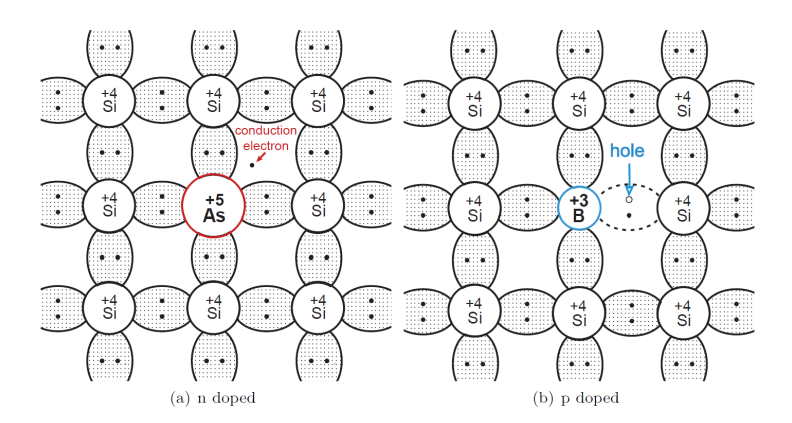


Figure 8: Schematic illustration of n- and p-type semiconductors [1].

In doped semiconductors, the unequal electron and hole densities cause one type of charge carriers to be more abundant than the other. These charge carriers are then called majority carriers, while the other, fewer carriers are called the minority carriers. Accordingly, in the p-doped semiconductor material, the majority carriers are holes, leaving electrons as minority carriers. In the n-doped material, the majority carriers are electrons and the minority carriers are holes [1].

3.3 The pn Junction

When combining p- and n-type semiconductor materials, pn junctions form.

The steep concentration gradient of charge carriers at the boundary between p- and n-doped materials leads to the diffusion of electrons from the n-type to the p-type side and holes from the p-type to the n-type side. As a result, electrons and holes recombine near the boundary of the pn junction, creating a depletion zone where there are no free charge carriers. The atoms become ionized after the recombination of electrons and holes in the depletion region. This leads to a negative space charge in the p-doped side and a positive space charge in the n-doped side of the depletion region. Consequently, an intrinsic electric field forms, that causes a drift of charge carriers opposite to the direction of diffusion.

This creates a stationary equilibrium between the drift current and diffusion current [1]. The drift and diffusion currents are illustrated in Fig. 9, as well as an exemplary doping concentration for a pn junction with the corresponding charge carrier density, space-charge density, electric field and potential.

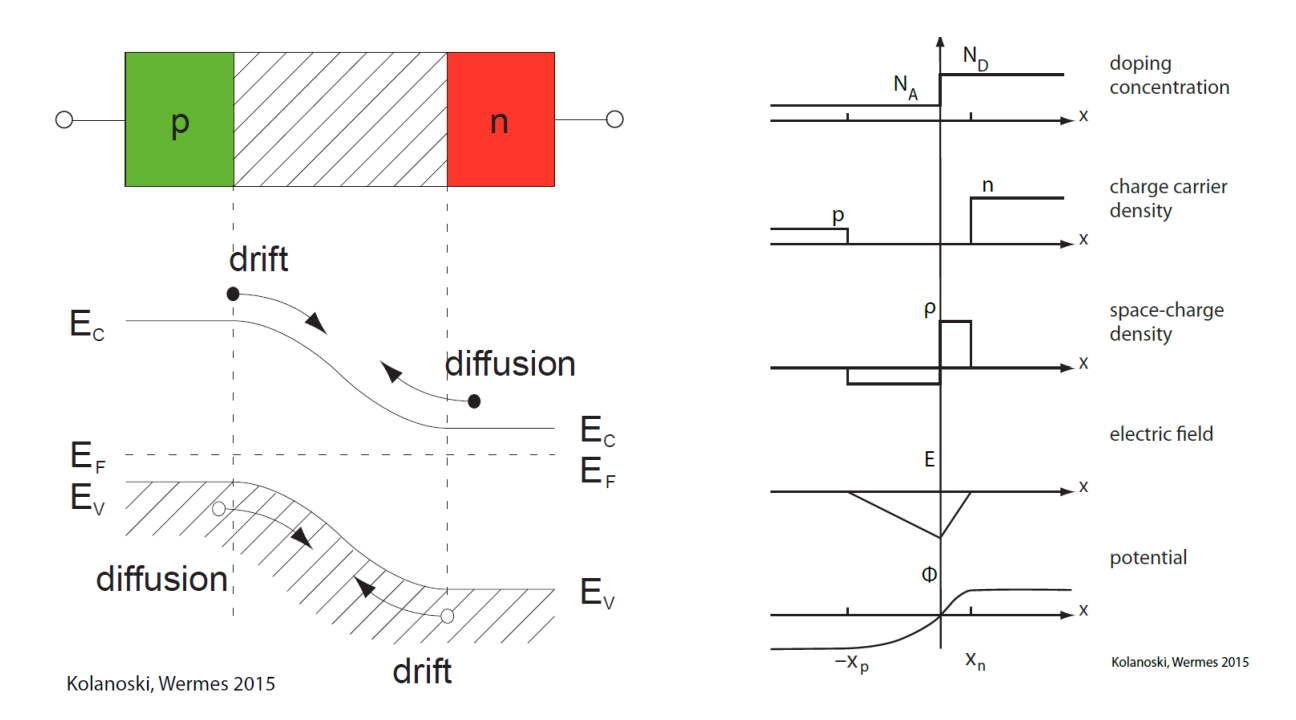


Figure 9: (left) Simplified illustration of the energy levels across a pn junction in equilibrium [1].

(right) Illustration of the doping concentration, space-charge density, field, and potential of a pn junction [1].

The potential difference of the space charge is called the built-in voltage, which consists of 0.6 V for silicon [1].

For the equilibrium, when no external voltage is present, the charge density $\rho(x)$ depends on the doping and can be described as:

$$\rho(x) = \begin{cases} -eN_A & \text{for } -x_p < x < 0, \\ +eN_D & \text{for } 0 < x < x_n. \end{cases}$$
 (12)

Here, x_n and x_p represent the depths of the space charge zones, while N_A and N_D are the acceptor and donor impurity concentrations. Outside the depletion region, the semiconductor remains electrically neutral and the following boundary condition applies:

$$E(-x_p) = E(+x_n) = 0 (13)$$

The neutrality condition of the semiconductor determines, that the number of charge

carriers in both parts of the depletion region must be equal:

$$N_A x_p = N_D x_n \tag{14}$$

With Eq. 12, 13 and 14 and the one-dimensional Maxwell equation, the electrical field can be calculated as:

$$E(x) = -\frac{d\varphi(x)}{dx} = \begin{cases} \frac{-eN_A}{\varepsilon}(x + x_p), & -x_p < x < 0, \\ \frac{+eN_D}{\varepsilon}(x - x_n), & 0 < x < x_n. \end{cases}$$
(15)

 ε is the dielectric constant [1].

An external voltage can be utilized to disturb the equilibrium and change the width of the depletion region. For silicon sensors, reverse bias is used to increase the depleted volume. In reverse bias mode, the external voltage follows the direction of the built-in voltage, which leads to a growing electrostatic potential. This reduces the diffusion current and as a result, the depletion region widens.

The capacitance of the junction can be derived from the following equation:

$$C = \varepsilon \cdot \frac{A}{d} = \varepsilon \cdot \frac{A}{x_n + x_p} \tag{16}$$

Here, A is the junction area and d the thickness of the depleted region. Therefore, the junction capacitance decreases for increasing thickness of the depletion region, realized by applying reverse bias [1, 12].

3.4 Metal-Oxide-Semiconductor Field-Effect Transistors

The metal-oxide-semiconductor field-effect transistor (MOSFET) acts as an electronic switch or amplifier by controlling the current that flows between its drain and source. A schematic of the MOSFET is displayed in Fig. 10.

There are two types of MOSFETs: NMOS and PMOS. NMOS refers to the n-type MOSFET with a channel between source and drain formed by electrons and controlled via a positive gate bias. The PMOS describes the p-type MOSFET with a channel of holes that is steered via a negative gate bias. In the following, the working principle of a MOSFET is described for the NMOS, for which a schematic is provided in Fig. 10. However, all characteristics are also applicable to the PMOS counterpart.

The n-type MOSFET possesses a p-type substrate, which in this case consists of p-doped Silicon. Two n⁺-regions, designated as the source and drain, are implemented on this substrate, forming two pn junctions. In between the source and the drain, a layer of SiO_2 is located that acts as an insulator. A metal contact on top of this insulator, which is referred to as the gate, can be supplied with a bias voltage, effectively creating a MOS capacitor. When a positive voltage is applied to the gate, the holes of the p-substrate are repelled from the vicinity of the insulator layer, leaving behind negatively charged acceptor ions. Essentially, a depletion region is created. If the gate voltage V_G exceeds a threshold voltage V_{th} , minority charge carriers (electrons) are attracted to the area below the gate, forming a conductive channel, which enables a current to flow from source to drain. The channel width and therefore the flowing current increases for increasing gate voltage. Other parameters that influence the behavior of the transistor are the channel length, the insulator thickness, the junction depth and the substrate doping [13, 14].

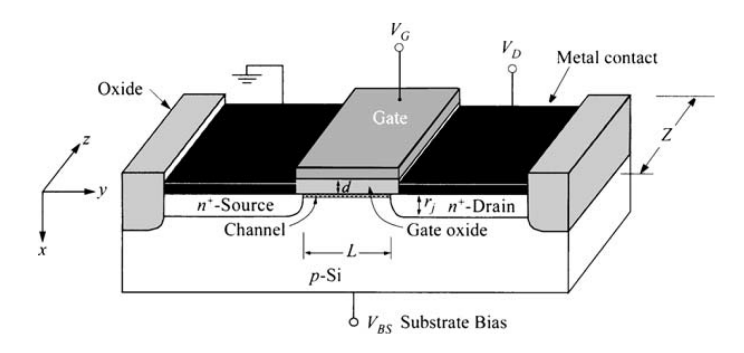


Figure 10: Schematics of a MOSFET [13].

3.5 Working Principle of MAPS

Monolithic Active Pixel Sensors (MAPS) are sensors for visible light as well as ionizing particles and utilized as particle tracking systems in various particle physics experiments. These MAPS are sensors based on silicon semiconductor technology and complementary metal-oxide-semiconductor (CMOS) technology. The CMOS technology is used for the in-pixel electronics, which consists of complementary logic in which both NMOS transistors and PMOS transistors are implemented on the same substrate. In MAPS, the silicon pixel sensor is integrated with the CMOS electronics circuitry, which is why the sensor is called monolithic [1, 15].

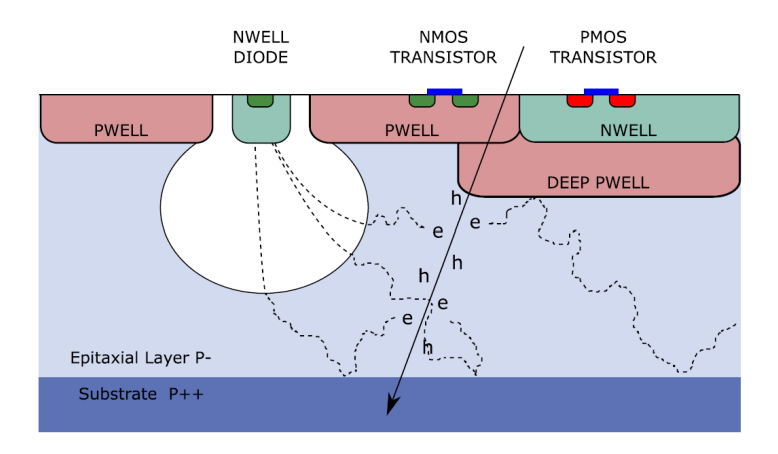


Figure 11: Schematic cross section of ALPIDE as an example for a MAPS [15].

In Fig. 11 the cross section of an exemplary MAPS can be seen, which depicts an ALPIDE. Above a highly p-doped silicon substrate (P++), which primarily acts as mechanical support, the less p-doped epitaxial layer (P-) is located, which forms the active volume of the sensor. At the top of the epitaxial layer, a collection diode is implemented, which consists of an n-well in the p-doped epitaxial layer. The resulting pn junction causes the formation of a depletion region, which is expandable by applying a reversed bias voltage between the n-well and the P++ substrate. The CMOS technology on the sensor is realized by implementing the transistors in oppositely doped wells to ensure proper functionality. Consequently, NMOS transistors are embedded inside p-wells and PMOS transistors inside n-wells. In order to avoid pn junctions to be formed by n-wells and the p-doped epitaxial layer, which would create diodes in competition to the collection diode, the n-wells are enclosed in additional deep p-wells. The utilization of deep p-wells is specific to the ALPIDE and also the MOSS design.

When a particle traverses the epitaxial layer, displayed in Fig. 11 by the black arrow, electron-hole pairs are generated by ionization. When the produced electrons, which are displayed in Fig. 11 by the dotted lines, are located in an undepleted region, diffusion is the dominating process. As soon as electrons enter the depletion region, drift dominates due to the present space charge, which causes the electrons to drift towards the collection diode. The charge travelling close to the collection diode induces a signal voltage by discharging the pixel capacitance. This signal voltage ΔV_{signal} depends on the collected charge Q and the pixel capacitance C:

$$\Delta V_{signal} = \frac{Q}{C} \tag{17}$$

The pixel capacitance C results from the junction capacitance of the collection diode (Eq. 16) and the parasitic capacitance of the circuitry. A high Q/C ratio lowers the power consumption of the in-pixel electronics and improves the signal-to-noise ratio. Applying reverse bias between the collection diode and the substrate, which expands the

depletion region, reduces the junction capacitance and therefore the pixel capacitance, which elevates the Q/C ratio. A smaller n-well of the collection diode leads to a reduced pixel capacitance, but at the same time to less collected charge. When increasing the thickness of the epitaxial layer, more charge can be deposited by traversing particles. However, a thicker epitaxial layer correlates with more undepleted space, resulting in more domination of the diffusion process, resulting in reduced charge collection efficiency as well as reduced radiation hardness [12, 16].

The induced signal voltage in the collection diode is further shaped and processed by the CMOS in-pixel circuitry. Due to the signal voltage from the diode, the presence of a traversing, ionizing particle can be detected [15].

4 The Monolithic Stitched Sensor (MOSS)

The Monolithic Stitched Sensor (MOSS) is a MAPS developed for the upgrade of the Inner Tracking System of the ALICE project (ITS3), which pioneers new grounds as a bendable wafer-scale sensor. The MOSS represents not yet the final chip for the ITS3, but the first stitched prototype with dimensions of $14 \,\mathrm{mm} \times 259 \,\mathrm{mm}$. The primary aim for the MOSS is to explore the stitching technique, the yield and the electrical performance [17]. In this chapter, the design, production, architecture and the analog in-pixel front-end electronics of MOSS are explored, along with the characteristics of BabyMOSS, a smaller test chip that is described later in this chapter.

4.1 Pixel Design

Fig. 12 shows the cross section of the pixel design used for the MOSS.

The predecessor sensor ALPIDE (Fig. 11) was produced with the 180 nm CMOS imaging process of Tower Partners Semiconductor Co., Ltd. (TPSCo) [18] with an epitaxial layer of 25 µm width [8]. The MOSS, which is produced with 65 nm technology by the same company, has a thinner epitaxial layer in comparison with 10 µm [8]. Consequently, the extension of the depletion is more limited for the MOSS and thus the pixel design needs to be adjusted. The primary difference to the pixel design of ALPIDE is the implementation of a low dose deep n-type implant with a gap near the pixel edges. This achieves full depletion of the epitaxial layer with the help of reverse bias, which can be applied between the collection diode and the substrate.

As a result, the charge collection depends dominantly on drift compared to diffusion. This reduces charge sharing with neighboring pixels, but increases the detection efficiency [8].

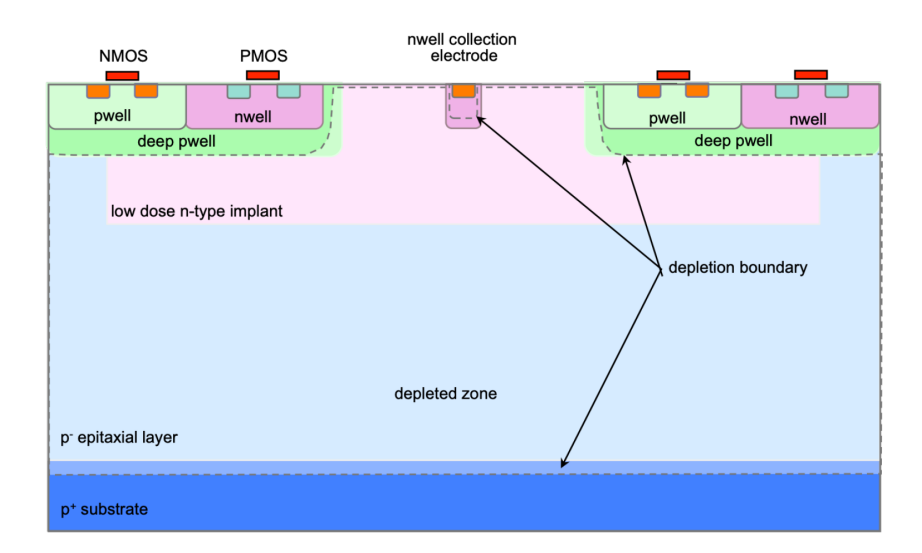


Figure 12: Cross section of the pixel design of MOSS not to scale [8].

4.2 Production and Chip Architecture of MOSS and BabyMOSS

The MOSS is a Monolithic Active Pixel Sensor produced with TPSCo 65 nm CMOS technology on silicon wafers of 300 mm diameter [8].

The process used for implementing the CMOS circuitry on the wafer is photolithography. During this process, a layer of photoresist is applied to the wafer and the pattern of a masking reticle is transferred to the wafer by exposing the reticle to UV light. Further information on photolithography can be found in [19].

The dominant limiting factor to the resolution is diffraction and coherent light is used to attenuate this diffraction. The necessity of coherent light establishes an upper limit on the size of the masking reticles and the pattern of the reticle is repeatedly transferred until the entire wafer is covered [19].

As a result, the length and width of a chip is limited by the reticle size to a few centimeters. In order to create a sensor that exceeds these limits, a technique called stitching is employed. For stitching, every lithography step is aligned with the preceding one. Continuous metal traces can then bridge the lithography boundaries and create interconnections between the chips [17].

For creating the MOSS, ten Repeated Sensor Units (RSUs) are stitched together in one dimension. One RSU consists of a chip with endcaps at the short edges. These endcaps are connected to the chip via a stitched communication backbone that traverses the whole RSU in longitudinal direction. In order to then stitch RSUs together, metal stripes connect the left endcap of one RSU with the right endcap of the next RSU. In the end, the RSUs can be supplied, controlled and read out in longitudinal direction via the stitching and interfaces on the far left endcap.

Additionally, there is also the possibility to supply, control and read out the individual RSUs via the long edges [8].

Each RSU is divided in two half units, designated as the top unit and bottom unit, which are fully standalone functional. Each unit consists of four equally sized pixel matrices, or regions, with varying pixel pitches between the top and bottom unit. The top unit comprises regions containing 256×256 larger pixels with a pitch of $22.5 \,\mu\text{m}$, whereas a region of the bottom unit contains 320×320 finer pixels with a pitch of $18 \,\mu\text{m}$. The full MOSS with ten RSUs comprises $6.72 \,\text{million}$ pixels [8].

In Fig. 13, the MOSS, a single RSU and the readout schematics of MOSS are displayed.

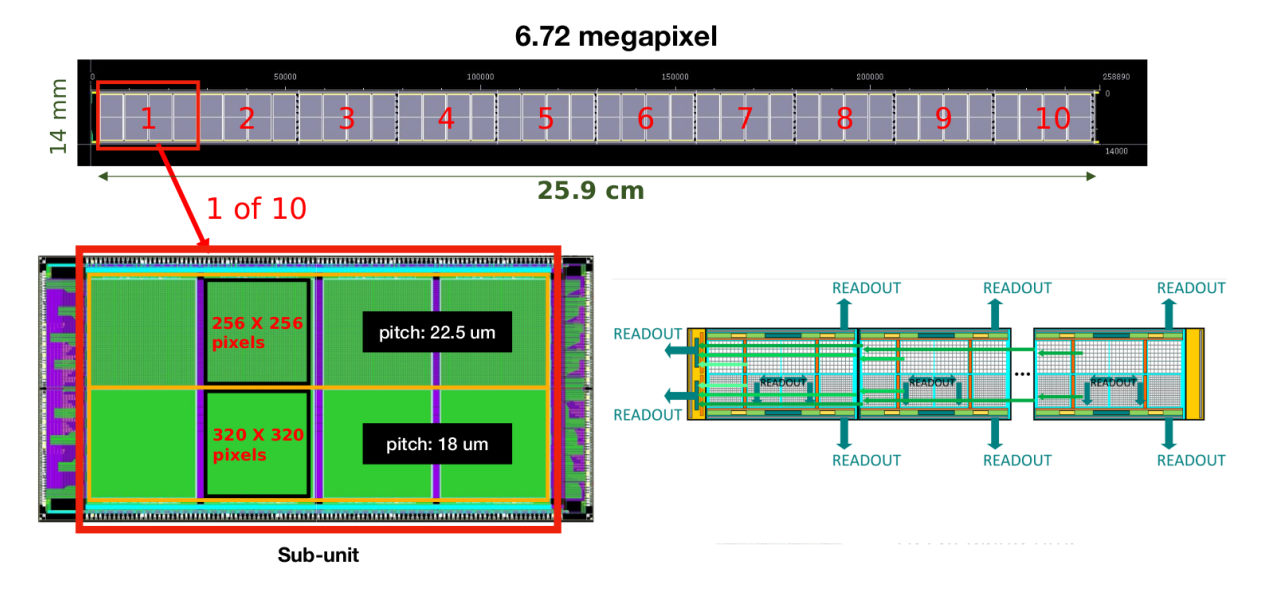


Figure 13: Structure of MOSS [20].

Given that the MOSS has a length of 259 mm, which is almost as long as the 300 mm wafer it is produced on, only six MOSS can fit on a single wafer. The remaining space on the wafer is utilized for the fabrication of test chips consisting of individual RSUs. This is illustrated in Fig. 14.

These test chips are referred to as BabyMOSS and the only difference to an RSU of MOSS is that the endcaps are not stitched to other endcaps.

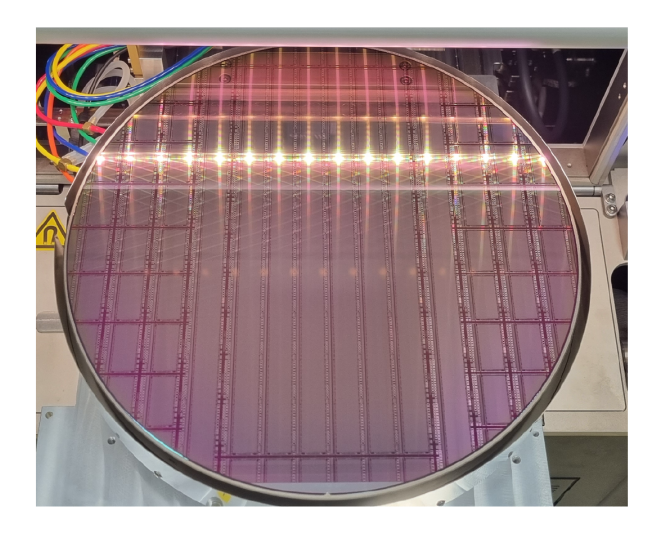


Figure 14: Picture of a wafer that contains six MOSS and several test chips [8].

The BabyMOSS is the sensor examined in this study. The regions of the top unit are referred to as top 0, top 1, top 2 and top 3. The regions of the bottom unit are referred to as bottom 0, bottom 1, bottom 2 and bottom 3.

In plots of data from BabyMOSS, the results for the eight regions are displayed separately, mirroring the arrangement of the pixel matrices on the sensor.

The specific BabyMOSS that is employed in this study is the babyMOSS-1_2_W22C7. This BabyMOSS possesses a malfunctioning region, which is region top 0. For this region, the readout gets stuck at row 0 when executing a scan, which is why the region is permanently disabled and not examined within this study.

4.3 Analog In-Pixel Front-End

The analog in-pixel front-end electronics is responsible for the initial processing of the analog signal from the collection diode before its conversion to a digital signal. This processing comprises amplification, pulse shaping and discrimination of the signal [1]. A schematic of the analog in-pixel front-end can be observed in Fig. 15. For NMOS transistors, the arrow points toward the source and for PMOS transistors the arrow points away from the source [14]. The transistors are numbered from M0 to M11. The red labels at the transistors name the 8-bit Digital-to-Analog Converters (DACs), which can be manually configured to adjust the behavior of the corresponding transistor.

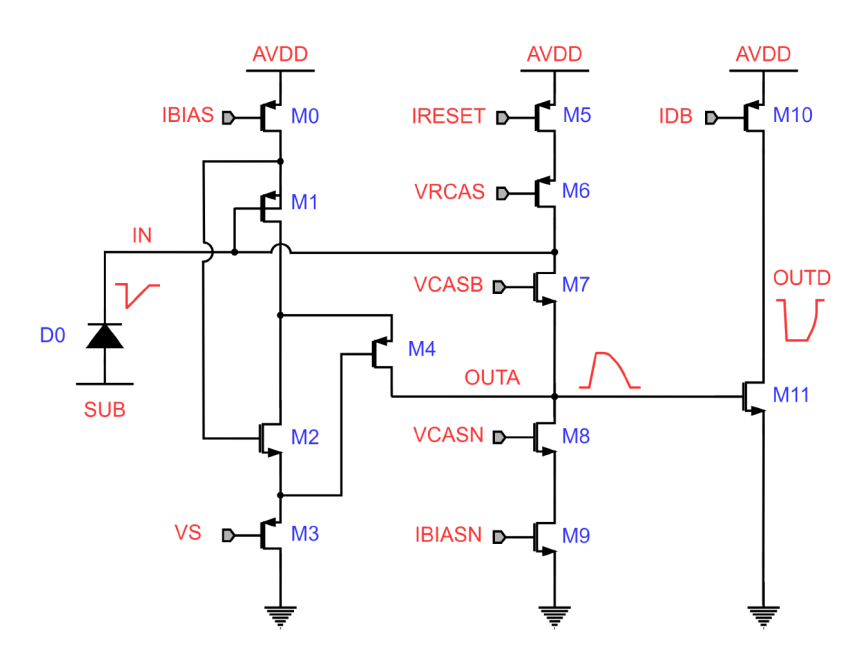


Figure 15: Simplified schematic of the analog in-pixel front-end [20].

In this study, the April 2024 DAC settings for the BabyMOSS are used for laboratory scans and test beam data taking, which are referred to as the default DACs going forward. These settings were determined through testing before a standard has been defined. The DAC settings are listed in Tab. 1 as well as the standard DACs that were released by CERN in July 2024. The behavior of the BabyMOSS for the DACs utilized in this study is expected to exhibit some variations to the behavior with the standard DACs.

	April 2024 DACs	July 2024 Standard DACs
	(Default DACs)	
IBIAS	25	62
IBIASN	40	100
IDB	25	50
IRESET	10	10
VCASB	15	15
VCASN	51	64
VPULSEH	42	70
VSHIFT	191	192

Table 1: DAC settings for BabyMOSS

For testing purposes, there are differences in the front-end electronics implemented for different regions. The individual differences for each region are specified in Fig. 16.

	Region 0	Region 1	Region 2	Region 3
ТОР	Standard	Larger input transistor (M1)	Larger discriminator input transistor (M11)	Larger common-source transistor (M2)
воттом	Standard	Standard	Standard	Slightly different layout

Figure 16: Differences in the front-end electronics within the RSU [20].

5 Laboratory Scans

In Fig. 17, the BabyMOSS test system for laboratory scans is depicted. The BabyMOSS sensor is wire-bonded to a carrier card and secured inside a black plastic casing. Fig. 18 displays the BabyMOSS on the carrier card without the protective casing. The carrier card, which hosts and connects the sensor, is connected to a raiser board, which is in turn connected to a DAQ board.

The DAQ board supplies the BabyMOSS with power, communicates with the sensor and provides the readout via a field-programmable gate array (FPGA), which is programmed with custom firmware. The DAQ board is connected to the computer via USB.

The raiser board acts as an interface between the DAQ board and the carrier card and is utilized for controlling and reading out the BabyMOSS. By using adapter boards like this raiser board, already existing DAQ boards can be utilized for a multitude of setups [21].

The DAQ board can be connected to a 0Ω shunt, which shortens the substrate and the nwell diode, putting them both at the same potential. This effectively results in 0V reverse bias for the BabyMOSS. The DAQ board can also be connected to the power supply, which provides a reverse bias of -1.2V, leading to an expanded depletion region within the sensor, as described in chapter 3.5. The reverse bias is set via the parameter VBB.

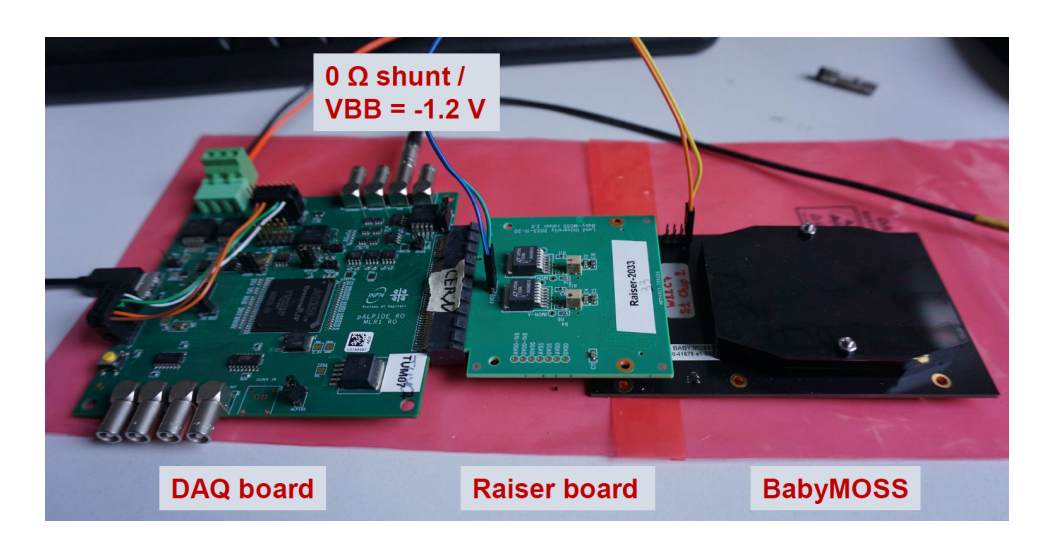


Figure 17: BabyMOSS laboratory test system.

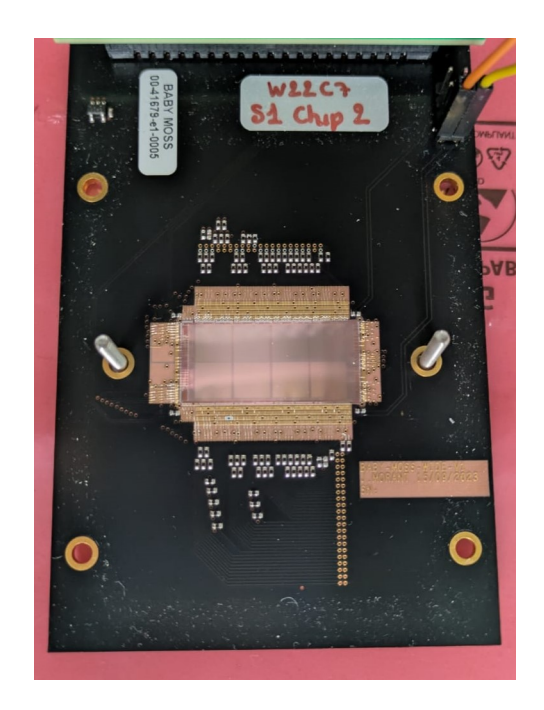


Figure 18: The BabyMOSS mounted on the carrier card.

5.1 Threshold Scan

The in-pixel front-end circuitry, introduced in chapter 4.3, operates with a continuously active discriminating amplifier. A signal, in the form of a voltage drop, gets discriminated after being amplified and shaped in the in-pixel front-end electronics. The discriminator decides if a signal is further processed, depending on whether or not the signal exceeds a charge threshold that is set by the user. Upon receiving a strobe signal (which can be given by an external trigger or initiated by an internal sequencer), the discriminated signal is latched into in-pixel memory and a hit is recorded for the respective pixel, resulting in binary pixel hit data [8, 22].

Chapter 3.5 describes how an impinging particle can create a signal voltage by generating electron-hole pairs.

A number of on-chip DACs control the signal shape and detection threshold. For fixed DAC settings, the sensor detection threshold is fixed at a specific value. To assess this value, threshold scans are performed using the pulsing circuitry available in each pixel. A small capacitor is used to inject a controlled amount of charge prior to the amplifier. The procedure involves sequentially injecting test charges $Q_{\rm inj}$ into the pixel front-end in steps of 1 DAC unit. These test charges are produced by a pulsing voltage $V_{\rm PULSE}$, which is applied over the capacitor with the capacitance $C_{\rm inj}$. After each pulse, the capacitor discharges, depositing a controlled amount of charge $Q_{\rm inj}$ into the pixel, given by:

$$Q_{\rm inj} = C_{\rm inj} \cdot V_{\rm PULSE} = C_{\rm inj} \cdot (V_{\rm PULSEH} - V_{\rm PULSEL}) \tag{18}$$

For each $Q_{\rm inj}$ value, the charge is injected a number $N_{\rm inj}$ of times. A number of those injections will pass the set threshold and assert the response of the pixel. The probability to have a response, given by the ratio $N_{\rm hit}/N_{\rm inj}$, resembles an S-curve and is shown in Fig. 19 as a function of the injected charge. The point where the hit fraction is 50% is defined as the threshold of the pixel under test. This can be repeated for all pixels in the matrix. Due to manufacturing variations, the 50% point will have a spread [12].

For the BabyMOSS, V_{PULSEL} defaults to 0 and V_{PULSEH} is set with the corresponding DAC parameter VPULSEH.

The DAC range of VPULSEH is $N_{\rm DAC} = 256$ [23] and the voltage range $V_{\rm DAC} = 1.2$ V, specific to the 65 nm CMOS technology. The design value for the capacitance is $C_{\rm inj} = 240$ aF [24]. Conservatively, the uncertainty is estimated to be 50%. The exact value for the capacitance is still under investigation. The uncertainty of $V_{\rm DAC}$ can be assumed to be negligible compared to the uncertainty of $C_{\rm inj}$ caused by the production process. With these values, the number of electrons per DAC of VPULSEH can be determined:

$$N_{\rm e} = \frac{V_{\rm DAC} \cdot C_{\rm inj}}{N_{\rm DAC}} \approx (7 \pm 3.5) e \tag{19}$$

Since the exact value of the capacitance is still under investigation, the charge will generally be expressed in units of DAC of the VPULSEH parameter.

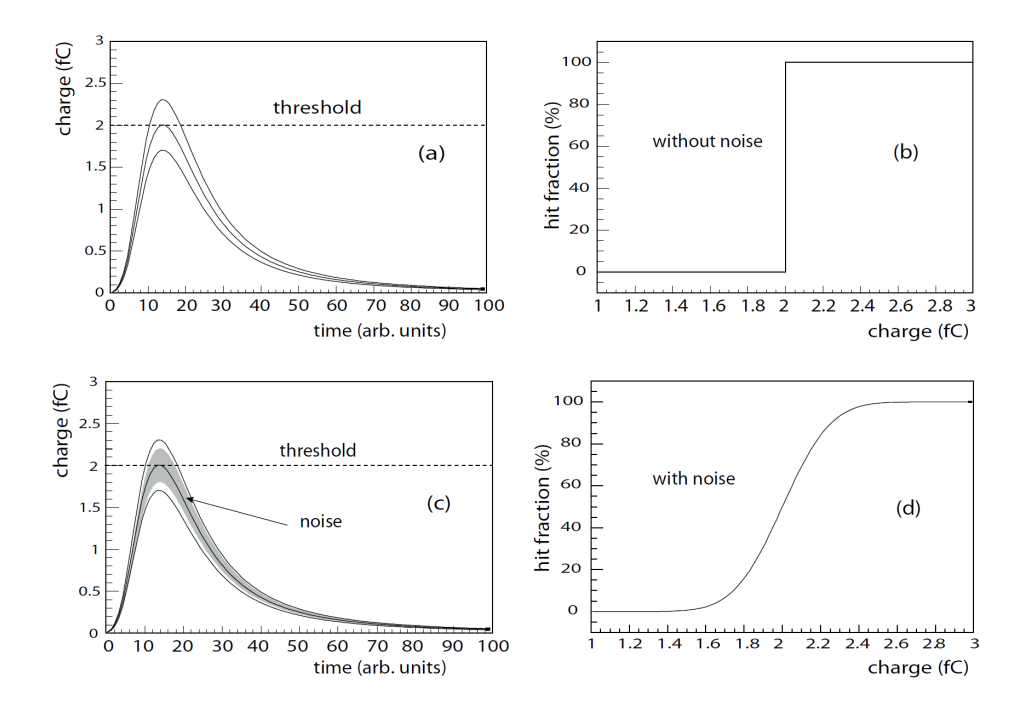


Figure 19: The principle of a threshold scan on a pixel sensor. (a) Three separate signals, one of which exceeds the set threshold value. No noise is present in the system. (b) Above the set value of the threshold, the hit probability is 100%, showing a sharp onset, due to the lack of noise. (c) Three signals, one of which has an uncertainty band, due to the noise present in the system. (d) The subsequent hit probability gets smeared around the charge threshold due to the noise present [1].

Fig. 19 illustrates the concept of a threshold scan for a single pixel. Panels (a) and (c) show exemplary signals of injected charge with varying amplitudes relative to the discriminator threshold, while panels (b) and (c) show the corresponding hit probability as a function of the charge.

Under ideal conditions where no noise is present, as shown in panels (a) and (b), the detector registers no hits when the injected charge is below the discriminator threshold. Once the injected charge exceeds the threshold, the hit probability has a sharp onset.

However, in real-world scenarios, temporal electronic noise is present, which describes time-dependent fluctuations of the signal, as illustrated in panels (c) and (d). The noise introduces fluctuations in the signals, resulting in a gradual, S-shaped transition of the hit probability curve rather than a sharp step. This noise is typically Gaussian, which allows the hit probability to be modeled using a Gaussian error function:

$$\frac{N_{\text{hit}}}{N_{\text{inj}}} = \frac{1}{2} \left[1 + \text{erf}\left(\frac{Q_{\text{inj}} - \mu}{\sqrt{2}\sigma}\right) \right]$$
 (20)

The threshold value, defined as the charge at which the pixel asserts a hit fraction of 50 %, is extracted from the inflexion point of the S-curve, represented by μ , while the width σ quantifies the noise [1, 12].

The threshold is set globally for the whole pixel matrix by the combination of DAC values chosen by the operator. In order to characterize the pixel sensor as a whole, the average threshold is calculated using the distributions of all single pixel thresholds.

Results of a threshold scan conducted with the BabyMOSS for the default DACs (Tab. 1) can be seen in Fig. 20. In this study, the VPULSEH covers the range of 0 to 70 DAC units in steps of 1 DAC and 25 injections per VPULSEH value were used. The temporal noise distributions are displayed in Fig. 21. Since the BabyMOSS is still an experimental sensor and the readout via the the stitched backbone is currently under development, the control and readout of the sensor takes place via the long edge.

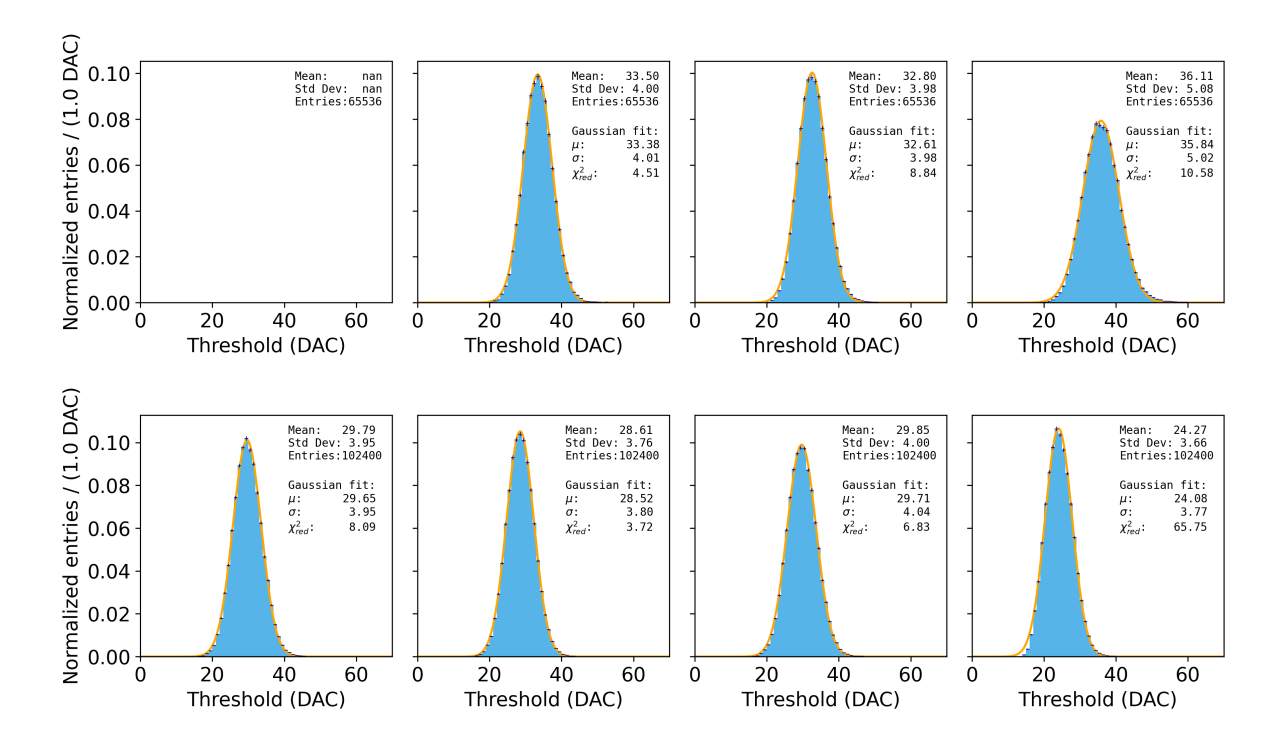


Figure 20: Threshold distributions for the default DACs at $VBB = 0\,V$. In dark blue, the y-errors represent the normalized bin errors, while the x-errors correspond to the bin width. The panels depict the eight regions of the BabyMOSS.

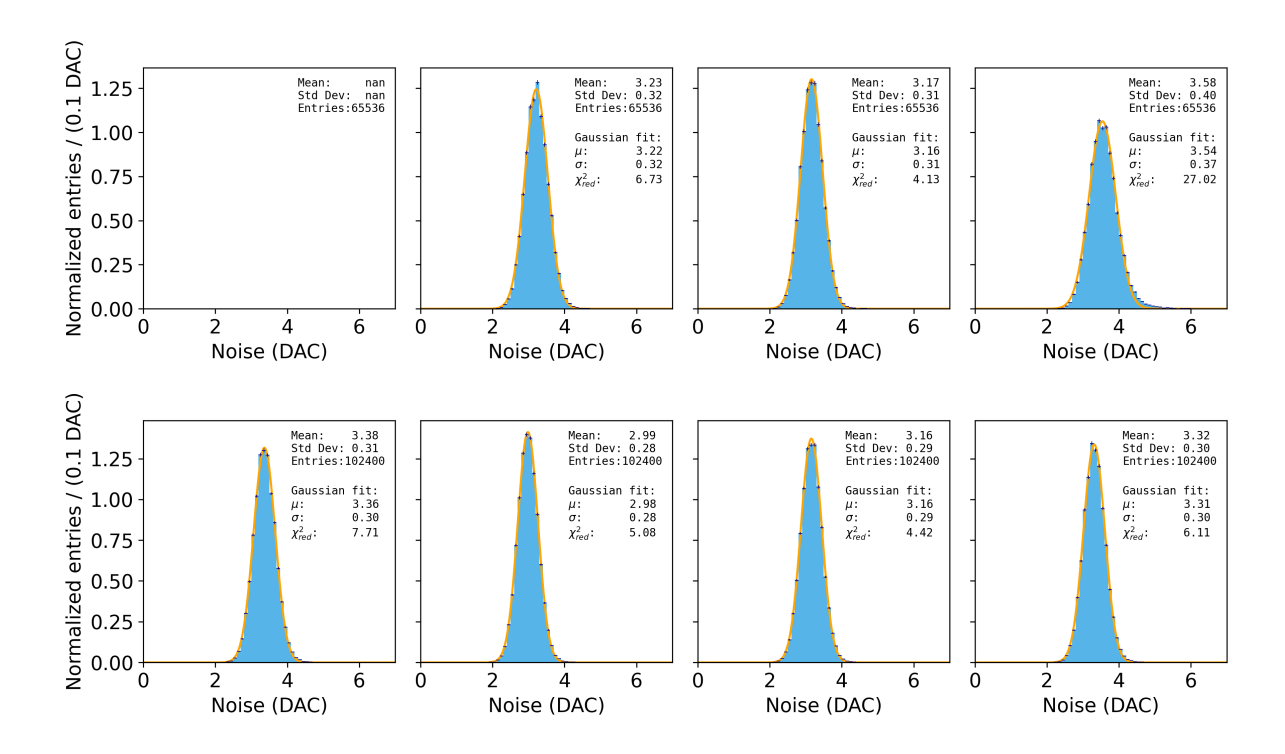


Figure 21: Noise distributions for the default DACs at VBB = 0 V. In dark blue, the y-errors represent the normalized bin errors, while the x-errors correspond to the bin width. The panels depict the eight regions of the BabyMOSS.

The mean (\bar{x}) and the standard deviation (σ_x) are calculated as follows with n as the number of entries, which represent the total number of pixels in the pixel matrix:

$$\bar{x} = \frac{1}{n} \sum_{i=1}^{n} x_i \tag{21}$$

$$\sigma_x = \sqrt{\frac{1}{n} \sum_{i=1}^{n} (x_i - \bar{x})^2}$$
 (22)

The normalized bin errors, represented by σ_{y_i} , are calculated based on Poisson statistics with N_i as the bin count and Δx as the bin width:

$$\sigma_{y_i} = \frac{\sqrt{N_i}}{n \cdot \Delta x} \tag{23}$$

Region top 0 is malfunctioning and disabled as previously mentioned in chapter 4.2. For the remaining regions, the average thresholds vary between 24 and 36 DAC units, which equals to a charge of about 168 ± 84 to 252 ± 126 electrons (Eq. 19). This difference is caused by the variations in the front-end electronics of the eight regions, which were implemented for testing purposes (Fig. 16). Each region results in an individual threshold for the same global DAC settings. Ideally, each region would be assigned a specific set of DACs in order to achieve a uniform threshold over the whole sensor, which would be of

advantage for the comparison of the behavior of the different regions. At the time of this study, only global settings could be set for the BabyMOSS. Recently, the possibility to apply specific DAC settings per region became available. Later in this study, different datasets are combined to obtain a global threshold.

The spread of the threshold distributions, quantified by the standard deviation, stays at about 4 DAC units for all regions except for region top 3, which has a standard deviation of 5.08 DAC units.

The average temporal pixel noise is located in a range of 3 to 4 DAC units, with region top 3 exhibiting the highest average noise. Additionally, region top 3 displays the larges spread of the temporal noise distribution with 0.40 DAC units, while the standard deviation stays near 0.30 DAC units for the remaining regions.

Overall, region top 3 stands out as the region with the highest noise per pixel and the broadest distribution of pixel thresholds around the mean. These effects are considered to be due to the larger common-source transistor used in the analog in-pixel front-end electronics of this region.

The distributions of threshold and noise resemble a Gaussian distribution. Consequently, a Gaussian function is fitted to the distribution with the mean μ and the standard deviation σ :

$$f(x) = a \cdot \exp\left(-\frac{1}{2} \frac{(x-\mu)^2}{\sigma^2}\right) \tag{24}$$

To measure the goodness of the fit, $\chi^2_{\rm red}$ is calculated for each fit:

$$\chi_{\text{red}}^2 = \frac{1}{\text{doF}} \sum_{i=1}^m \left(\frac{y_i - y_{\text{fit},i}}{\sigma_{y_i}} \right)^2 \tag{25}$$

In this equation, m represents the number of bins on the x-axis and doF is an abbreviation for the number of degrees of freedom, which is calculated as the number of fit parameters subtracted from the number of data points.

We expect a value of $\chi^2_{\rm red} \approx 1$ for a good fit. However, the produced $\chi^2_{\rm red}$ for both threshold and noise distributions exceeds this value.

For the noise distributions, the $\chi^2_{\rm red}$ ranges from 4.13 to 27.02, indicating a deviation from the Gaussian distribution for all regions. For the highest $\chi^2_{\rm red}$ of 27.02 in region top 3, the tail of the noise distribution towards higher DAC units visibly exceeds the Gaussian distribution, which implies that some pixels exhibit an especially high temporal noise. For the threshold distributions, the $\chi^2_{\rm red}$ ranges from 3.72 to 65.75, indicating that all distributions are not well represented by a Gaussian. The variance of $\chi^2_{\rm red}$ in between the regions is influenced by the changes in transistor structures and layouts.

The width and shape of the threshold distributions stem primarily from pixel-to-pixel differences. These pixel-to-pixel differences arise from production-related variations in the transistors of the in-pixel electronics, which occur in a spatially stable pattern throughout the sensor. The resulting unwanted variations in the behavior of the pixels are referred to as fixed-pattern noise (FPN) [12]. Due to the stable pattern of the FPN, the threshold and noise distributions resemble a Gaussian distribution. However, deviations from perfect Gaussian distributions are expected due to manufacturing variations, which result in a stable but presumably not perfectly uniform pattern.

Additionally, it was observed for BabyMOSS that the 2D distribution of average thresholds displays four stripes of pixels with lower thresholds in all regions (Fig. 22). This is known to occur for BabyMOSS, but not for MOSS.

In both sensors, parallel power tracks are implemented, with one track connecting to a given RSU. At the edge of one RSU all power tracks hop to the track next to it, which is referred to as power-hopping. For BabyMOSS, which consists of one RSU, only one metal power-hopping line is needed and wire-bonded, leaving the remaining unused power-hopping lines floating. This causes coupling noise in the circuit, which in turn results in stripes of pixels that exhibit lower thresholds. Wire-bonding the unused power-hopping lines to ground has been demonstrated to result in a significant reduction of the stripes, leaving only very thin stripes of pixels exhibiting lower thresholds. Compared to the average threshold exhibited by pixels outside of these stripes, the threshold within the stripes is lower by approximately 2 to 3 DAC units [25]. This effect is still under investigation.

In the end, these pixel stripes of lower threshold can be expected to have an influence on the threshold distribution. However, if this were the primary cause for the deviation of the threshold distribution from a Gaussian fit, one would expect to observe an increased number of pixels in the lower threshold tail, causing a discrepancy from the fit. Yet, the data in fact tends to fall below the fit in the lower tail of the threshold distribution and above the fit for the higher threshold tail, which is especially visible in region bottom 3, where $\chi^2_{\rm red}$ is the highest. This indicates that the origin for the deviation from the Gaussian distribution remains within manufacturing variations of the FPN.

Considering that the Gaussian fit does not describe the threshold distribution sufficiently, the average threshold retrieved from the data directly represents the characteristics of the pixel matrices more accurately. Therefore, these values will be utilized for further analysis whenever the average threshold is considered.

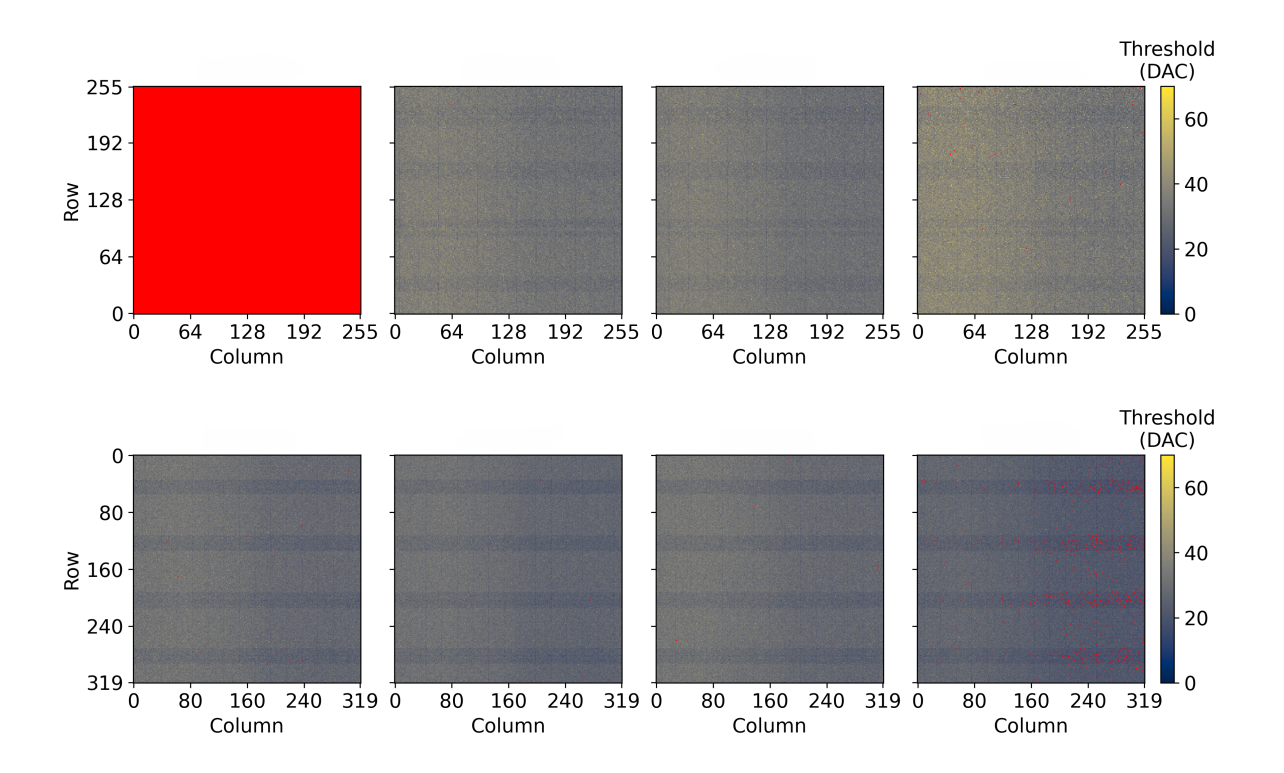


Figure 22: 2D distributions of average thresholds for the default DACs at VBB = 0 V. The panels depict the eight regions of the BabyMOSS.

Fig. 23 depicts the noisy pixels detected while performing the threshold scan using the default DACs, which produce the thresholds displayed in Fig. 20. A pixel is classified as noisy if it exceeds a predefined fake-hit rate. The fake-hit rate is the number of hits per pixel per unit time (or per event) in the absence of any external stimuli. During the threshold scan, the pulsing is executed row by row and if a pixel fires, even though it is not located in the row that currently is injected with charge, the detected hit is considered a fake-hit. However, the fake-hit rate should only be interpreted as an estimator, since capacitive coupling between pixels can act as an external stimulus when neighboring rows are pulsed. To classify pixels as noisy, the estimated critical fake-hit rate is set to one hit per pixel per hour, motivated by the approximate duration of the threshold scan for default DACs. Ultimately, all pixels identified as noisy are masked, meaning they are excluded from further data analysis.

In Fig. 23, an especially high number of noisy pixels is visible for region bottom 3 with a further increased number of noisy pixels within the stripes of lower threshold. The exact amount of noisy pixels can be found in Tab. 2. The reason for this occurring only for region bottom 3 can be traced back to the lower overall threshold of this region. For the applied DAC settings, this region exhibits the lowest mean threshold overall, approximately 5 DAC units lower than the second-lowest threshold.

Leaving aside the striped pattern previously explained, the distribution of noisy pixels in the bottom 3 region seems to indicate an increase in the second half of the matrix,

towards larger column numbers. This is unexpected and further investigated in chapter 7.

Fig. 24 shows the distribution of bad pixels, which are pixels that do not exhibit any response at all. These pixels are permanently defective and excluded from the data analysis. The only region to exhibit bad pixels, excluding the disabled region top 0, is region top 3. Region top 3 exhibits 44 bad pixels (Tab. 2), which amounts to 0.07% of the total pixel count. The amount of bad pixels within this region seems to increase marginally for higher rows.

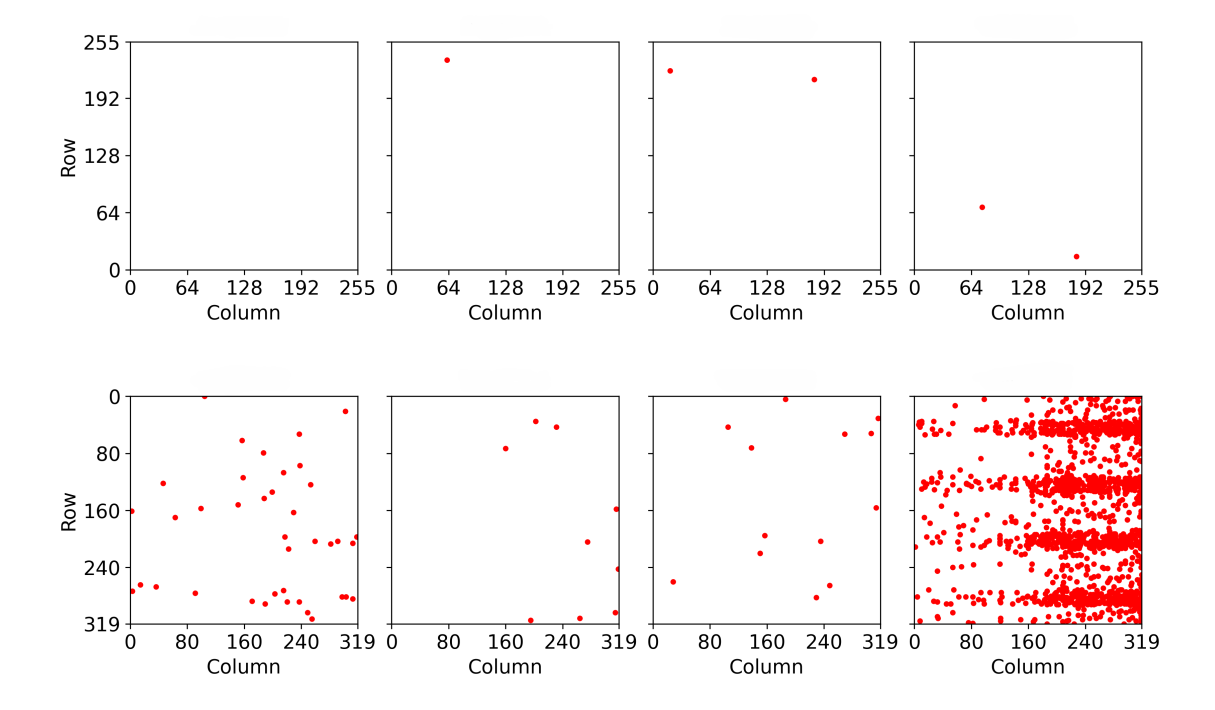


Figure 23: Distribution of noisy pixels for the default DACs at VBB = 0 V. The panels depict the eight regions of the BabyMOSS.

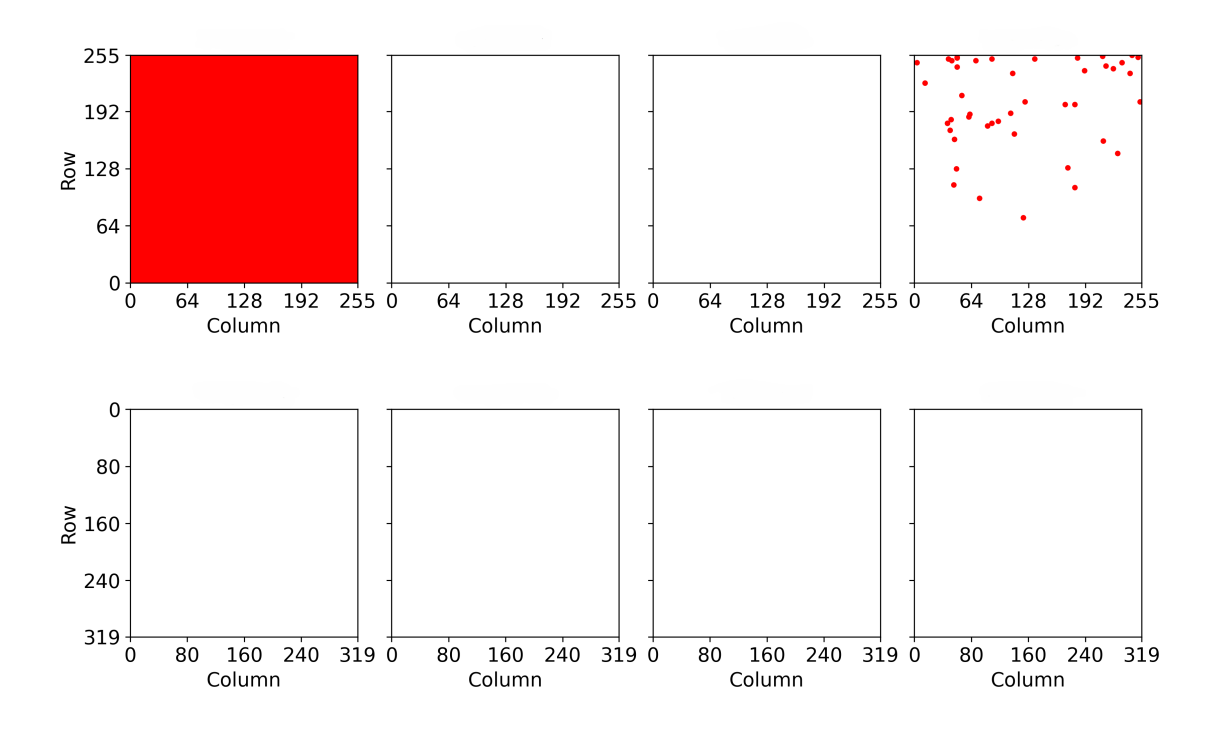


Figure 24: Distribution of bad pixels for the default DACs at VBB = 0 V. The panels depict the eight regions of the BabyMOSS.

Region	# noisy pixels	# bad pixels
Top 0	NaN	NaN
Top 1	1	0
Top 2	2	0
Top 3	2	44
Bottom 0	39	0
Bottom 1	9	0
Bottom 2	13	0
Bottom 3	1396	0

Table 2: Noisy and bad pixels for the default DACs at VBB = 0 V.

5.2 Exploration of the Threshold Range of BabyMOSS

For the MOSS and therefore also BabyMOSS, the threshold is primarily dependent on the front-end DAC called VCASB (Fig. 15). In order to characterize the BabyMOSS, the exploration of the parameter space and the associated behavior of the sensor is important. Therefore, a range of thresholds for VBB = 0 V and VBB = -1.2 V is examined by varying the VCASB value.

For an increasing VCASB value the threshold decreases and hence the fake-hit rate increases. As VCASB continues to rise, the fake-hit rate has a sharp onset, and a limit is reached when the increasing data load (due to the extra fake hits being read) becomes unmanageable, causing the threshold scan to fail. At this point, the last working VCASB

value is chosen as the upper limit. The lower VCASB limit is evaluated and chosen in relation to the upper limit, with the aim of selecting a VCASB value that remains comfortably below the optimal threshold.

For VBB = 0 V, the highest value is VCASB = 28 DAC units and the lowest value is set to VCASB = 5 DAC units with the standard value of VCASB = 15 DAC units well within this range.

For VBB = -1.2 V, the upper limit is VCASB = 104 DAC units and the lower limit is set to VCASB = 75 DAC units. When this range was determined, no standard VCASB value was known for VBB = -1.2 V. Later, colleagues from the ITS3 collaboration provided a standard value of VCASB = 84 DAC units, which lies within the explored parameter range. When reverse bias is applied, the depletion region expands and the pixel capacitance is reduced, as discussed in chapter 3.5. As a result, the signal voltage increases for the same amount of collected charge compared to the case without reverse bias. Consequently, different VCASB settings are applied when reverse bias is present, in order to adapt the signal discrimination to the new charge-to-voltage conversion.

Performing a threshold scan of all regions and pixels using the default DAC settings takes up approximately one hour. In order to make the threshold characterization for varying VCASB settings more time efficient, five rows evenly distributed over each region are used to determine a representative threshold. By carefully selecting these rows, it was avoided to place them within a stripe of pixels that show a lower threshold. Due to the pixels being pulsed row by row when performing the threshold scan, only using five rows for the scan reduces the scan time by about 98%. Selecting these five rows are shown to be enough to be representative of the full matrix, while reducing the scanning time dramatically. The threshold distributions for five rows can be seen in Fig. 25, using the same settings as for the full threshold scan (Fig. 20). As previously stated, the average threshold is derived directly from the data and no Gaussian distribution is fitted.

The average threshold values for the scan covering only five rows and for the full scan, along with the difference between them, are presented in Tab. 3. The average thresholds are rounded to whole numbers, because the threshold cannot be controlled with a precision finer than 1 DAC unit. The threshold values for a full scan and for a scan with five rows show deviations up to a maximum of 1 DAC unit. This deviation, corresponding to the smallest measurable unit, is expected and considered the error of the average threshold conducted with only five rows.

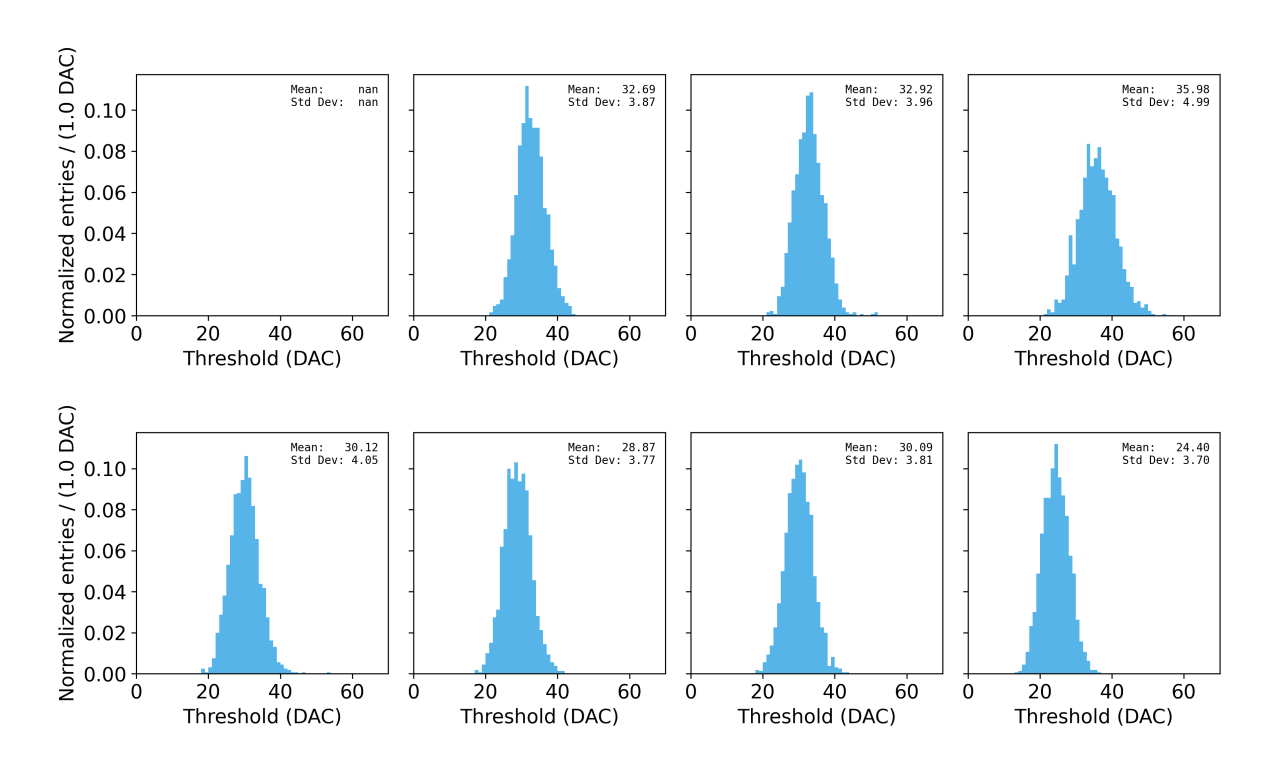


Figure 25: Threshold distributions when scanning five rows for the default DACs at VBB = 0 V. The panels depict the eight regions of the BabyMOSS.

Region	Threshold _{full scan} (DAC)	$Threshold_{five rows} (DAC)$	$\Delta_{\rm threshold}$ (DAC)
Top 0	NaN	NaN	-
Top 1	34	33	1
Top 2	33	33	0
Top 3	36	36	0
Bottom 0	30	30	0
Bottom 1	29	29	0
Bottom 2	30	31	1
Bottom 3	24	24	0

Table 3: Comparison of average thresholds for a full scan with the results of a scan of five rows.

The average threshold for every scan with VBB = 0 V is plotted against the VCASB value in Fig. 26, while in Fig. 27, the results of the threshold scans done with VBB = -1.2 V can be observed.

The relation between the average threshold and VCASB is antiproportional: A higher VCASB value results in a smaller discrimination threshold and vice versa. Increasing the VCASB value raises the gate voltage of the corresponding transistor, whose general mode of operation is discussed in chapter 3.4. This, in turn, influences the drain current. However, the overall relation between the threshold and VCASB value cannot be directly inferred from this effect alone, as it is shaped by the complex interaction of currents and voltages within the in-pixel front-end, introduced in chapter 4.3. Therefore, a more

detailed analysis would be required to determine the exact relation between VCASB and the threshold.

An exponential fit of threshold versus VCASB has been demonstrated to provide an accurate description of the data. The $\chi^2_{\rm red}$ values (Eq. 25) are displayed in Tab. 4. These values span a range of 0.01 to 0.11, indicating that the residuals between data and fit are much smaller than the error on the average threshold, which is limited by the smallest measurable unit. Overall, the exponential fit closely follows the trend of the data and seems to capture the dependency accurately.

The common thresholds for all regions, which are the threshold values that all regions of the BabyMOSS reach for the scanned VCASB settings, are highlighted in the plots as the green area. For VBB = $0\,\mathrm{V}$, the thresholds of 24 to 33 DAC units can be reached throughout each region and for VBB = $-1.2\,\mathrm{V}$ the threshold range of 22 to 29 DAC units is common for all regions.

In chapter 7.4, the fitted data will be used to match every region to the same threshold. This is done by determining the specific VCASB value each region needs to be set to, in order to achieve the desired threshold throughout the whole sensor. Over the entire range common for all regions, the VCASB values corresponding to the fitted threshold values are retrieved.

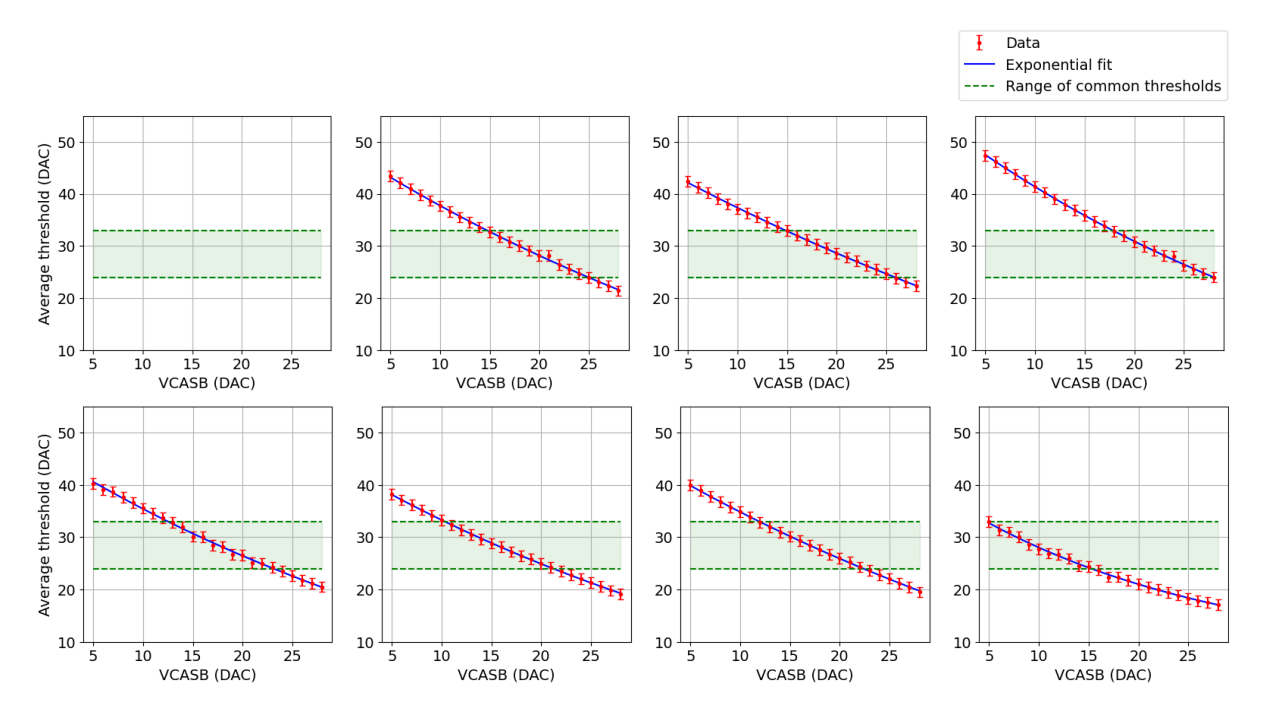


Figure 26: Average thresholds plotted against VCASB values for default DACs at VBB = 0 V. The panels depict the eight regions of the BabyMOSS.

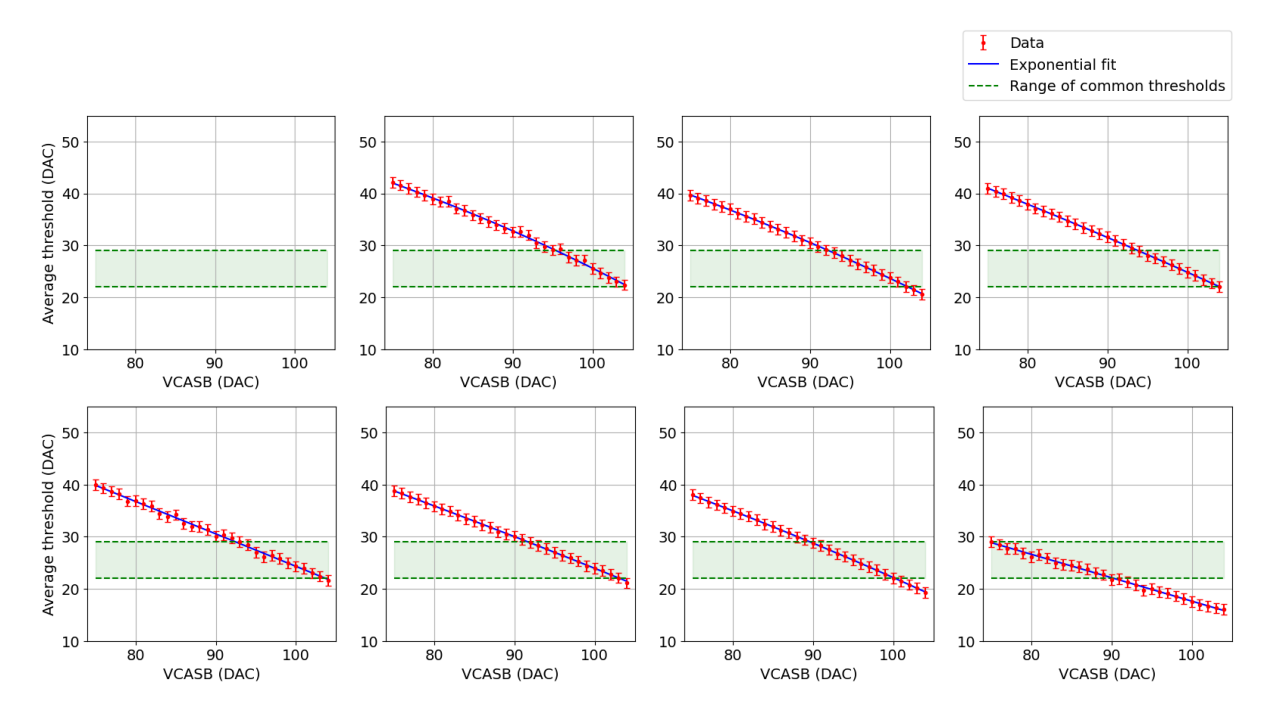


Figure 27: Average thresholds plotted against VCASB for default DACs at VBB = $-1.2\,\mathrm{V}$. The panels depict the eight regions of the BabyMOSS.

Region	$\chi^2_{\rm red}$ for VBB = 0 V	$\chi^2_{\rm red}$ for VBB = $-1.2\mathrm{V}$
Top 0	NaN	NaN
Top 1	0.05	0.11
Top 2	0.02	0.01
Top 3	0.03	0.01
Bottom 0	0.10	0.13
Bottom 1	0.01	0.02
Bottom 2	0.01	0.01
Bottom 3	0.06	0.06

Table 4: $\chi^2_{\rm red}$ values of the average threshold conducted with a scan of five rows.

6 Test Beam

In April 2024, there has been the opportunity to include the BabyMOSS in a test beam campaign at DESY (Deutsches Elektronen-Synchrotron) in Hamburg, Germany. The objective was to further examine the behavior of the BabyMOSS in response to varying operating points. For these operation points, different charge thresholds are used with and without applied reverse bias. In this chapter, the test beam facility is introduced and details of the test beam campaign are provided.

6.1 DESY II Test Beam Facility

The DESY test beam facility provides beam lines driven by the DESY II synchrotron, which has a circumference of 292.8 m and accelerates electrons. A bunch of about 10^{10} electrons is injected into the circular beam pipe after being accelerated to an energy of $E_{\rm min}=0.45\,{\rm GeV}$ by a linear preaccelerator called LINAC II. Inside DESY II, the particles get accelerated to a maximum energy of $E_{\rm max}=6.3\,{\rm GeV}$ and the beam is stored with sinusoidal beam energy ranging from $E_{\rm min}$ to $E_{\rm max}$. The bending magnets, driven by a sinusoidally oscillating current, follow 80 ms magnet cycles. After one DESY II cycle, which consists of two magnet cycles, the beam is dumped. Fig. 28 displays the oscillating DESY II beam energy, as well as the beam intensity. Because of the deceleration and the subsequent beam losses, a decrease in beam intensity can be observed for the second magnet cycle [26].

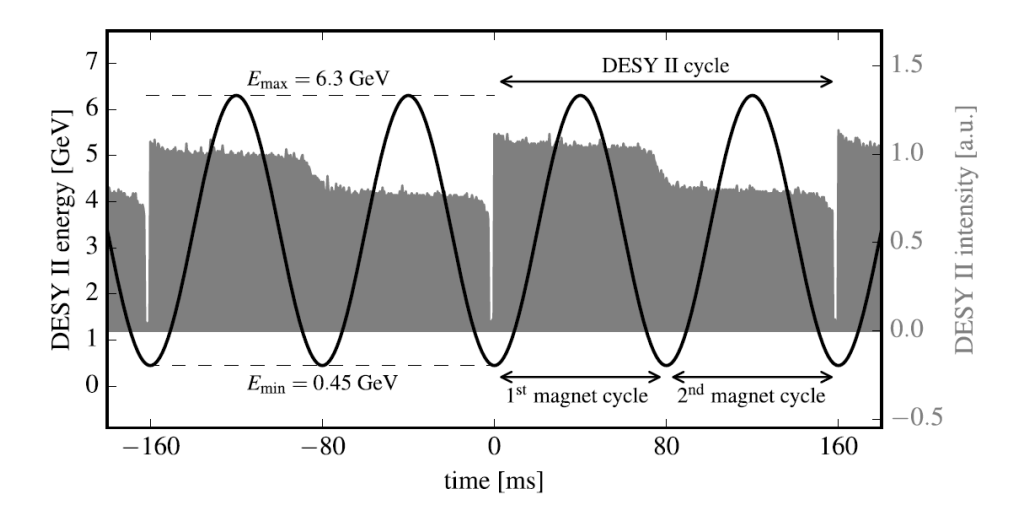


Figure 28: Schematic of the sinusoidal beam energy of DESY II (black) with the corresponding beam intensity (grey) in the background [26].

For the DESY II test beam facility, whose layout is sketched in Fig. 29, the primary beam is not directly extracted from DESY II. Instead, a primary target consisting of carbon

fiber is permanently placed in the orbit of DESY II and intercepts the beam, which leads to the creation of bremsstrahlung photons. These photons are generated by electrons with the respective energies of the DESY II cycle and travel through an extraction pipe and an aluminum exit window out of the DESY II vacuum. Next, the photons travel through air before reaching the conversion target, which leads to the creation of electrons and positrons through pair production. Afterward, the electrons and positrons enter a high vacuum beam line, where they reach a dipole magnet, which deflects the particle trajectories depending on the momentum and charge of the respective particle. The polarity and strength of the magnetic field of the dipole magnet can be adjusted and together with the help of a configurable primary collimator, a beam consisting of the desired particle type and momentum is transmitted further while all remaining particles are rejected. This beam passes through a beam shutter before reaching the test beam area, where the particle rate is monitored by a beam counter consisting of two scintillators and the beam is shaped by a fixed secondary lead collimator.

Due to the oscillating energy of the primary beam, the particle rate reduces when selecting higher test beam energies. When selecting lower energies, the higher particle rate leads to an increase of the amount of data being collected. However, lower energies also cause an increase in multiple scattering within the particle detectors (Eq. 8). The selected test beam energy is determined depending on the individual requirements of the test beam campaign.

In DESY II, three primary targets are implemented creating three independent beam lines, which are referred to as TB21, TB22 and TB24 [26].

The test beam, which is referenced in this study, was conducted at beam line T24.

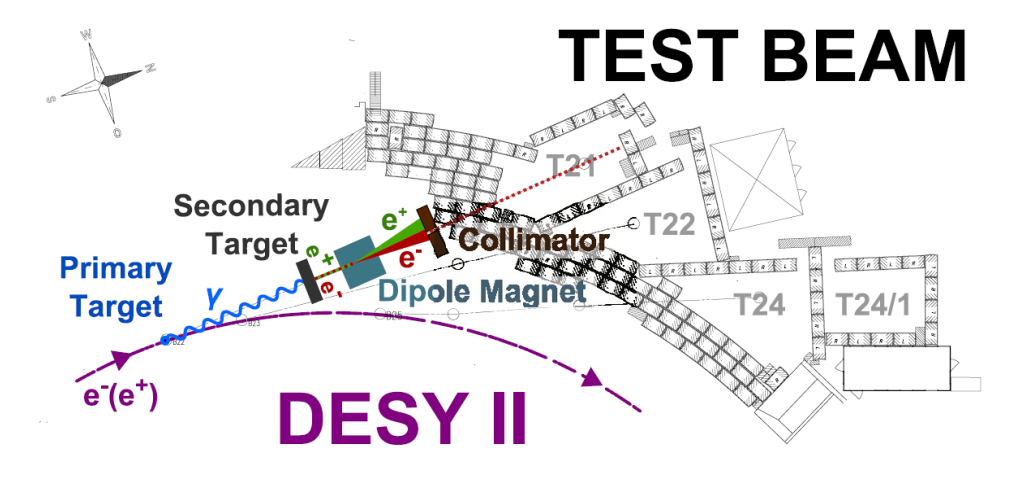


Figure 29: DESY II Test Beam Facility [26].

6.2 Test Beam Campaign

When running a test beam campaign, the device under test (DUT) is generally placed inside a structure called beam telescope. This beam telescope is comprised of multiple detectors with known properties positioned in front of and behind the DUT, providing spatial resolution and timing. The sensors of the telescope, typically consisting of six planes, provide reference data for the DUT, which enables the tracking of particle trajectories along the sensor planes.

However, the test beam campaign conducted at the DESY test beam facility in April 2024 targeted multiple research projects and therefore BabyMOSS did not represent the primary DUT. The primary DUT was placed inside a telescope consisting of six ALPIDE planes with a scintillator positioned in front of the telescope, that provides timing in the sense of an event start signal. Behind the telescope, a second scintillator was implemented before the additionally tested devices. The BabyMOSS is positioned behind the second scintillator and at the very end, three planes of Outer Barrel Modules (OBM) are placed. The complete setup is displayed in Fig. 30 and Fig. 31 shows a close up of the BabyMOSS, mounted on the carrier card and connected to a raiser board and DAQ board. The BabyMOSS sensor is connected as described in chapter 5.



Figure 30: Complete test beam setup at beam line T24 of the DESY test beam facility in April 2024.

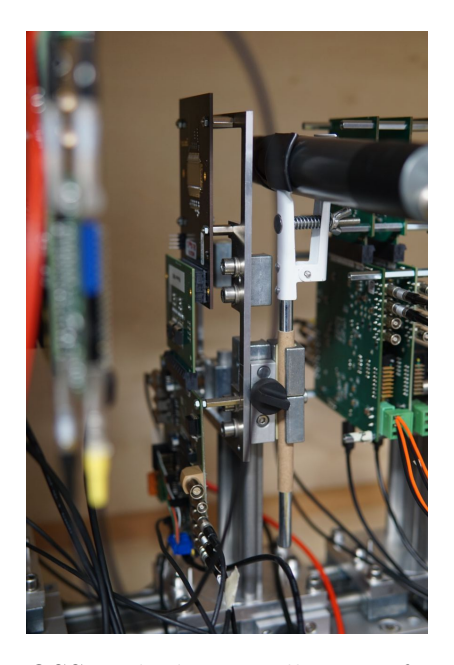


Figure 31: Close up of BabyMOSS with the scintillator in front at the test beam campaign in April 2024.

The implementation of scintillators enables limiting the readout and storage of the data collected by the pixel sensors to times when there is a high chance of a particle actually traversing the beam. The scintillators are of roughly the same size as the pixel detectors and placed in geometrical overlap before the sensor with respect to the beam. When the scintillator registers a particle hit, a trigger signal is distributed to all connected pixel sensors. In response to the trigger signal, the pixel sensor starts reading out the data. During this time, a busy signal is sent to the trigger board, which blocks following trigger signals from being distributed while the pixel sensors are occupied [27].

For the test beam setup described above, the first scintillator provides trigger signals in coincidence with the second scintillator for the telescope setup by daisy-chaining the DAQ boards in a master-slave configuration. Additionally, the second scintillator provides trigger signals for the BabyMOSS and the three OBM planes. The busy signal used to create trigger signals for the BabyMOSS and the OBM planes differs from the busy signal used for the telescope due to the longer readout time of the OBM planes. Since the priority of the test beam campaign was to investigate the DUT with the aim of taking as much data as possible, the choice was made to use separate trigger signals as opposed to synchronized ones.

Furthermore, no global clock could be employed to assign timestamps to the individual events. Only the timestamps supplied by the clock of the data-taking computer are assigned to each event. Potentially non-synchronized and granularity lacking timestamps complicate the retroactive synchronization of the events detected by the telescope to the ones detected by the BabyMOSS, which is why the cluster size analysis in chapter 7 is

conducted using BabyMOSS as a standalone system.

The data acquisition software framework called EUDAQ2 is utilized for this test beam [28]. This framework facilitates the configuration and control of the data acquisition, as well as the collection of data produced by the detectors and its storage in a raw data file.

7 Test Beam Data Analysis

After the test beam campaign with the BabyMOSS, the stored data is analyzed using the test beam data reconstruction framework Corryvreckan [29]. The Corryvreckan framework, which is written in modern C++, possesses a modular event reconstruction chain. This property is what leads to the versatility of the framework. When analyzing data with Corryvreckan, the raw data from the EUDAQ2 files first is decoded and processed by EventLoader modules. Events are constructed from the data by using the trigger identification number (ID) to assign detected hits to a Corryvreckan event. A hit is detected by a pixel, when a signal voltage exceeds the user-defined discriminator threshold, as described in chapter 5.1.

In order to accurately examine the detector characteristics using the test beam data, signals from pixels that exhibit an exceptionally high fake-hit rate are unwanted and should therefore be excluded from the further data analysis. The Corryvreckan module MaskCreator provides a method to mask such pixels, based on the comparison of the individual hit rates of the pixels to the global hit rate of the pixel matrix. Since the BabyMOSS consists of multiple pixel matrices of varying behavior, which are treated as independent sensors, the application of the MaskCreator module poses difficulties and a different approach for the pixel masking is explored in chapter 7.1.

Using the masked data, the cluster sizes of the sensor are analyzed in chapter 7.2. A cluster is produced when an impinging particle causes multiple pixels to register a hit, which then build the cluster. The total number of the pixels detecting a hit associated to the same particle define the cluster size. This occurs due to a process referred to as charge sharing, where the diffusion of the generated charge leads to fractions of the charge being collected in neighboring pixels. Corryvreckan provides a module called *Clustering4D*, which uses positional information to detect clusters and calculates the position of a cluster as the mean value of the pixel coordinates [29, 30].

Besides examining the cluster size distribution for the BabyMOSS with and without reverse bias, the development of the mean cluster size is analyzed in chapter 7.3 for an increasing VCASB value, which steers the threshold of the pixels.

However, the regions of the BabyMOSS exhibit different thresholds for the same VCASB setting as a result of the variations of the analog in-pixel front-end electronics. This is why the threshold scans of chapter 5 are utilized to match the different regions of the BabyMOSS to the same thresholds in chapter 7.4. This enables the comparison between different regions at similar operating points.

The test beam data analysis is performed on two different datasets, which were taken with and without reverse bias. Without reverse bias applied, 20 runs with 100 k events per run have been recorded for each VCASB setting during a test beam run using a 2.4 GeV/c

particle beam. In contrast, the data taken with VBB = $-1.2\,\mathrm{V}$ was recorded during a test beam run using a $4.8\,\mathrm{GeV/c}$ particle beam and only 10 runs have been recorded with 100 k events per run and per VCASB setting. The average energy loss per path length by ionization for the highly relativistic $2.4\,\mathrm{GeV/c}$ and $4.8\,\mathrm{GeV/c}$ electrons is approximately the same due to the high Lorentz gamma factor of the electrons in this regime.

Region top 0 is malfunctioning and not examined in this study, as discussed in chapter 4.2.

7.1 Pixel Masking and Analysis of Hit Count Distributions

As previously mentioned in chapter 5, pixel sensors potentially exhibit a number of pixels with an exceptionally high hit rate compared to the average pixel of the matrix. Such behavior can origin for example from a lower in-pixel threshold due to defects arising during the manufacturing process or subsequent damage. A fake-hit can then be initiated without external stimulation, but through thermal noise. Consequently, pixels with a relatively high fake-hit rate have the potential to bias the sensor characterization. This is why such pixels need to be masked, which effectively excludes them from the further data analysis.

The Corryvreckan framework provides a *MaskCreator* module, which can be used to mask unwanted pixels that demonstrate atypically high hit rates. Within this module, the frequency method can be used to mask pixels based on comparison of their individual firing rate to the global pixel firing rate, which is calculated over one reference run. For the BabyMOSS, each region is treated as an independent sensor and the global firing rate is calculated for each region individually. A pixel is designated as noisy, when its hit rate exceeds the global hit rate multiplied by the so-called *frequency cut*. The frequency cut value is chosen by the user depending on the individual prerequisites and requirements. All pixels that are identified as noisy are written to a mask file and excluded in subsequent Corryvreckan analysis procedures [29, 30].

To review the results from this masking procedure, generated hitmaps can be used, which display the recorded hits of the analyzed dataset in a 2D histogram. When applying this masking method to the BabyMOSS data taken at the DESY test beam campaign, one reference run was used to generate the mask file, which was then applied for all 20 runs per VCASB setting taken without reverse bias or 10 runs per VCASB setting with reverse bias. When reviewing the hitmaps, it became apparent, that using one reference run to create the masking for all runs does not consistently capture all pixels with atypically high hit rates. It was observed, that certain runs still resulted in hitmaps exhibiting single pixels with extremely high hit rates. Consequently, a method of masking using the entire

dataset of one setting would ensure a more reliable masking.

Moreover, it became apparent, that choosing one frequency cut value, which is applied to all eight regions of the sensor, results in drastically different hitmaps for each region regarding the maximum hit count and the number of pixels that can be observed to exhibit high hit counts. Every region of the sensor shows varying behavior due to differences in the in-pixel front-end electronics, as described in chapter 4.3, which includes varying thresholds for the same DAC settings, as discussed in chapter 5.1. When one region has more pixels with a very high hit rate, the global hit rate of this region increases. This in turn raises the maximum firing rate a pixel is allowed to exhibit, before it is masked. As a result, the critical hit rate used for the masking of pixels varies between the regions and cannot be individually adapted to each region, since the frequency cut value is set uniformly for the BabyMOSS, while the global hit rate of the regions differs.

Ultimately, the *MaskCreator* module is a simplistic method to mask noisy pixels and relies on a quiet sensor. To utilize the entire dataset of each setting for pixel masking and gain a better understanding of the individual behavior of the regions regarding hit rates, which allows for a more educated masking process, another method is applied.

For this other method, a python code is written to define the masking specifically for the BabyMOSS. The data processing is explained using exemplary settings based on given standards for the VCASB value, which were introduced in chapter 5: VCASB = $15 \,\mathrm{DAC}$ units for VBB = $0 \,\mathrm{V}$ and VCASB = $84 \,\mathrm{DAC}$ units for VBB = $-1.2 \,\mathrm{V}$.

7.1.1 Exemplary Analysis without Reverse Bias

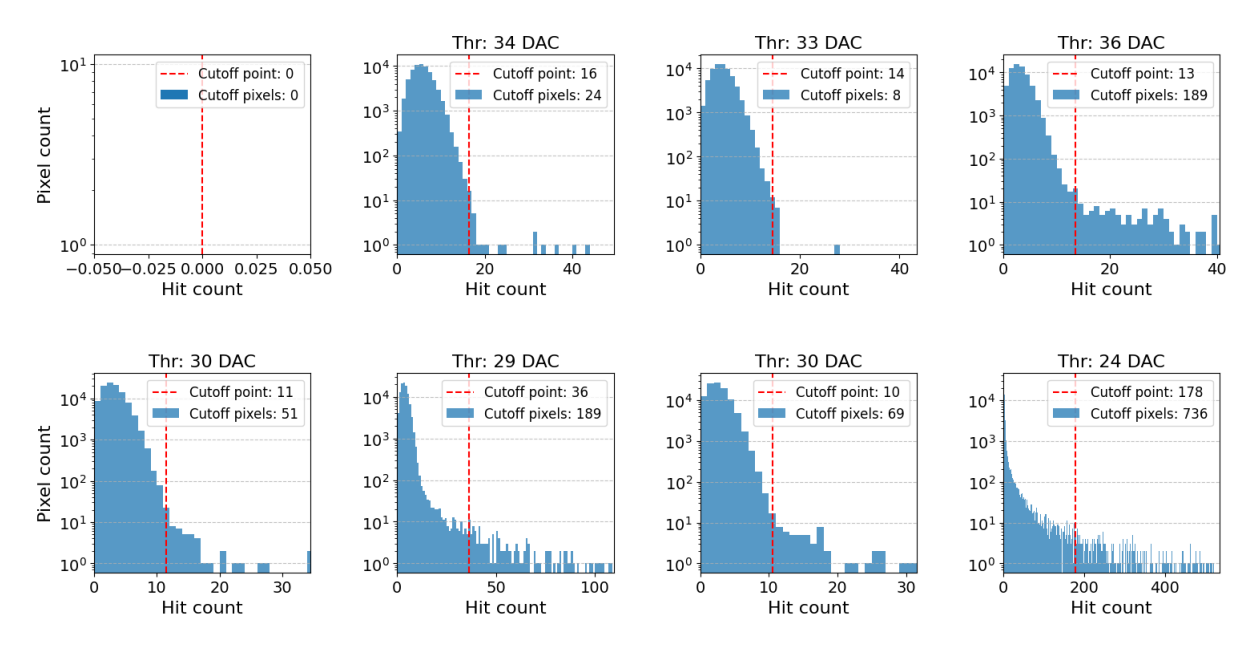


Figure 32: Distribution of the number of pixels per hit count in two million events for $VCASB = 15 \, DAC$ units at $VBB = 0 \, V$. The bin width equals one hit count. All pixels above the cutoff point are masked. The panels depict the eight regions of the BabyMOSS.

Region	Cutoff hit rate (pixel $^{-1}$ event $^{-1}$)
Top 0	-
Top 1	$8 \cdot 10^{-6}$
Top 2	$7 \cdot 10^{-6}$
Top 3	$6.5 \cdot 10^{-6}$
Bottom 0	$5.5 \cdot 10^{-6}$
Bottom 1	$18 \cdot 10^{-6}$
Bottom 2	$5 \cdot 10^{-6}$
Bottom 3	$89 \cdot 10^{-6}$

Table 5: Critical hit rate used to identify noisy pixels for each region of the BabyMOSS at VBB = 0 V and VCASB = 15 DAC units.

Firstly, the raw test beam data of two million events is read with Corryvreckan. In order to better understand the behavior of the BabyMOSS and to determine the pixels that need to be masked, the number of pixels is plotted against the hit count in two million events (Fig. 32). Each pixel of the sensor records a specific number of hits in two million events. The plot displays the total number of pixels corresponding to a specific hit count. The sum of all pixel counts in one region results in the total number of pixels in the matrix. In an effort to improve the visibility of the most important parts of the distribution, the x-axis does not show the complete range of hit counts present for each region, but only the lower section. The order of magnitude of the total hit count range for each region can

be extracted from the hitmaps in Fig. 33. The threshold, which is given in DAC units, is displayed above each region. The threshold values for each region were determined with the laboratory scans described in chapter 5. The thresholds are again displayed in all following plots of chapter 7.1.1.

The distributions of the pixels per hit count for the different regions of the sensor display varying behavior. Region top 1 and 2 exhibit a rise in pixel counts before a decline, with the peak of pixel counts representing the most probable hit count value for a given pixel in the matrix, which is referred to as the mode. The distribution around the mode is a consequence of the random impingement of particles on the sensor. After the decline, pixels with further increasing hit counts only appear sporadically. The other regions also display this peak in pixel counts, but the decline of the distribution transitions into a tail of pixels with higher hit counts. These regions exhibit a larger fraction of pixels with hit counts much higher than the mode.

Since some regions exhibit this tail in the distribution, classifying pixels as noisy becomes more complex compared to cases where pixels show only sporadically exceptionally high hit counts, indicative of defective pixels. These outlier pixels of high hit counts can then be separated more distinctly and associated to a high fake-hit rate. For the masking, a cutoff point of the hit count is set for each region and all pixels that exhibit a higher hit count are classified as noisy and masked. The cutoff point is chosen to be at the highest hit count exhibited by 10 pixels. After this cutoff point, each hit count corresponds to fewer than 10 pixels. This results in the masking of the occasionally appearing pixels of high hit counts for region top 1 and 2, as well as the cutoff of a large fraction of the tail of pixels with increasing hit counts, which can be associated with fake hits. In Fig. 32, this cutoff point is illustrated through the vertical red line and all pixels that are located on the right side of this line are masked by extracting their coordinates and writing them into a mask file. The resulting critical hit rates from the cutoff hit count are calculated for each region by division with the total number of events and displayed in Tab. 5. The number of masked pixels per region is also displayed in Fig. 32 and ranges from 8 to 736, which demonstrates the varying behavior of the regions. In all cases, the proportion of masked pixels stays below 0.01 % of the total number of pixels, indicating that the data is not majorly biased through this masking process.

The region with the most masked pixels and the largest tail is region bottom 3, while this is also the region with the lowest threshold given a common VCASB setting for all regions. This indicates that the observed tail in the distribution, corresponding to pixels exhibiting exceptionally high hit rates, is due to the relatively high sensitivity of the pixels. For the higher thresholds the other regions exhibit, the tail of the distribution generally decreases in comparison.

In contrast, region top 3, which is assigned the highest threshold, shows a relatively large

tail, indicating differences in behavior compared to the other regions due to differences in the in-pixel front-end electronics. However, this behavior could also be influenced by differences between the threshold, that was measured by doing laboratory scans, and the actual threshold of the region during the data taking at the test beam.

For one, the different environmental conditions can influence the threshold of the sensor. While this would apply to all regions of the sensor, a varying reaction to the changes in environmental conditions due to the varying in-pixel front-end electronics cannot be ruled out. Different front-end designs can respond differently to e.g. the same temperature variation. Following the test beam campaign, the threshold of the MOSS, and consequently the BabyMOSS, has been demonstrated to be sensitive to temperature. The dependency between threshold and temperature can be estimated to about 0.3 DAC per 1 °C [31]. This is why more recent versions of the raiser board have the possibility to measure the room temperature, while the one used in this study was of a previous version and did not have this capability.

Additionally, a bandgap reference voltage and current is used by the DACs to convert digital signals into analog ones. A reference voltage is important for most integrated circuits as it enables reliable and predictable performances. A bandgap reference circuit operates by combining a voltage that decreases linearly with temperature with another that increases linearly with temperature. This results in a reference voltage that is first-order independent of temperature with a value close to the bandgap voltage of silicon [32]. Bandgap trimming is used to modify this reference voltage by means of a complex network of resistors and digital decoder, as well as a direct adjustment of the bandgap outputs. For the MOSS and BabyMOSS, the bandgap circuitry provides a reference voltage which should be trimmed to about 416 mV and a reference current of 10.2 µA [20]. Variations in the bandgap trimming can lead to variations in the reference voltage and current, which influence the analog signals produced by the DACs and thus change the discriminator thresholds of the sensor. No data regarding the exact bandgap trimming was documented during the test beam, which was conducted using preliminary software, which raises the possibility that a discrepancy exists between the bandgap trimming for the test beam and for the laboratory scans.

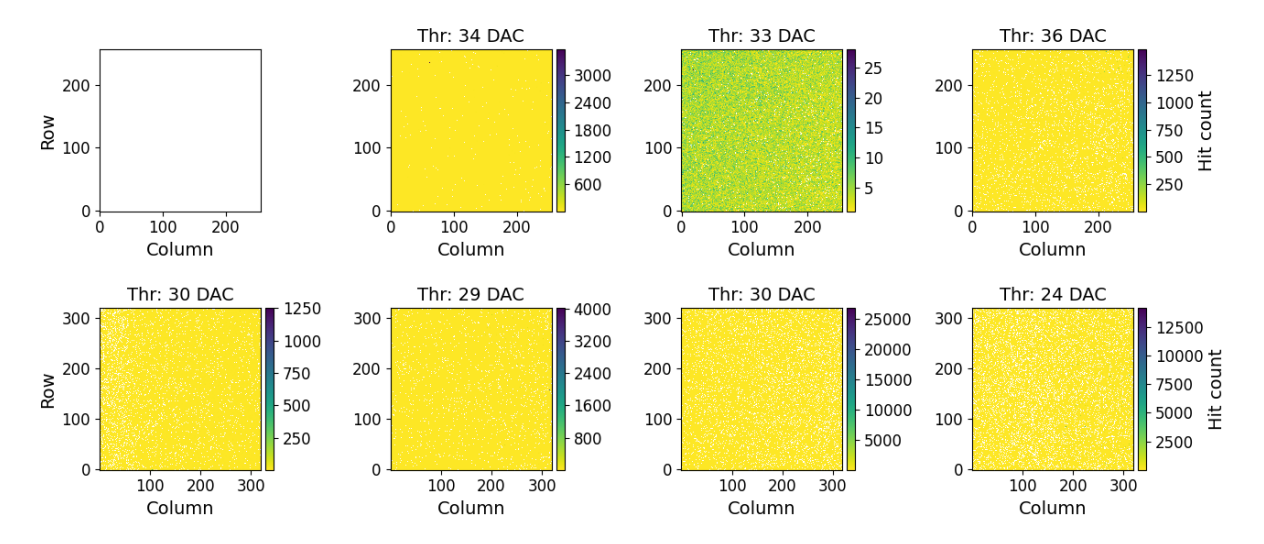


Figure 33: Hitmaps for VCASB = $15 \, \text{DAC}$ units at VBB = $0 \, \text{V}$ before masking. The data taken for two million events is analyzed and the panels depict the eight regions of the BabyMOSS.

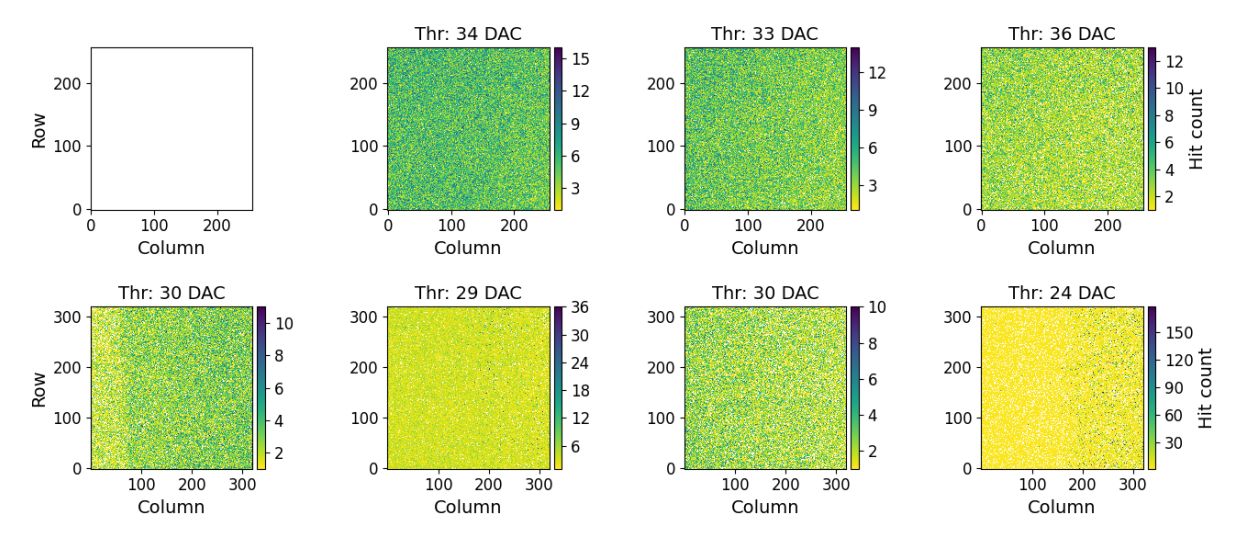


Figure 34: Hitmaps for VCASB = $15 \,\mathrm{DAC}$ units at VBB = $0 \,\mathrm{V}$ after masking. The data taken for two million events is analyzed and the panels depict the eight regions of the BabyMOSS.

The effect the applied masking has on the order of magnitude of the maximum hit count of each region for the analyzed dataset can be observed in Fig. 33 and Fig. 34. The Figures display the recorded hits for two million events in a 2D histogram before and after the masking was applied. The 2D grids of these hitmaps represent the pixel matrices, where every pixel is assigned a color according to their recorded hit count.

Before the masking, the hit count ranges of the different regions span several orders of magnitude. Region top 2 displays a maximum hit count in the order of 10^1 hits per pixel, forming the lower limit of hit count ranges across the regions. Region bottom 3 shows a maximum hit count in the order of 10^4 hits per pixel, which creates the upper limit

of hit count ranges. After the masking was applied, which excludes the pixels with the highest hit counts from the data as previously discussed, most regions display maximum hit counts in the order of 10^1 hits per pixel. Only region bottom 3 shows a maximum hit count in the order of 10^2 hits per pixel, which is higher compared to the other regions, but to be expected considering the low threshold and therefore high fake-hit rate for this region at this setting, which cannot be entirely accounted for by the masking process without risking to bias the data. However, some unexpected behavior can be observed for region bottom 0 and bottom 3, as both display a not perfectly uniform distribution of detected hits.

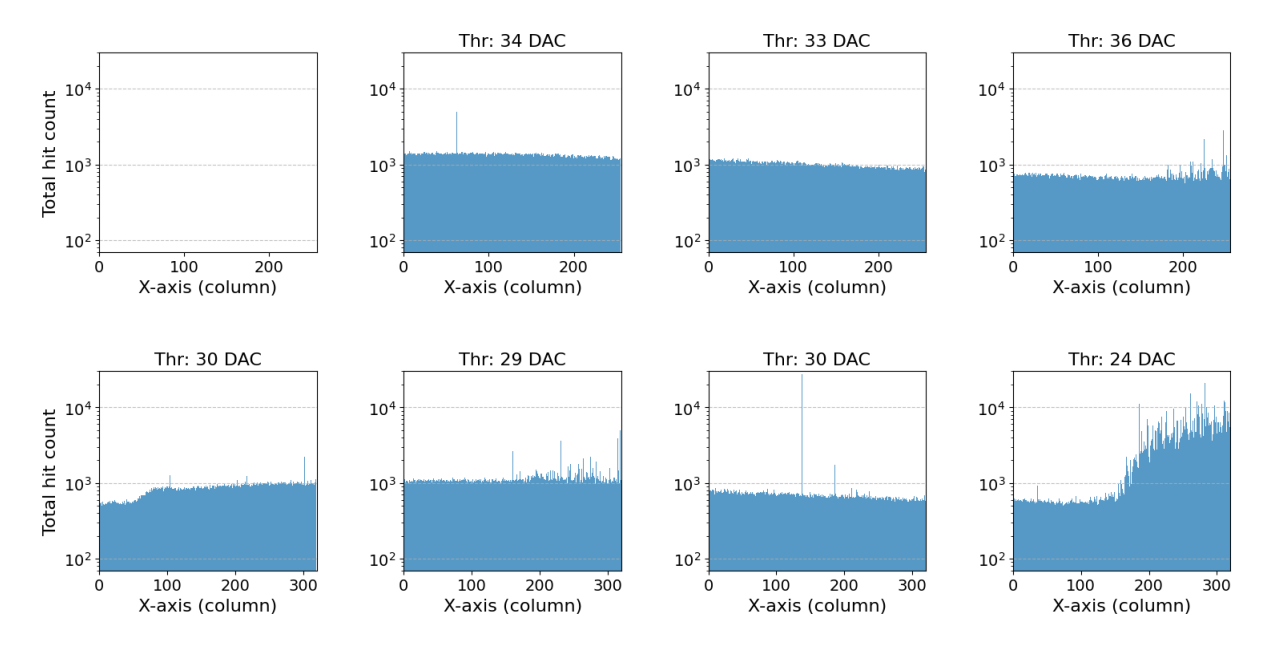


Figure 35: Hit count projected onto the x-axis for $VCASB = 15\,DAC$ units at $VBB = 0\,V$ before masking. The data taken for two million events is analyzed and the panels depict the eight regions of the BabyMOSS.

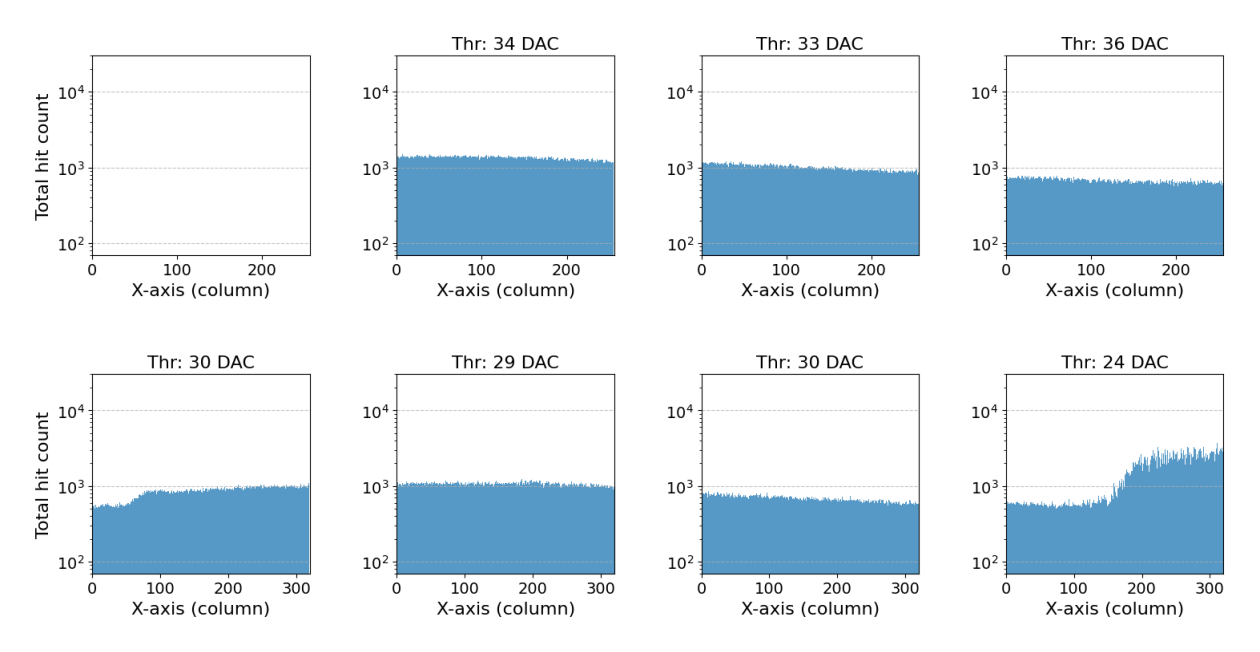


Figure 36: Hit count projected onto the x-axis for VCASB = $15 \,\mathrm{DAC}$ units at VBB = $0 \,\mathrm{V}$ after masking. The data taken for two million events is analyzed and the panels depict the eight regions of the BabyMOSS.

In order to get a better understanding on the distribution of the recorded hits, Fig. 35 and Fig. 36 display the hit counts projected onto the x-axis before and after the masking. Here, the hit counts of all the pixels in each column are summed up and plotted in a logarithmic scale. When comparing the distributions before and after the masking, the spikes of especially high hit counts disappear and the distribution becomes more flat, as expected. It is clearly visible both with and without masking that region bottom 0 detects less hits over a narrow stripe of pixels on the far left side. For every dataset taken with varying VCASB settings, the stripe of pixels detecting less hits in region bottom 0 appears. It can be assumed that this stripe appears due to this area being covered by something placed before the BabyMOSS in the test beam set up. This coverage may be related to the scintillator mount, which was placed directly in front of the BabyMOSS as can be observed in Fig. 30.

Far more unusual is the drastic change in hit counts from the left side to the right side in region bottom 3. The number of detected hits rises steeply at the midpoint of the region and then stabilizes at a hit count that is approximately one magnitude higher than that of the left side of the sensor. It seems, that the pixels on the right side of the matrix have a lower effective threshold compared to the pixels on the left side of the matrix, which increases the probability to detect fake hits induced by noise. The behavior of exhibiting a left-to-right asymmetry regarding the fake-hit rate was already observed by Styliani Paniskaki [33] [34] and is not specific for one region, but dependent on the threshold of the region.

Besides BabyMOSS, MOSS has also shown a left-to-right asymmetry regarding the fake-hit

rate. Preliminary results of separate studies suggest that the observed effects are related to the choice of strobe signal length and its distribution across the matrix [35]. This correlation was observed after the test beam campaign of this study was conducted and is under current investigation.

For the dataset of VCASB = 15 DAC units, the left-to-right asymmetry only occurs for region bottom 3 due to the low threshold this region has for the set DACs. When increasing the VCASB value and therefore decreasing the discriminator threshold of the pixels, the left-to-right asymmetry can be observed also for other regions of the Baby-MOSS. As an example, the hit count projection for the highest VCASB value analyzed of the test beam for all regions without reverse bias can be found in the appendix (Fig. 54).

7.1.2 Exemplary Analysis with Reverse Bias

When a reverse bias of VBB = $-1.2 \,\mathrm{V}$ is applied between the collection diode and the substrate of the pixels, the pixels become fully depleted. When a particle traverses a pixel, the generated electron-hole pairs are quickly separated by the electric field in the depletion region, preventing recombination and reducing charge loss. Due to the larger drift region for applied reverse bias, the charge collection time is reduced. Moreover, the larger depletion region results in a reduced junction capacitance, which allows for a larger voltage signal to be detected from same amount of collected charge, as explained in chapter 3.5. This, in turn, leads to an improved signal-to-noise ratio [2, 16].

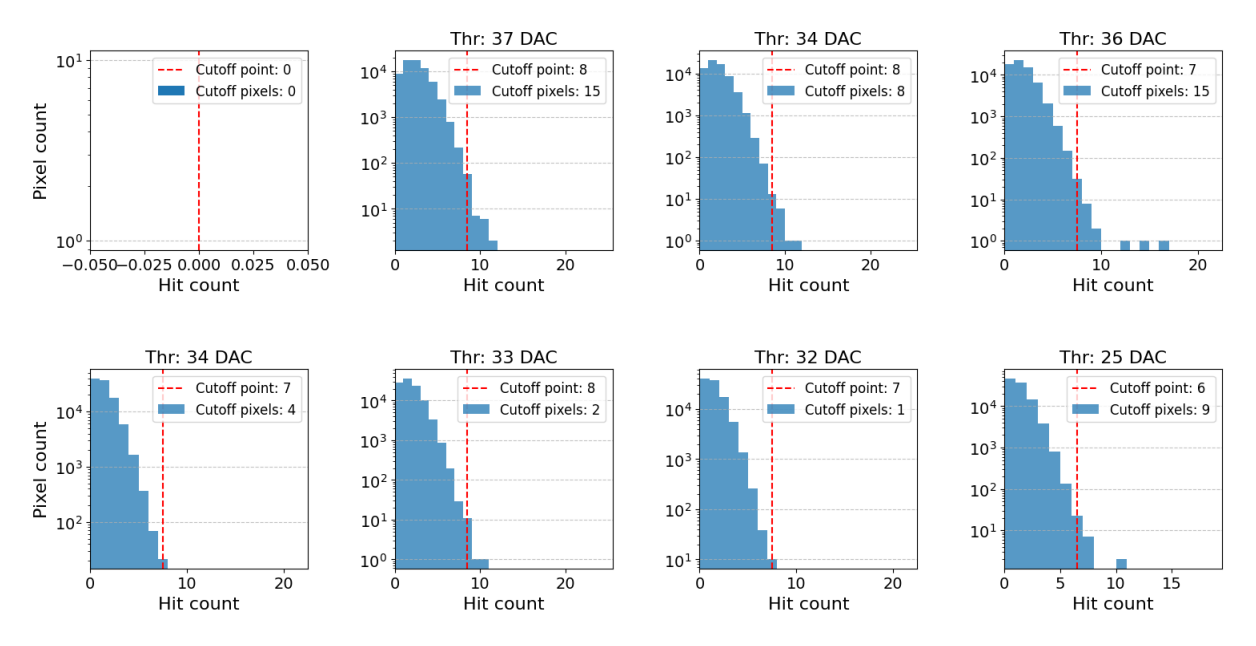


Figure 37: Distribution of the number of pixels per hit count in one million events for VCASB = $84 \,\mathrm{DAC}$ units at VBB = $-1.2 \,\mathrm{V}$. The bin width equals one hit count. All pixels above the cutoff point are masked. The panels depict the eight regions of the BabyMOSS.

Region	Cutoff hit rate ($pixel^{-1}event^{-1}$)
Top 0	-
Top 1	$8 \cdot 10^{-6}$
Top 2	$8 \cdot 10^{-6}$
Top 3	$7 \cdot 10^{-6}$
Bottom 0	$7 \cdot 10^{-6}$
Bottom 1	$8 \cdot 10^{-6}$
Bottom 2	$7 \cdot 10^{-6}$
Bottom 3	$6 \cdot 10^{-6}$

Table 6: Critical hit rate used to identify noisy pixels for each region of the BabyMOSS at VBB = -1.2 V and VCASB = 84 DAC units.

The dataset analyzed in this section was recorded with an applied reverse bias and adjusted VCASB value, as discussed in chapter 5.2. The data is processed in the same manner as the dataset taken without reverse bias. The one million events are first read with Corryvreckan. Fig. 37 displays the number of pixels per hit count in one million events for the BabyMOSS with VCASB = $84\,\mathrm{DAC}$ units at VBB = $-1.2\,\mathrm{V}$. The threshold, given in DAC units, is again displayed above each region for this and all following plots of chapter 7.1.2. In contrast to the results without reverse bias, the distributions display no tail corresponding to pixels with exceptionally high hit counts compared to the mode, even though the pixel thresholds are in a similar range. The cutoff point, represented by the vertical red line in Fig. 37, is again set to be at the highest hit count exhibited by 10 pixels. The resulting critical hit rates from the cutoff hit count are displayed in Tab. 6. Pixels exhibiting higher hit counts are written to the mask file and excluded from the further data analysis. In comparison to the case without reverse bias, the number of masked pixels is generally smaller and ranges from 1 to 15, staying below 0.001% of the total number of pixels for all regions.

The absence of tails in the distributions of pixel counts over the hit count, which correlates with the lower number of masked pixels, can be attributed to an overall lower amount of fake hits being recorded compared to the case without applied reverse bias due to the improved signal-to-noise ratio.

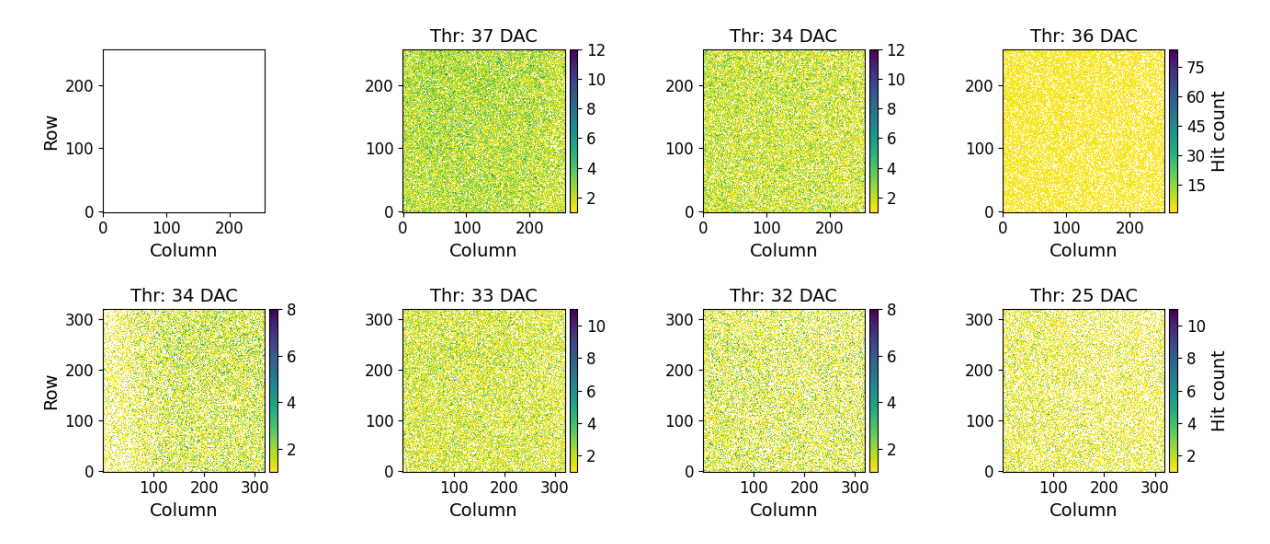


Figure 38: Hitmaps for VCASB = $84\,\mathrm{DAC}$ units at VBB = $-1.2\,\mathrm{V}$ before masking. The data taken for one million events is analyzed and the panels depict the eight regions of the BabyMOSS.

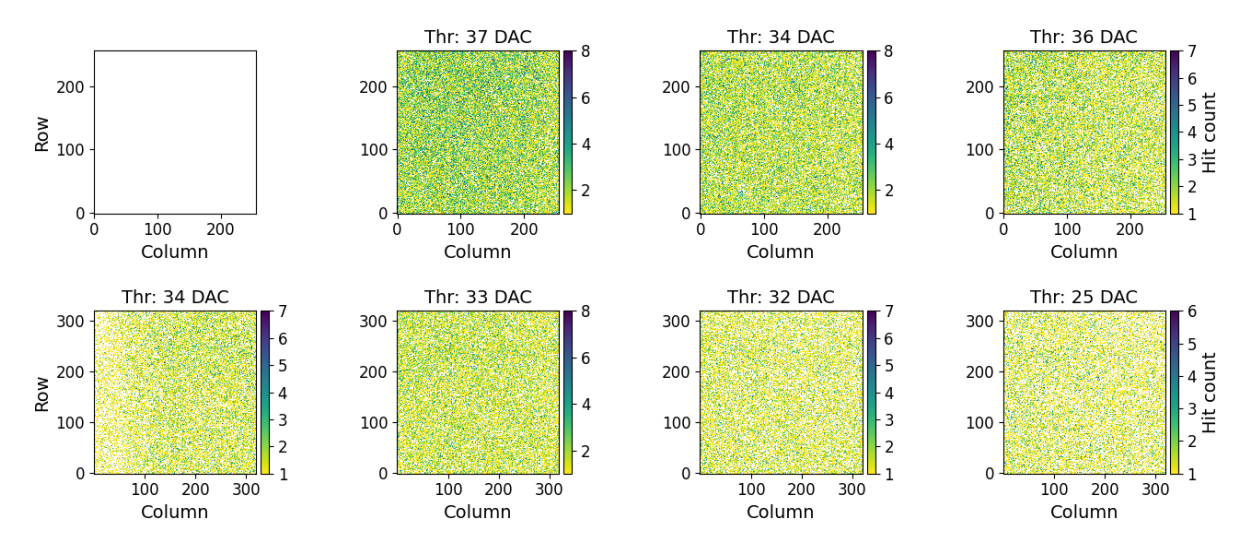


Figure 39: Hitmaps for VCASB = $84\,\mathrm{DAC}$ units at VBB = $-1.2\,\mathrm{V}$ after masking. The data taken for one million events is analyzed and the panels depict the eight regions of the BabyMOSS.

The hitmaps of data taken for one million events prior to the masking are displayed in Fig. 38 and after the masking in Fig. 39.

Once again, a stripe with decreased hit rate on the left side can be observed for region bottom 0, supporting the previous conclusion that this appears due to this area being covered by something placed in front of the sensor. However, no left-to-right asymmetry can be observed, even for region bottom 3, which again exhibits the lowest threshold.

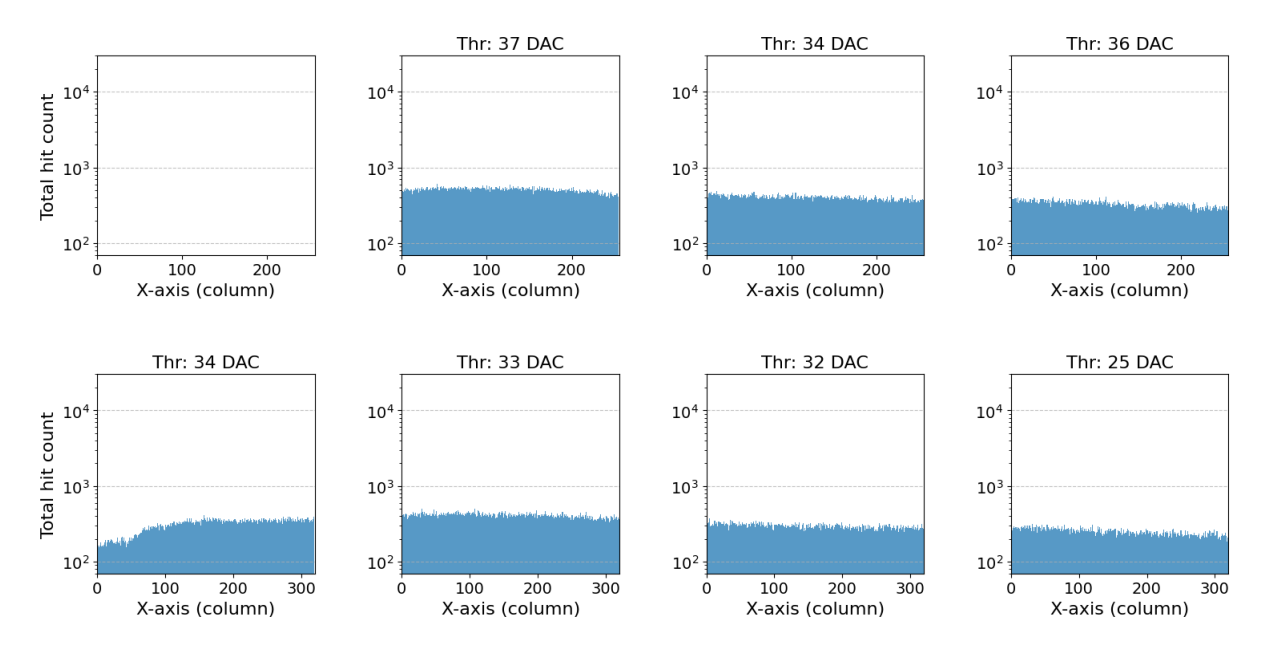


Figure 40: Hit count projected onto the x-axis for VCASB = $84\,\mathrm{DAC}$ units at VBB = $-1.2\,\mathrm{V}$ before masking. The data taken for one million events is analyzed and the panels depict the eight regions of the BabyMOSS.

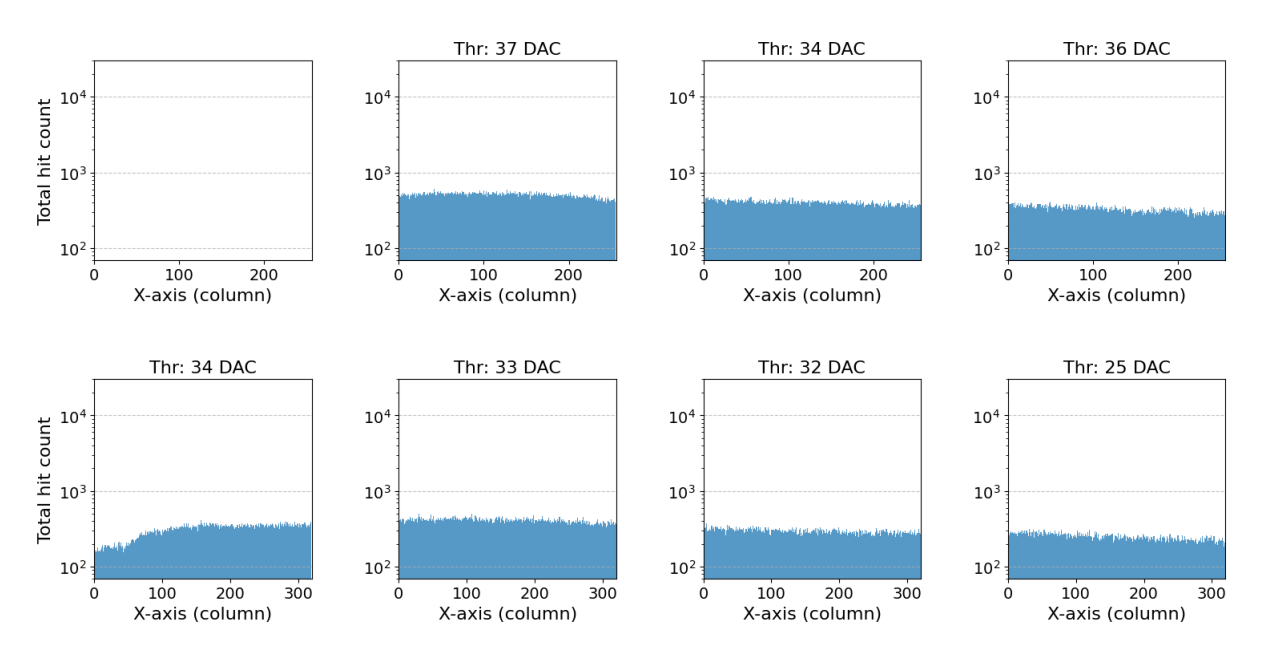


Figure 41: Hit count projected onto the x-axis for VCASB = $84\,\mathrm{DAC}$ units at VBB = $-1.2\,\mathrm{V}$ after masking. The data taken for one million events is analyzed and the panels depict the eight regions of the BabyMOSS.

Fig. 40 and Fig. 41 display the hit count projection onto the x-axis for one million events before and after masking. Due to the improved signal-to-noise ratio for applied reverse bias, no distinct spikes in hit counts are visible even before the masking of noisy pixels. As in Fig. 36, a stripe of decreased hit rate can be observed in bottom 0, but no left-to-right asymmetry in hit counts can be observed. Indeed, no left-to-right asymmetry in hit counts as seen with reverse bias can be observed even for higher VCASB settings and therefore

lower thresholds. As an example, the hit count projection onto the x-axis for the highest VCASB analyzed of the test beam for all regions can be found in the appendix (Fig. 55), which shows no left-to-right asymmetry with a steep rise at the midpoint of the pixel matrix. The left-to-right asymmetry of the fake-hit rate appears to only visibly influence the hit count distribution over the pixel matrices when when no reverse bias is applied. This can be attributed to the improved signal-to-noise ratio for applied reverse bias, which occurs due to the reduced junction capacitance of the expanded depletion region.

7.2 Cluster Size Distributions

The expected spatial resolution of a sensor in the absence of charge sharing between pixels is referred to as binary resolution, where the impact position of a particle is assumed to be at the center of the pixel that detects the hit. It is calculated as follows [1]:

$$\sigma_{\text{binary}} = \frac{\text{pixel pitch}}{\sqrt{12}} \tag{26}$$

The top unit of BabyMOSS has pixels with a pitch of $22.5 \,\mu\text{m}$, which results in a binary resolution of $6.5 \,\mu\text{m}$. For the bottom unit, which has a pixel pitch of $18 \,\mu\text{m}$, the binary resolution is at $5.2 \,\mu\text{m}$.

The spatial resolution can be further improved, when charge sharing between pixels is present, causing clusters to be formed. When a cluster of pixels is associated with one hit, the impact position can be determined by calculating the center of gravity of the cluster, leading to a sub-pixel position estimation of the impinging particle. Therefore, studying clusters in BabyMOSS is of particular interest.

The previously masked data of the test beam is used to analyze the cluster size distributions of the sensor with and without reverse bias for the given standard VCASB settings.

When a particle traverses a pixel sensor and deposits charge, as described in chapter 3.5, electrons and holes are produced. When the charge is generated in an undepleted region of the pixel, diffusion is the dominating process. After entering the depletion region of the pixel, drift dominates and charge drifts towards the collection diode. Since the pixels in the pixel matrix of the sensor are not isolated from each other, the charge can be shared between multiple pixels due to diffusion or capacitive coupling during the drift process. As a result, multiple pixels are able to detect a signal from the same particle and form a cluster. The cluster size refers to the number of pixels participating in such a cluster. Corryvreckan provides a module called *Clustering4D*, which uses positional information to detect clusters.

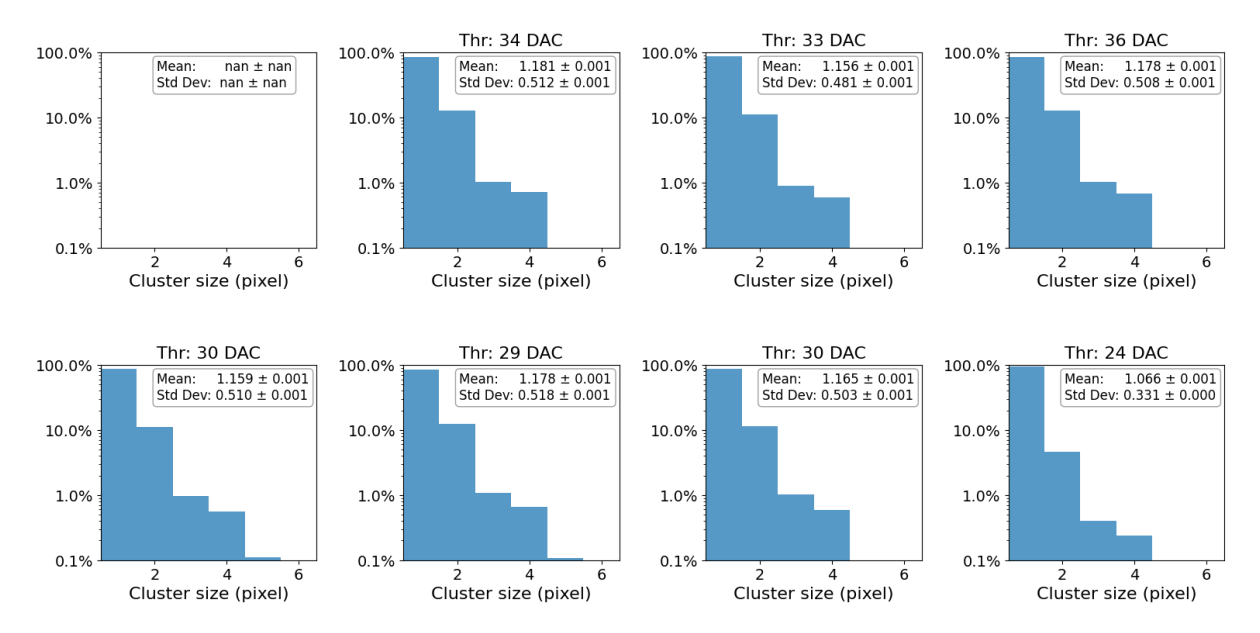


Figure 42: Cluster size distribution for $VCASB = 15 \, DAC \, units$ at $VBB = 0 \, V$ after masking. The data taken for two million events is analyzed and the panels depict the eight regions of the BabyMOSS.

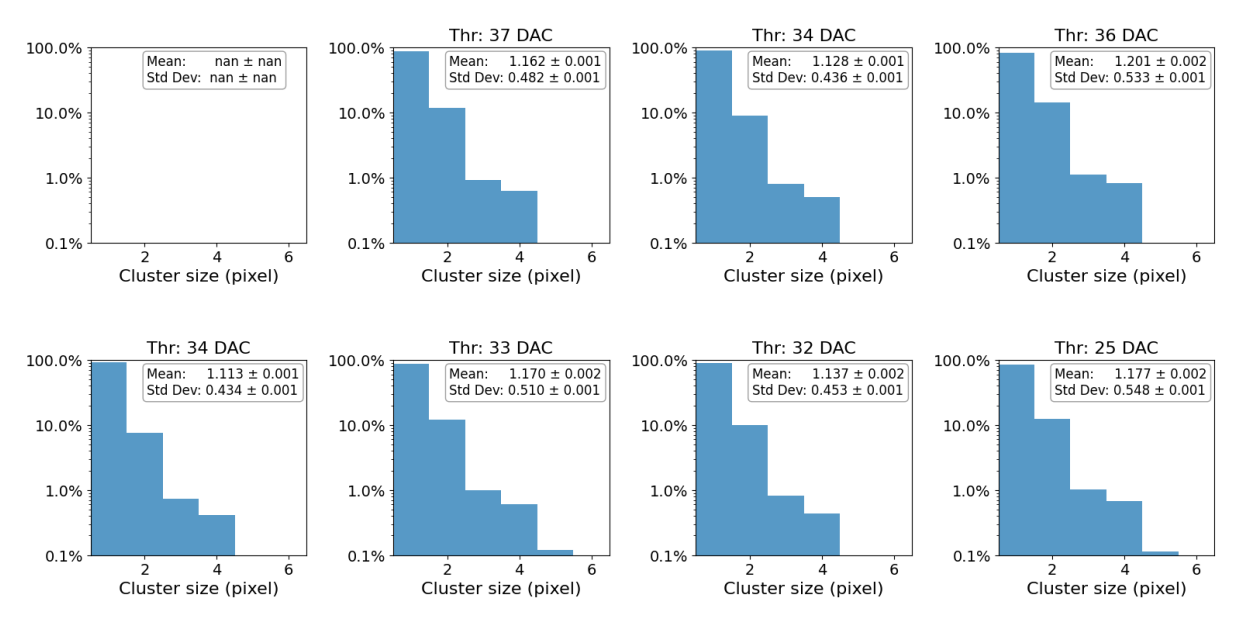


Figure 43: Cluster size distribution for VCASB = $84\,\mathrm{DAC}$ units at VBB = $-1.2\,\mathrm{V}$ after masking. The data taken for one million events is analyzed and the panels depict the eight regions of the BabyMOSS.

Fig. 42 displays the cluster size distribution of data taken in two million events for VCASB = 15 DAC units and VBB = 0 V. Fig. 43 displays the cluster size distribution of data taken in one million events for VCASB = 84 DAC units and VBB = -1.2 V. The mean and standard deviation are calculated using Eq. 21 and 22 with n as the total

number of clusters. The uncertainty of the mean is calculated as follows:

$$\sigma_{mean} = \frac{\text{std dev}}{\sqrt{n}} \tag{27}$$

The uncertainty of the standard deviation can be derived using the following equation [36]:

$$\sigma_{std\,dev} = \frac{\text{std dev}}{\sqrt{2 \cdot (n-1)}} \tag{28}$$

The one-pixel cluster makes up over 80 % and in some cases even over 90 % of the cluster size distribution both with and without reverse bias. The two-pixel clusters generally make up around 10 % of the distribution, while three- and four-pixel clusters barely reach 1 %. Cluster sizes above appear only occasionally. Consequently, the mean cluster size remains between 1 and 2 pixels. The error of the mean stays at 0.001 pixels without reverse bias and partly increases to 0.002 pixels with reverse bias. This elevation of the error stems from the reduced amount of data available for the case with applied reverse bias. Overall, the small relative error amounts to approximately 0.1 %.

The generally low cluster sizes detected for BabyMOSS can be attributed to the thin epitaxial layer and large depletion region in relatively small pixels. This results in a sensor, which is drift dominated and with short distances between the point of charge generation and charge collection, causing the charge to be collected mainly in one pixel.

When comparing the cluster size distributions with and without reverse bias, small differences are to be expected since the thresholds of the regions tend to be slightly higher with reverse bias applied using the provided standard setting for VCASB of 84 DAC units. A higher threshold reduces the probability to detect clusters with multiple pixels, due to the low amount of charge that is collected by each diode, when the charge is shared between multiple pixels. As a result, the mean cluster size decreases in the regions top 1 and 2, as well as in the regions bottom 0, 1 and 2, with reductions ranging from 0.008 to 0.046 pixels.

Additionally, when the depletion region is expanded, the diffusion process can be neglected as a transport process since it occurs on a much longer timescale compared to the drift process. For a fully depleted sensor, a decrease in the average cluster size would be expected, since it becomes more probable that the deposited charge is fully collected by the nearest diode through drift, resulting in one-pixel clusters. On the other hand, even without reverse bias there is a significant contribution from the drift process due to the small pixel size and thin epitaxial layer, which already results in low cluster sizes.

However, region top 3 and bottom 3 exhibit an increase of the mean cluster size of 0.023 and 0.111 pixels, respectively, when reverse bias is applied. This can be associated with a decreased fake-hit rate. Since an increased fake-hit rate leads to an increased

production of one-pixel clusters, a shift of the average cluster size towards lower values can be expected with no reverse bias applied. Both region top 3 and bottom 3 exhibit a tail in the distribution of pixel counts against hit count, corresponding to a large fraction of pixels with exceptionally high hit counts compared to the mode, when no reverse bias is applied (Fig. 32). No such tail in the distribution can be observed with reverse bias (Fig. 37). Consequently, both regions have a higher number of masked pixels without reverse bias and can be expected to exhibit a higher fake-hit rate even after the masking. This is more extreme for region bottom 3, which exhibits a left-to-right asymmetry in hit counts, as displayed in Fig. 36.

This effect can also be expected to cause the lower average cluster size for bottom region 3 compared to the other regions when no reverse bias is applied (Fig. 42). To further validate the decrease in average cluster size originating from an increased number of fake hits, particle track reconstruction using a beam telescope of multiple pixel sensors could be employed to distinguish clusters produced by impinging particles from those caused by fake hits.

7.3 Exploration of the Average Cluster Size over the VCASB Range

The VCASB DAC setting can be adjusted in order to modify the discrimination threshold of the pixels. For an increasing VCASB value, the threshold decreases and smaller signal voltages cause a hit to be detected. This, in turn, influences the cluster sizes detected with the pixel sensor. The globally set VCASB settings result in varying thresholds for each region due to differences in the in-pixel front-end electronics (Fig. 16). Therefore, exploring the average cluster sizes of the regions of BabyMOSS over the VCASB range determined in chapter 5 not only enables the analysis of the average cluster size for varying thresholds, but also a comparison between the regions of the BabyMOSS.

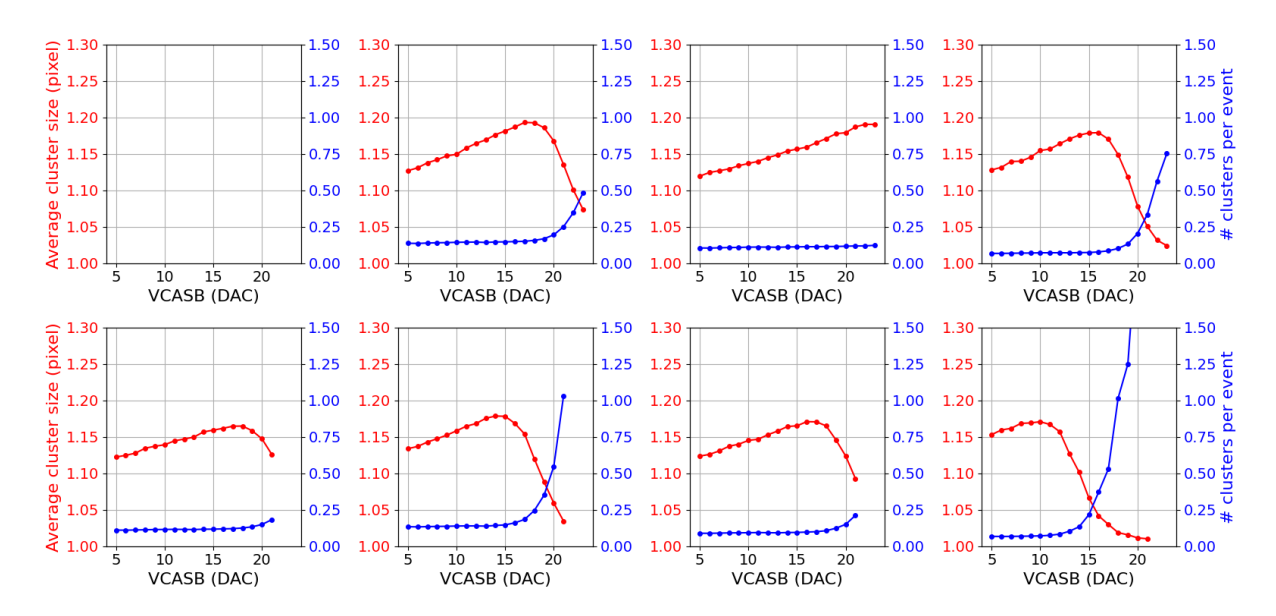


Figure 44: Average cluster size plotted against VCASB at VBB = $0\,\mathrm{V}$. The average cluster size is plotted against the VCASB value in red and the number of clusters per event is plotted against the VCASB value in blue. For each VCASB value, two million events were used in the data taking process and masking was applied using the method described in 7.1. The panels depict the eight regions of the BabyMOSS.

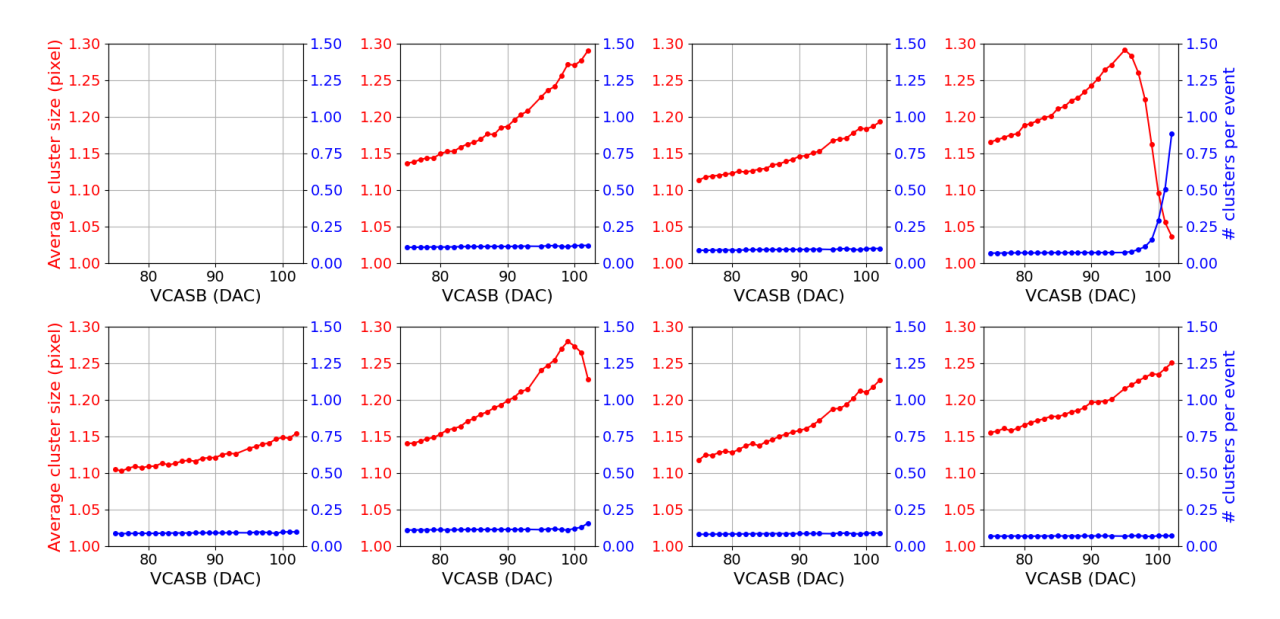


Figure 45: Average cluster size plotted against VCASB at VBB = $-1.2\,\mathrm{V}$. The average cluster size is plotted against the VCASB value in red and the number of clusters per event is plotted against the VCASB value in blue. For each VCASB value, one million events were used in the data taking process and masking was applied using the method described in 7.1. The panels depict the eight regions of the BabyMOSS.

In Fig. 44 and Fig. 45, the average cluster size and the number of clusters per event are plotted against the VCASB values. The number of clusters per event is used as an indirect measure for the amount of recorded fake hits, as fake hits produce one-pixel clusters and for an increasing number of detected fake hits more clusters are detected per event.

Fig. 44 depicts the average cluster size and the number of clusters per event without applied reverse bias. The measurement starts at VCASB = 5 DAC units, i.e. the highest threshold. As the VCASB value increases and the threshold decreases, the number of fake hits and consequently the amount of data taken per pixel per event at high VCASB values increases. Accordingly, a rising number of clusters per pixel per event can be observed in Fig. 44. This makes the data analysis increasingly more time inefficient and approaches the limits of possible data analysis, which is why the data taken at the test beam is analyzed up to VCASB = 21 DAC units.

In order to extend the lower threshold range for matching the different regions of the sensor to the same operating points in chapter 7.4, two additional VCASB settings are analyzed for the top half unit, that generally exhibits higher threshold values compared to the bottom unit as shown in Fig. 26.

At first, the average cluster size rises steadily for increasing VCASB values throughout all regions. Due to the decreasing threshold, less charge needs to be collected by each diode in order for the signal to exceed the threshold, which increases the probability of detecting clusters containing multiple pixels. As a result, the average cluster size rises until it approaches a maximum, where the lowest threshold is reached that does not yet result in a rise of the number of clusters per event due to an increased fake-hit rate. The maximum average cluster size is located between 1.15 and 1.20 pixels for all regions. After reaching this maximum, the mean cluster size starts declining steeply. At the same time, the number of detected clusters per event at each VCASB setting starts rising. This indicates, that fake hits start dominating compared to hits generated by impinging particles due to the decreasing threshold. At which VCASB setting the decline in mean cluster size begins is dependent on the corresponding effective threshold of the region. For example, region bottom 3 exhibits the lowest threshold for the same global VCASB settings compared to all other regions (Fig. 26) and the decline therefore starts at lower VCASB settings for this region.

In Fig. 45, the mean cluster size and the number of clusters per event are plotted against the VCASB values with reverse bias applied. The test beam data with reverse bias is analyzed from VCASB = $75\,\mathrm{DAC}$ units up to VCASB = $102\,\mathrm{DAC}$ units. As seen for the case without reverse bias, the average cluster size rises for increasing VCASB values due to the decreasing threshold and the therefore increasing probability of detecting clusters of multiple pixels.

The average cluster size climbs for some regions above the value of 1.2 pixels, which was the approximate maximum cluster size observed without reverse bias (Fig. 44). This can be attributed to the number of clusters per event only starting to rise, when the average cluster size approaches a value of 1.3 pixels, as seen for region top 3 and bottom 1 (Fig.

45). Region top 3 and bottom 1 both display a maximum of the average cluster size between 1.25 and 1.30 pixels, before the decline of the mean cluster size begins. Again, this decline is accompanied by a rise in the number of clusters per event, due to the increasing amount of fake hits. All other regions don't reach a decline in average cluster size and also don't show an incline in the number of clusters per event in the tested range. The overall higher maximum in average cluster size when reverse bias is applied can be attributed to the improved signal-to-noise ratio, which was discussed in chapter 7.1.2. The improved signal-to-noise ratio results in fake hits starting to dominate only when a threshold is reached, that allows for larger cluster sizes to be detected.

7.4 Average Cluster Sizes for Matched Thresholds

In order to be able to compare the average cluster sizes between the regions for the same thresholds, i.e. working points, the results of chapter 5.2 are used to select VCASB settings for each region, which correspond to the same or a similar operating point. For the available VCASB range, the lowest and highest possible threshold is determined, that can be reached with every region. These thresholds, along with one in the middle, serve as the working points to which the eight regions of the BabyMOSS are set to. Without reverse bias, this results in the thresholds of 28, 31 and 33 DAC units. With reverse bias applied, the thresholds of 24, 27 and 29 DAC units are used. One DAC unit corresponds to 7 ± 3.5 electrons (Eq. 19). The determined VCASB values of each region corresponding to these thresholds are used to select the required dataset for each region.

It is important to keep in mind, that the thresholds measured in the laboratory scans might differ from the thresholds the BabyMOSS exhibited during the test beam campaign due to the corresponding environmental conditions and possible differences in bandgap trimming, as discussed in chapter 7.1.1.

7.4.1 Analysis for Matched Thresholds without Reverse Bias

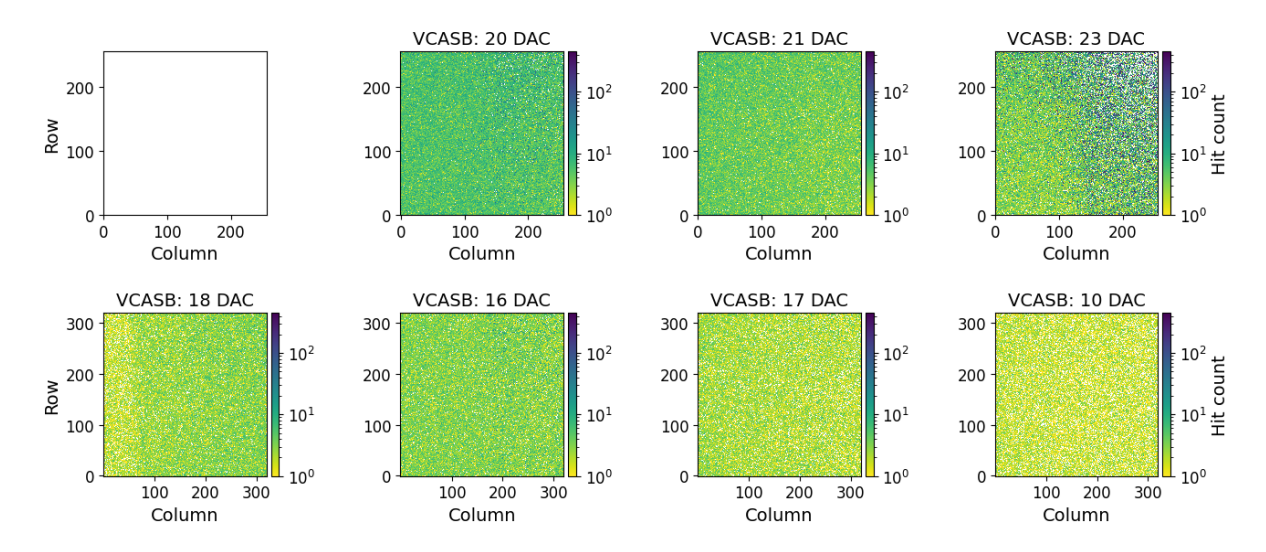


Figure 46: Hitmaps for a threshold of 28 DAC units at VBB = $0\,\mathrm{V}$. The data taken for two million events is analyzed and masking was applied using the method described in 7.1. The panels depict the eight regions of the BabyMOSS.

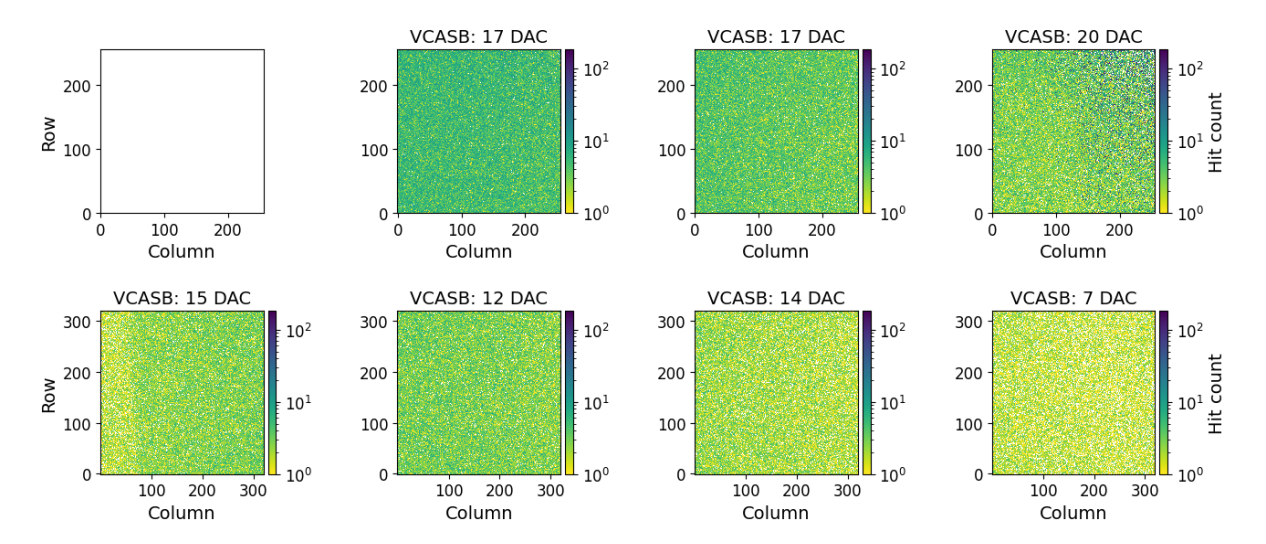


Figure 47: Hitmaps for a threshold of 31 DAC units at $VBB = 0 \, V$. The data taken for two million events is analyzed and masking was applied using the method described in 7.1. The panels depict the eight regions of the BabyMOSS.

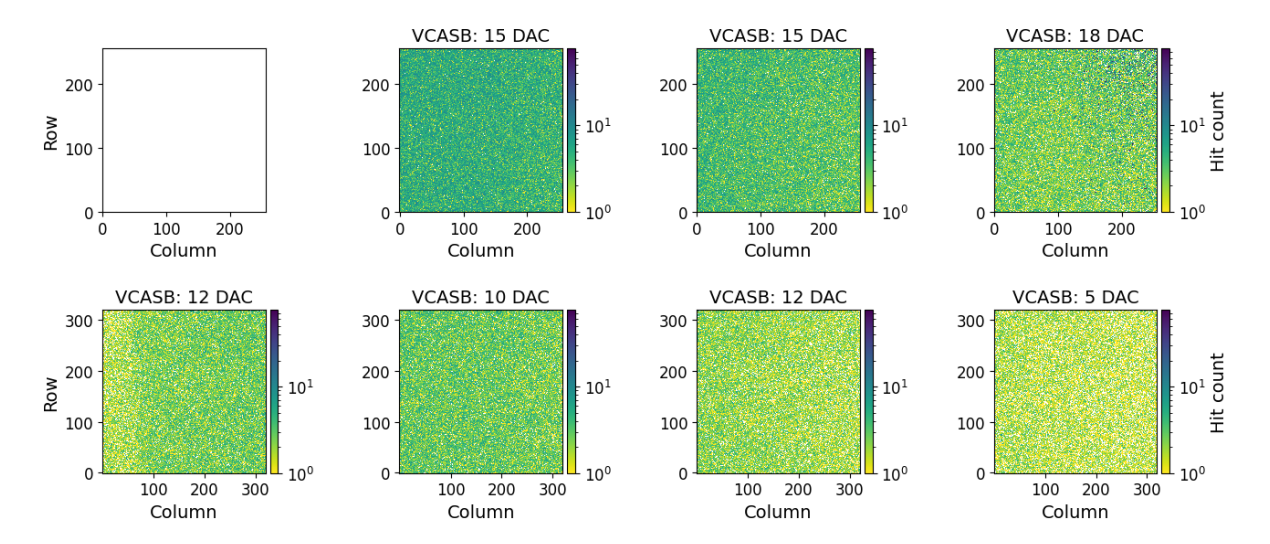


Figure 48: Hitmaps for a threshold of 33 DAC units at $VBB = 0 \, V$. The data taken for two million events is analyzed and masking was applied using the method described in 7.1. The panels depict the eight regions of the BabyMOSS.

Fig. 46 to 48 display hitmaps corresponding to increasing thresholds of 28 DAC units, 31 DAC units and 33 DAC units respectively. In order to enable better comparison between the hitmaps for matched thresholds, a logarithmic color scale of the same range was chosen to display the hit counts. Above each region, the selected VCASB value is displayed and the data taken with this VCASB setting is used for this specific region. For regions that have shown lower thresholds compared to the other regions for the same VCASB settings, the threshold needs to be elevated in comparison and therefore the VCASB setting is lowered. Since region bottom 3 has the lowest threshold in comparison to the other regions at the same VCASB setting (Fig. 26), it is now assigned the lowest VCASB value.

In turn, for regions that exhibit higher thresholds compared to the other regions for the same VCASB setting due to differences in the front-end circuitry, the threshold needs to be lowered and therefore the assigned VCASB setting is higher. As region top 3 has the highest threshold when comparing the regions at the same VCASB settings, as depicted e.g in Fig. 34, it is now assigned the highest VCASB value.

As region bottom 0 to 2 have the same front-end (Fig. 16), they are expected to have roughly the same response. Indeed, the VCASB settings for region bottom 0, 1 and 2 are around the same value for a specific threshold with deviations of about ± 1 DAC unit that can be attributed to the uncertainty of the measured threshold of 1 DAC unit, which originates from performing the threshold scan using only five rows of the pixel matrix, as discussed in chapter 5.2.

The regions display differing behavior in hit counts, even for approximately the same threshold. Region top 3 exhibits a left-to-right asymmetry in hit counts, as well as an increasing hit count for higher rows, especially for the threshold of 28 DAC units. This

region already exhibited a relatively high number of noisy pixels in relation to its threshold, as discussed in chapter 7.1.1. For region top 1, a left-to-right asymmetry can also be observed for a threshold of 28 DAC units. This behavior can be associated with differences in the front-end electronics, as well as possible deviations of the measured thresholds of the regions from the actual thresholds at the test beam due to environmental differences or deviations in the bandgap trimming.

Besides, region top 1 displays a higher average hit count over the whole matrix compared to other regions and especially region bottom 3, which displays a lower hit count compared to other regions for each threshold setting. For one, this can be attributed to the lower number of pixels in the pixel matrices of the top unit. Due to the larger pixel pitch, a region in the top unit has 256 x 256 pixels compared to 320 x 320 pixels a region of the bottom unit possesses. Consequently, a pixel of the top unit is expected to show a higher hit rate than a pixel of the bottom unit for the same number of hits detected over the whole region. Additionally, the beam profile is expected to not be uniform over the whole BabyMOSS. When analyzing both units separately, the highest hit count over the whole matrix is visible for region top 1 and bottom 1 respectively, with a decreasing hit count for increasing region numbers. For the bottom unit, region bottom 0 also seems to display a decreasing number of hit counts, without taking the stripe of lower hit counts to the far left into account. This can be attributed to the beam being centered on the location of the regions top and bottom 1 and when moving away from the beam center, fewer hits induced by particles are detected.

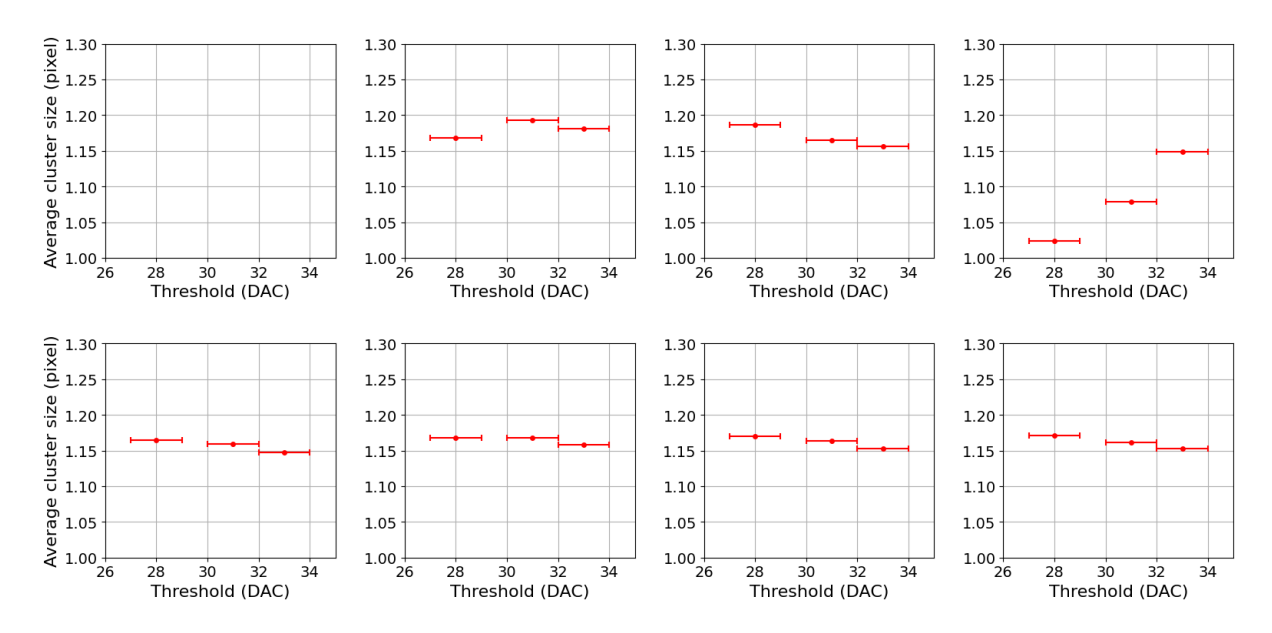


Figure 49: Average cluster size plotted against the threshold in DAC units at VBB = 0 V with 1 DAC unit as the threshold error. The panels depict the eight regions of the BabyMOSS.

In Fig. 49, the average cluster sizes are plotted against the threshold using the data

displayed in the previous hitmaps. The error on the threshold of 1 DAC unit originates from the dominating threshold uncertainty introduced by scanning only five rows of the whole pixel matrix, as discussed in chapter 5.2. The error on the average cluster size is in the vicinity of 0.001, as discussed in chapter 7.2, which is significantly smaller than the displayed scale increments of 0.05 and therefore not visually represented. The bottom unit displays a similar behavior for all regions with slightly decreasing average cluster size for higher thresholds, starting below 1.20 pixels and ending near 1.15 pixels. This is consistent with the expectation, that region bottom 0 to 2 show similar responses for the same thresholds due to having the same in-pixel front-end design. The decrease appears because a larger signal is needed to exceed the threshold and therefore the probability to detect clusters containing multiple pixels decreases. The top unit displays this behavior only for region top 2. Region top 1 shows first an increased average cluster size for the threshold of 31 DAC units and then a decreased average cluster size for a threshold of 33 DAC units. The slightly lower mean cluster size at a threshold of 28 DAC units can be attributed to the increased fake-hit count this region shows with a left-to-right asymmetry for this threshold setting (Fig. 46). The pixels with exceptionally high hit counts compared to the most probable hit count can be associated with fake hits, as discussed in chapter 7.1, which produce one-pixel clusters and therefore result in a decrease of the mean cluster size. However, the values for average cluster size stay in the region between 1.15 and 1.20 pixels for region top 1. The largest discrepancy from the behavior of the other regions can be found for region top 3, exhibiting an increase in average cluster size due to the decreasing contribution of fake hits that can be observed for the corresponding hitmaps. The lowest threshold of 28 DAC units results in a visible left-to-right asymmetry in hit counts for region top 3 (Fig. 46) corresponding to an increased amount of recorded fake hits. For a threshold of 31 DAC units, this left-to-right asymmetry decreases (Fig. 47). For the highest threshold of 33 DAC units, no left-to-right asymmetry can be observed (Fig. 48) and the reduced amount of recorded fake hits, which produce one-pixel clusters, results in a higher average cluster size.

7.4.2 Analysis for Matched Thresholds with Reverse Bias

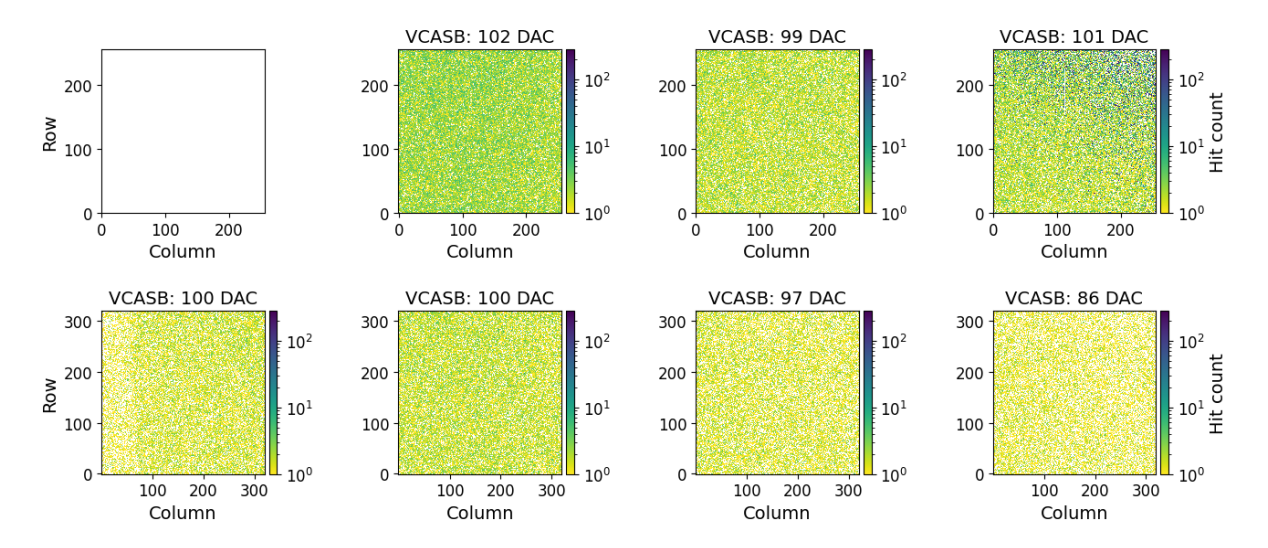


Figure 50: Hitmaps for a threshold of 24 DAC units at VBB = -1.2 V. The data taken for one million events is analyzed and masking was applied using the method described in 7.1. The panels depict the eight regions of the BabyMOSS.

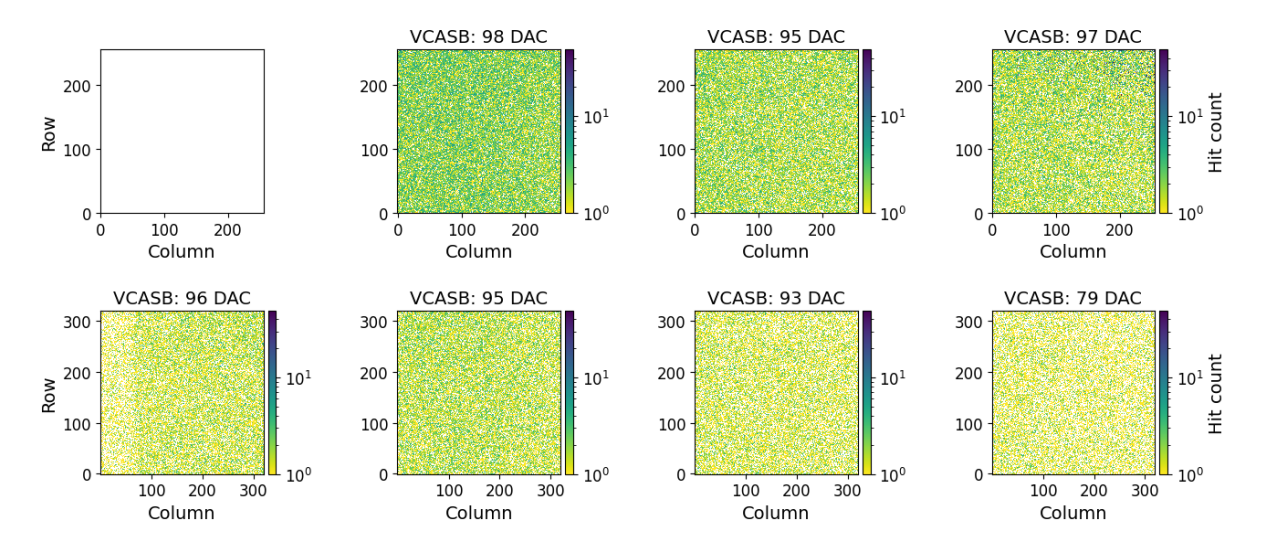


Figure 51: Hitmaps for a threshold of 27 DAC units at VBB = -1.2 V. The data taken for one million events is analyzed and masking was applied using the method described in 7.1. The panels depict the eight regions of the BabyMOSS.

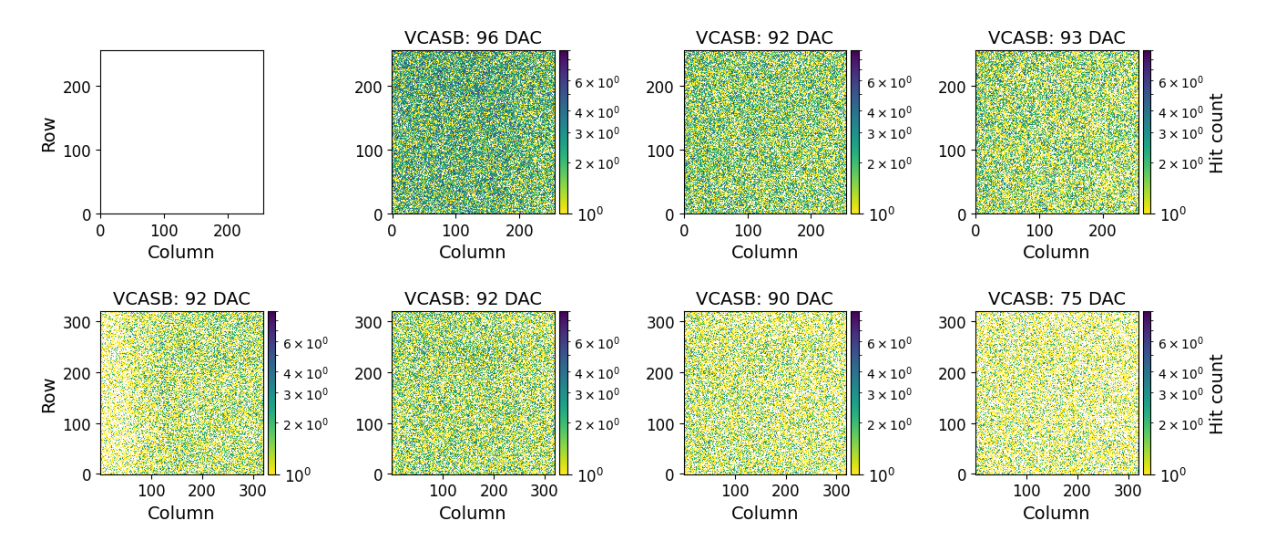


Figure 52: Hitmaps for a threshold of 29 DAC units at VBB = $-1.2\,\mathrm{V}$. The data taken for one million events is analyzed and masking was applied using the method described in 7.1. The panels depict the eight regions of the BabyMOSS.

For applied reverse bias, Fig. 50 to and 52 display the hitmaps corresponding to an increasing threshold of 24 DAC units, 27 DAC units and 29 DAC units respectively. Again, a logarithmic color scale of the same range was chosen and the selected VCASB value is displayed above each region.

Region bottom 0, 1 and 2, which have the same front-end design, show deviations in VCASB settings of ± 1 or 2 DAC units for the same selected threshold, which can be associated with the uncertainty of the measured threshold.

No left-to-right asymmetry in hit counts can be observed for applied reverse bias due to the improved signal-to-noise ratio, which was discussed in chapter 7.1.2. Region top 3 displays pixels of the highest hit count, which are distributed increasingly toward the top right edge. This is mainly prominent at a threshold of 24 DAC units and decreases for higher thresholds as the fake-hit rate decreases. Again, regions of the top unit generally display higher hit counts than regions of the bottom unit due to the lower number of pixels, which are of a larger pixel pitch. As expected, the beam is again centered toward region 1 for both units and fewer particle hits are detected when moving further away from this region.

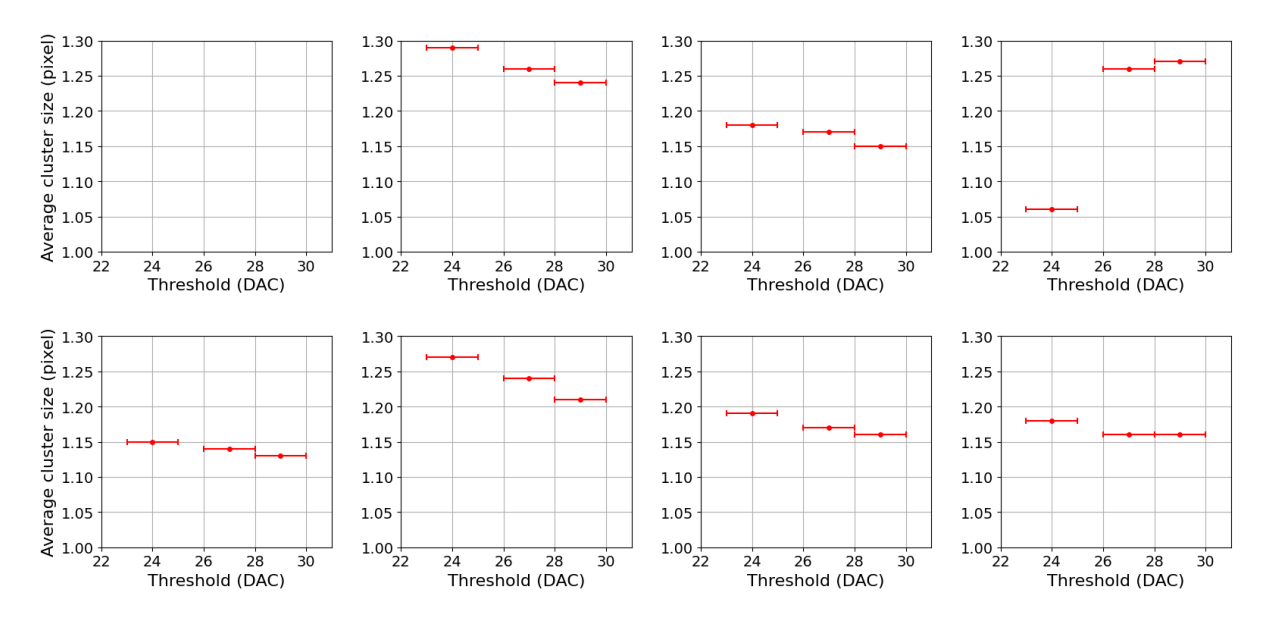


Figure 53: Average cluster size plotted against the threshold in DAC units at VBB = -1.2 V with 1 DAC unit as the threshold error. The panels depict the eight regions of the BabyMOSS.

In Fig. 53, the mean cluster size is plotted against the threshold using the selected data shown in the previous hitmaps. Consistent with the observed variations in behavior displayed in Fig. 45, the average cluster sizes of the regions display differences up to about 0.25 pixels for a specific threshold. The highest average cluster size displayed for each region varies between 1.15 and almost 1.30 pixels. Most regions show a slight decrease in average cluster size for higher thresholds, since more collected charge is needed for a hit to be detected, which reduces the probability of detecting clusters of a size above one pixel. In contrast to the case without reverse bias, region top 1 exhibits now also a decreasing cluster size for increasing thresholds. However, region top 3 again shows a steep increase in average cluster size associated with the reduction of fake hits for increasing thresholds. While the differences in average cluster size between the regions can mostly be associated with differences in the front-end, region bottom 0, 1 and 2 are expected to show similar behavior for the same applied threshold, as they have the same in-pixel front-end electronics. However, these regions exhibit varying average cluster sizes for the selected thresholds with deviations ranging from 0.03 to 0.12 pixels. Variations in behavior for these regions can also be observed for the average cluster size plotted against the measured VCASB range (Fig. 45). Repeated measurements with calibrated thresholds should be performed to enable a direct comparison between the regions and to assess whether this behavior persists.

8 Conclusion and Outlook

During the Long Shutdown 3 (2026-2029) of the LHC at CERN, the ALICE experiment will upgrade the Inner Tracking System (ITS2) to the next-generation ITS3. In this upgrade, the three innermost vertexing layers of the ITS2 Inner Barrel will be replaced with truly cylindrical layers made of bendable wafer-scale silicon sensors. This upgrade reduces the material budget per each layer, as well as allowing the layers to be placed closer to the interaction point, therefore improving the spatial resolution and the track reconstruction efficiency of low-momentum particles.

The large curved sensors for the ITS3 will be produced using the TPSCo 65 nm CMOS technology, which allows for denser circuitry and larger wafers compared to the predecessor sensors ALPIDE, which are produced by the same company with 180 nm CMOS technology. Since wafer-scale sensors cannot be created directly due to photolithography constraints, a new procedure called stitching is used, where the mask is periodically exposed and aligned creating seamless transitions between regions. A first large stitched sensor prototype called MOSS (Monolithic Stitched Sensor) was produced in a first engineering run. It has a design featuring ten pixel sub-matrices, called Repeated Sensor Units (RSUs), with data and power lines that are stitched across the larger sensor. Each RSU is divided in two standalone half-units (top and bottom), each in turn containing four sub-matrices, also referred to as regions. The top and bottom regions have different pixel pitches and therefore a different number of pixels for the same area. For the top unit, each region consists of 256×256 square pixels, each having a pitch of $22.5 \,\mu\text{m}$, while regions of the bottom unit have 320×320 , each with a pitch of 18 µm. Each sub-matrix is characterized by different circuit densities and front-end designs. This combination of different pixel pitches and design optimizations was selected to study the impact of various front-end architectures on charge collection efficiency and to identify the optimal balance between circuit density and performance. Each wafer contains six MOSS sensors, as well as smaller test chips. One such test chip, known as BabyMOSS, consists of an individual RSU. The performance characterization of one such sensor is the aim of this study.

Threshold scans

The specific BabyMOSS sensor studied in this thesis is the babyMOSS-1_2_W22C7, which is hosted by a carrier card, connected to a raiser board that serves as an adapter board, which is then connected to a DAQ board. The region top 0 of the studied BabyMOSS is non-functional. A series of threshold scans were performed on the BabyMOSS sensor, confirming its electrical functionality of the remaining regions. For the default DAC settings in the case of no reverse bias applied (Tab. 1), both the threshold and temporal noise distribution of each region were analyzed. Due to production-related variations in the transistors of the in-pixel electronics, which is referred to as fixed-pattern noise, the

threshold distributions should resemble a Gaussian distribution. However, the resulting $\chi^2_{\rm red}$ from fitting the data to a Gaussian function indicate a poor fit, which is primarily attributed to manufacturing variations. Additionally, stripes of pixels exhibiting lower thresholds were observed in 2D distributions of the average thresholds (Fig. 22). These stripes, which are known to be visible for BabyMOSS but not MOSS with pixels of a lower threshold by approximately 2 to 3 DAC units, have been observed to correlate with floating power-hopping lines and are still under investigation. By comparing Gaussian fits of threshold distributions from BabyMOSS to ones conducted for MOSS, the influence of these stripes on the distributions could be further examined.

Due to the differences in the front-end, each region of the sensor displays varying behavior when global DAC settings are applied with individual thresholds that span over a range of 12 DAC units, which converts to a charge of 84 ± 42 electrons. The uncertainty of the charge stems from the uncertainty of the design value of the capacitance of the capacitor used to inject the charge. The exact value of the capacitance is still under investigation. Regions that exhibit lower thresholds than others for the same applied settings can be associated with an increase in the number of noisy pixels. This is distinctly visible for region bottom 3 of the BabyMOSS for the applied default DACs (Fig. 23).

Recently, applying specific DAC settings for each region has become possible. This enables the calibration of the BabyMOSS to one desired global threshold, which is of great advantage for the comparison of the behavior of the eight regions in terms of particle detection.

The thresholds of the BabyMOSS were explored for the case when no reverse bias is applied, as well as for a reverse bias of $-1.2\,\mathrm{V}$ applied between the collection diode and the substrate. This was done over a range of globally set VCASB values, which is the primary DAC used for controlling the discrimination threshold. In order to improve the time efficiency of the threshold scans, five rows of each pixel matrix were used to perform one threshold scan for each setting, instead of the full matrix scan. This was shown to be enough to reproduce the representative value that the full matrix scan gives. The average threshold was plotted against VCASB for both cases with and without applied reverse bias and the overall antiproportional behavior allows to steer the threshold via the VCASB value. (Figs. 26 and 27). Overall, the BabyMOSS sensor exhibited consistent behavior with previous BabyMOSS studies, apart from the malfunctioning region, confirming its functionality and suitability for further development.

Test beam campaign at the DESY II test beam facility

In order to further examine the behavior of the BabyMOSS in response to varying operating points, the sensor was included in a test beam campaign at the DESY II test beam facility in April 2024. Due to multiple research projects being targeted with this test beam campaign, the BabyMOSS did not represent the primary DUT and was not

placed inside a beam telescope, which would have enabled track-based analysis using other reference sensors. The BabyMOSS was placed behind a scintillator, which provided trigger signals. Due to the sensor not being the primary focus of the test beam, a total of two million events were recorded with a beam of $2.4 \, \text{GeV/c}$ electrons with no reverse bias applied, and one million events were recorded with a beam of $4.8 \, \text{GeV/c}$ electrons while this time the sensor was reverse biased at $-1.2 \, \text{V}$. This allows the study of the cluster size and noise behavior during in-beam conditions.

Investigation of hit count distributions and pixel masking

When analyzing the test beam data taken with no reverse bias applied, a left-to-right asymmetry in hit counts can be observed, which appears in regions especially for high VCASB values, which result in low thresholds (Fig. 54). This can be attributed to an increased fake-hit rate for the right half of the pixel matrix due to a lower effective threshold. This left-to-right asymmetry in the fake-hit rate was already observed for MOSS and BabyMOSS and correlates with the value and the distribution of the strobe signal over the matrix. This effect is currently under investigation. No left-to-right asymmetry is visible when reverse bias is applied and the sensor is fully depleted, which can be associated with the improved signal-to-noise ratio (Fig. 41).

A first step in the analysis of the test beam data is noisy pixel masking. Pixels that have exceptionally high count compared to the average pixels in the matrix are identified and masked, in order not to bias the analysis. A customized masking method was applied to the recorded data in order to use the entire dataset of each setting for the masking and to get a better understanding of the individual behavior of the regions of the BabyMOSS, which allows for a more educated masking process. The total number of pixels corresponding to a specific hit count was plotted. For the exemplary setting without reverse bias, regions which exhibit a left-to-right asymmetry in hit counts resulted in an increasing amount of pixels that are assigned to high hit counts in relation to the most probable hit count for the region (Fig. 32). Pixels were classified as noisy and masked, when their hit count exceeded a cutoff point, which was set to be at the highest hit count exhibited by ten pixels. As a result, a large fraction of the pixels with high hit counts are masked for regions that show a tail in the distribution towards higher hit counts, caused by an increasing number of recorded fake hits. For regions without this tail, only the sporadic outlier pixels are masked. The amount of noisy pixels has been observed to not only depend on the presence of a left-to-right asymmetry caused by the low threshold of the region, but also on the individual behavior of the regions due to the variations of the front-end electronics. However, this observation might be biased by differences between the actual thresholds of the regions during the data taking and the measured thresholds conducted by performing laboratory scans for globally set VCASB values. These differences may be caused by environmental changes, particularly temperature variations, to which both the MOSS

and BabyMOSS have been shown to be sensitive. The dependency between threshold and temperature can be estimated to about 0.3 DAC per 1 °C. The temperature was not controlled or measured at the test beam, where data was taken over long periods of time with possible influences of the day-night cycle. For the laboratory scans, the temperature was also not controlled or measured, leading to possible differences to the test beam conditions. In order to account for changes in temperature, more recent versions of the raiser board provide the possibility to measure the room temperature during the operation of the chip. Additionally, differences in bandgap trimming at the test beam and the laboratory scans cannot be ruled out. The bandgap trimming influences the reference voltage and current used by the DACs to convert digital signals to analog ones. This, in turn, influences the set discrimination threshold, which can therefore possibly exhibit differences.

Cluster size analysis

The data with noisy pixels masked was used to analyze the cluster sizes. The total number of the pixels detecting a hit associated to the same particle define the cluster size and the position of a cluster is calculated using the center of gravity method. When analyzing the cluster size distributions for given standard VCASB settings, both in the case where no reverse bias voltage is applied and when it is, the predominant cluster is the one-pixel cluster due to the drift dominated collection mechanism. They account for about 80-90% of the total clusters. The rest is made by two-pixel clusters (about 10%) and less than 1% by larger clusters. Consequently, the mean cluster size stays between one and two pixels. The generally low cluster sizes detected for BabyMOSS can be attributed to the thin epitaxial layer and large depletion region of the relatively small pixels, which result in a drift dominated sensor, with strong electric fields and short distances between the point of charge generation and charge collection. In comparison, pixel sensors such as ALPIDE produced with a standard process and thicker epitaxial layer, which are dominated by diffusion, exhibit average cluster sizes between two and three pixels, which allows for an improvement of the binary resolution (approximately 8 µm in the case of the ALPIDE sensor with a pixel pitch of $\sim 30 \, \mu \text{m}$) to a spatial resolution below $5 \, \mu \text{m}$ [12]. In the case of the BabyMOSS, clustering can be expected to have a smaller impact on the intrinsic spatial resolution. For the BabyMOSS, the binary resolution amounts to 6.5 µm for the top unit and 5.2 µm for the bottom unit. Due to the predominant cluster size of one, the spatial resolution can be expected to be close to the binary resolution, as there is little to no charge sharing. To achieve a intrinsic spatial resolution comparable to the ALPIDE sensors (5 µm), the smaller pixel pitch is required, made possible by the smaller feature size of the transistors in 65 nm CMOS technology. Due to the reduced material budget and the closer proximity of the sensors to the interaction point, the overall spatial resolution is still improved for the ITS3.

In order to analyze the behavior of the average cluster sizes for varying thresholds, the

average cluster sizes were plotted against the VCASB DAC settings (Figs. 44 and 45). In the case where no reverse bias is applied, the maximum mean cluster size is located between 1.15 and 1.20 pixels for all regions and limited by the increasing fake-hit rate for decreasing thresholds, which results in the increased production of one-pixel clusters. With reverse bias applied, the signal-to-noise ratio is improved and the number of recorded fake hits begins to dominate only at lower thresholds, which is why a maximum average cluster size in the vicinity of 1.30 pixels can be observed. By implementing the BabyMOSS as a device under test (DUT) in a beam telescope, which enables tracking particle trajectories, clusters could be assigned to specific traversing particles and the associated cluster sizes could be better determined by excluding clusters produced by fake hits over the matrix. Laboratory threshold scans were used to match the thresholds of each region for better comparison by selecting the corresponding VCASB settings. Without reverse bias applied, the average cluster sizes matched to the thresholds show similar behavior with values between approximately 1.15 and 1.20 pixels for most regions. However, region top 3 exhibits lower average cluster sizes associated with an increased fake-hit rate compared to the other regions (Fig. 49), indicating that a higher threshold for this region would reduce the bias introduced by fake hits. With reverse bias applied to achieve full depletion of the sensor, more variations of the cluster sizes between the regions can be observed due to differences of the in-pixel front-end design of the regions. However, region bottom 0, 1 and 2 are expected to behave similarly, as they have the same front-end. Yet, they show deviations in the average cluster size for specific thresholds ranging from 0.03 to 0.12 pixels (Fig. 53). Repeated measurements with calibrated thresholds would allow for a direct comparison of the cluster size trends between the regions and could help assess whether this behavior persists.

Outlook

The characterization of the BabyMOSS has provided valuable insights into the behavior of threshold and noise, as well as cluster size distributions. Additional studies of the BabyMOSS and MOSS as the DUT in test beams with controlled environmental conditions and directly calibrated thresholds would enable precise particle tracking beneficial for the cluster size analysis. Moreover, ongoing studies examine the correlation between the choice of strobe length and fake-hit rate, aiming to optimize the operating regime of the sensor in order to reduce the impact of noise on the data. Further investigations of MOSS and BabyMOSS enable the optimization of the detector design, which is crucial for the performance of the ALICE ITS3.

Appendix

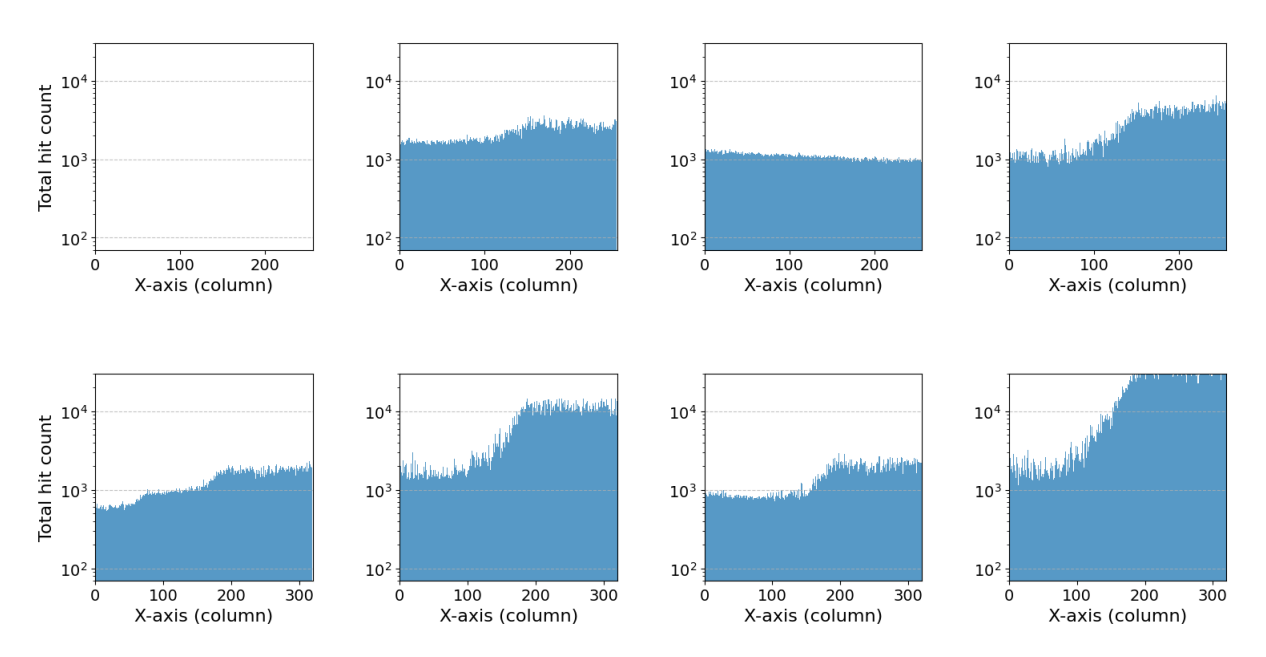


Figure 54: Hit count projected onto the x-axis for VCASB = 21 DAC units at VBB = 0 V after masking. The hit count projections show a left-to-right asymmetry for multiple regions due to the low thresholds.

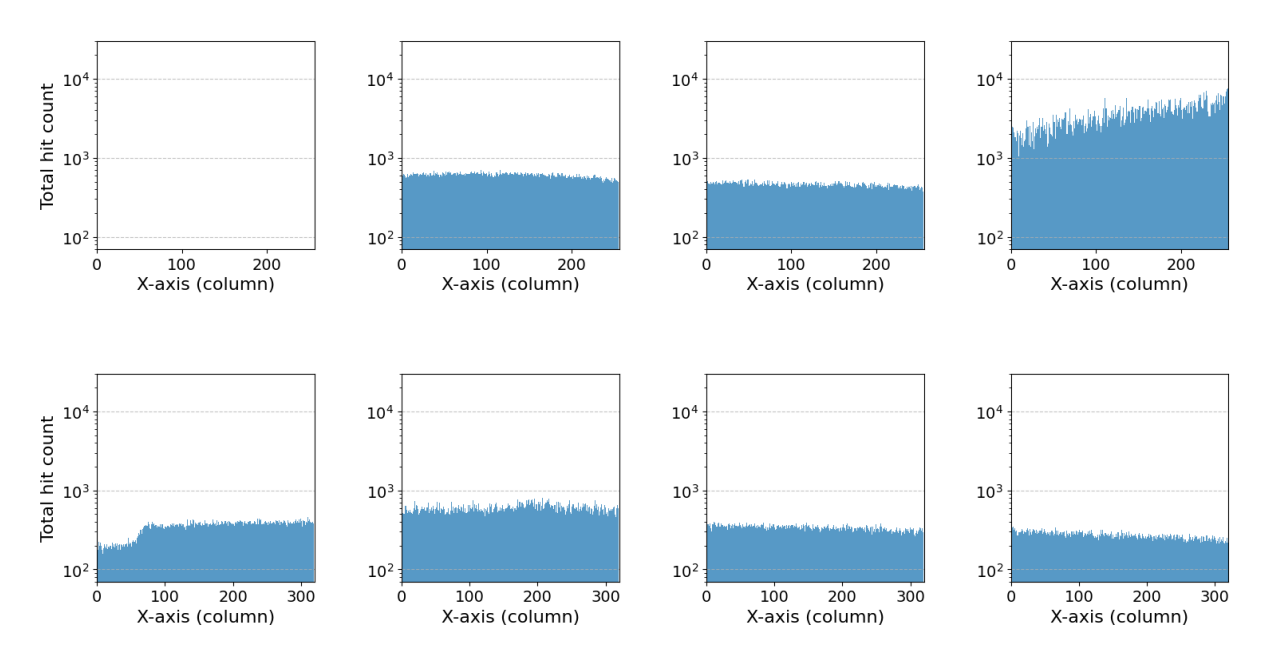


Figure 55: Hit count projected onto the x-axis for VCASB = $102\,\mathrm{DAC}$ units at VBB = $-1.2\,\mathrm{V}$ after masking. No left-to-right asymmetry as seen without reverse bias can be observed. Only region top 3 exhibits a steady increase in hit counts to the right side, but without a division into two distinct sides with different behavior.

References

- [1] Hermann Kolanoski and Norbert Wermes. *Particle detectors: Fundamentals and applications*. Reprinted with corrections in 2022, Impression: 2. Oxford and New York, NY: Oxford University Press, 2022. ISBN: 978-0-19-885836-2.
- [2] Silvia Masciocchi. "The Physics of Particle Detectors: Heidelberg University lecture script, summer term 2022".
- [3] R. L. Workman et al. "Review of Particle Physics". In: *Progress of Theoretical and Experimental Physics* 2022.8 (2022). DOI: 10.1093/ptep/ptac097.
- [4] ALICE Collaboration. ALICE (A Large Ion Collider Experiment). URL: https://alice.cern/ (visited on 06/17/2024).
- [5] CERN. The Large Hadron Collider. URL: https://home.cern/science/accelerators/large-hadron-collider (visited on 06/25/2024).
- [6] ALICE Collaboration. "ALICE upgrades during the LHC Long Shutdown 2". In: Journal of Instrumentation 19.05 (2024), P05062. DOI: 10.1088/1748-0221/19/05/P05062. URL: http://arxiv.org/pdf/2302.01238v2.
- [7] Luciano Musa. Letter of Intent for an ALICE ITS Upgrade in LS3. 2019. DOI: 10.17181/CERN-LHCC-2019-018.
- [8] ALICE Collaboration. "Technical Design report for the ALICE Inner Tracking System 3 ITS3; A bent wafer-scale monolithic pixel detector". In: CERN-LHCC-2024-003, ALICE-TDR-021 (2024). URL: https://cds.cern.ch/record/2890181.
- [9] CERN. Longer term LHC schedule. URL: https://lhc-commissioning.web.cern.ch/schedule/LHC-long-term.htm (visited on 02/12/2025).
- [10] Frank Mattias Hartmann. Evolution of silicon sensor technology in particle physics. Second edition. Vol. Volume 275. Physics. Cham: Springer, 2017. ISBN: 978-3-319-64434-9. DOI: 10.1007/978-3-319-64436-3.
- [11] Wolfgang Demtröder. *Atome, Moleküle und Festkörper*. 5., neu bearbeitete und aktualisierte Auflage. Vol. 3. Springer-Lehrbuch. Berlin and Heidelberg: Springer Spektrum, 2016. ISBN: 978-3-662-49093-8.
- [12] Miljenko Suljic. "Study of Monolithic Active Pixel Sensors for the Upgrade of the ALICE Inner Tracking System". PhD thesis. Trieste U., 2017. URL: https://cds.cern.ch/record/2303618.
- [13] S. M. Sze and Kwok Kwok Ng. *Physics of semiconductor devices*. 3. ed. Hoboken, NJ: Wiley-Interscience, 2007. ISBN: 0-471-14323-5. DOI: 10.1002/0470068329. URL: https://search.ebscohost.com/login.aspx?direct=true&scope=site&db=nlebk&db=nlabk&AN=172575.

- [14] Behzad Razavi. Design of analog CMOS integrated circuits. Second editon. New York: McGraw Hill Education, 2016. ISBN: 978-0-07-252493-2. URL: https://ebookcentral.proquest.com/lib/kxp/detail.action?docID=6327694.
- [15] B. Abelev et al. "Technical Design Report for the Upgrade of the ALICE Inner Tracking System". In: *Journal of Physics G: Nuclear and Particle Physics* 41.8 (2014), p. 087002. ISSN: 0954-3899. DOI: 10.1088/0954-3899/41/8/087002.
- [16] Felix Reidt. "Studies for the ALICE Inner Tracking System Upgrade". PhD thesis. Heidelberg University Library, 2016. DOI: 10.11588/heidok.00020648.
- [17] Geun Hee Hong. "Monolithic Stitched Sensor (MOSS) Development for the ALICE ITS3 Upgrade". In: Proceedings of 10th International Workshop on Semiconductor Pixel Detectors for Particles and Imaging PoS(Pixel2022). Ed. by Hans-Günther Moser et al. Trieste, Italy: Sissa Medialab, 2023, p. 028. DOI: 10.22323/1.420.0028.
- [18] Tower Partners Semiconductor Co., Ltd. Official website of Tower semiconductor. URL: https://towersemi.com (visited on 02/16/2025).
- [19] P. Rai-Choudhury. Handbook of Microlithography, Micromachining, and Microfabrication. Vol. 39. SPIE Press monograph. Bellingham, Wash.: SPIE Optical Engineering Press, 1997. ISBN: 0-8194-2378-5.
- [20] ALICE Collaboration. "MOSS User Manual". URL: https://gitlab.cern.ch/groups/alice-its3-wp3/moss-testing/-/wikis/Moss%20user%20manual.
- [21] Styliani Paniskaki. "Characterisation of the first large-scale prototypes for the ALICE ITS3 Upgrade". PhD thesis. 2024.
- [22] M. Mager. "ALPIDE, the Monolithic Active Pixel Sensor for the ALICE ITS upgrade". In: Nuclear Instruments and Methods in Physics Research Section A: Accelerators, Spectrometers, Detectors and Associated Equipment 824 (2016), pp. 434–438. ISSN: 01689002. DOI: 10.1016/j.nima.2015.09.057.
- [23] ALICE Collaboration. Repository of software and firmware used within ITS3 WP3. URL: https://gitlab.cern.ch/alice-its3-wp3/moss-testing/sw/-/blob/master/moss_scans/dac_scan.py#L137 (visited on 01/27/2025).
- [24] Simone Emiliani. ITS3 TWEPP rehearsals: Investigation of non-idealities of pulsing circuitry in the ALICE ITS3 MOSS monolithic sensor. 2024-10-02. URL: https://indico.cern.ch/event/1456972/contributions/6133270/attachments/2930377/5150004/MOSS_pulsing_TWEPP24_Emiliani.pdf.
- [25] Zhenyu Ye and Iaroslav Panasenko. ITS3 WP3 Weekly Meeting: BabyMOSS test system development. 2024-03-05. URL: https://indico.cern.ch/event/1390271/contributions/5845102/attachments/2812789/4910009/yezhenyu_babyMOSS_20240305.pdf.

- [26] R. Diener et al. "The DESY II test beam facility". In: Nuclear Instruments and Methods in Physics Research Section A: Accelerators, Spectrometers, Detectors and Associated Equipment 922 (2019), pp. 265–286. ISSN: 01689002. DOI: 10.1016/j.nima.2018.11.133.
- [27] Pascal Becht. "Performance and characterisation of bent monolithic active pixel sensors (MAPS) for the application in future tracking detectors using the example of the ALPIDE chip". Master thesis. Heidelberg, 2021. URL: https://www.physi.uni-heidelberg.de/Publications/Pascal_Becht_master_thesis.pdf.
- [28] Y. Liu et al. "EUDAQ2 A Flexible Data Acquisition Software Framework for Common Test Beams". In: Journal of Instrumentation 14.10 (2019), P10033–P10033. DOI: 10.1088/1748-0221/14/10/P10033. URL: http://arxiv.org/pdf/1907. 10600v3.
- [29] Jens Kröger, Simon Spannagel, and Morag Williams. *User Manual for the Corryvreckan Test Beam Data Reconstruction Framework, Version 1.0.* URL: http://arxiv.org/pdf/1912.00856v1.
- [30] Dominik Dannheim et al. "Corryvreckan: A Modular 4D Track Reconstruction and Analysis Software for Test Beam Data". In: *Journal of Instrumentation* 16.03 (2021), P03008. DOI: 10.1088/1748-0221/16/03/P03008. URL: http://arxiv.org/pdf/2011.12730v2.
- [31] Karl Gran Grodas. ITS3 WP3 Weekly Meeting: MOSS Temperature Measurements. 2024-04-30. URL: https://indico.cern.ch/event/1411658/contributions/5933564/attachments/2847070/5006641/MOSS%20Temperature%20Measurement. pdf.
- [32] Vinayak Hande and Maryam Shojaei Baghini. "Survey of Bandgap and Non-bandgap based Voltage Reference Techniques". In: *Scientia Iranica* 23.6 (2016), pp. 2845–2861. DOI: 10.24200/sci.2016.3994.
- [33] Styliani Paniskaki. ITS3 WP3 Weekly Meeting: Summary results of March PS testbeam and fake-hit rate analysis. 2024-07-09. URL: https://indico.cern.ch/event/1435685/contributions/6041257/attachments/2892821/5071370/summaryMarchTestbeam_FHR.pptx.
- [34] Styliani Paniskaki. ITS3 WP3 Weekly Meeting: Fake-hit rate studies on NIEL irradiated babyMOSS and non-irradiated MOSS. URL: https://indico.cern.ch/event/1437774/contributions/6050211/attachments/2896861/5079854/Fake-hit_rate_studies.pptx.

- [35] Miljenko Suljic. ITS3 Plenary: ER1 testing summary and planned measurements. 2025-01-21. URL: https://indico.cern.ch/event/1496205/contributions/6305619/attachments/2999532/5285421/2025-01-21_its3_plenary_moss.pdf.
- [36] Sangtae Ahn and Jeffrey A. Fessler. Standard Errors of Mean, Variance, and Standard Deviation Estimators. URL: https://www.eecs.umich.edu/techreports/systems/cspl/cspl-413.pdf.

Acknowledgements

I would like to express my sincere gratitude to Silvia Masciocchi for giving me the opportunity to be part of the ALICE group and for the invaluable support I received during my work with the BabyMOSS. I would also like to thank Dr. Klaus Reygers, the second examiner of this work. Moreover, I would like to extend my appreciation to Bogdan Blidaru, Pascal Becht, and Maurice Donner for their help and mentorship throughout this project.

A special thanks goes to everybody who supported me emotionally. I am truly grateful to have so many wonderful people in my life whom I can call at any given time.

Declaration

I confirm that I have written this thesis independently and have not used any sources or aids other than those stated.

Heidelberg, 23.02.2025